

**PONTIFICIA UNIVERSIDAD  
CATÓLICA DEL PERÚ**

**Escuela de Posgrado**



**Characterization of luminescent ITO:Tb  
and AZO:Tb thin films prepared by  
radio frequency magnetron sputtering**

Tesis para obtener el grado académico de Doctor en Física  
que presenta:

**Paul David Llontop López-Dávalos**

Asesor:

**Prof. Dr. Jorge Andrés Guerra Torres**

Lima, 2023

## Informe de Similitud

Yo, Jorge Andrés Guerra Torres, docente de la Escuela de Posgrado de la Pontificia Universidad Católica del Perú, asesor de la tesis de doctorado titulada *Characterization of luminescent ITO:Tb and AZO:Tb thin films prepared by radio frequency magnetron sputtering*, del autor Paul David Llontop López-Dávalos

dejo constancia de lo siguiente:

- El mencionado documento tiene un índice de puntuación de similitud de 15.%. Así lo consigna el reporte de similitud emitido por el software *Turnitin* el 29/03/2023.
- He revisado con detalle dicho reporte y la Tesis o Trabajo de Suficiencia Profesional, y no se advierte indicios de plagio.
- Las citas a otros autores y sus respectivas referencias cumplen con las pautas académicas.

Lima, 29/03/2023

Jorge Andrés Guerra Torres	
DNI: 46163725	Firma 
ORCID: 0000-0002-1734-6660	

## Acknowledgements

This manuscript represents the conclusion of a project that started several years ago. Since the start of this journey, different institutions and many people have been involved directly and indirectly in the effort and work I have given to this endeavor.

First, I would like to thank the National Council of Science, Technology and Innovation (CONCYTEC-FONDECYT) for the financial support through a PhD in Physics scholarship and with Prof. Dr. Alberto Gago, Director of the PhD in Physics program at PUCP for allowing my entrance to the program. I am also thankful with the further financial support from DAAD-CONCYTEC grants N. 423-2019 and 57508544, PUCP Research Office and the Office of Naval Research, grant N62909-21-1-2034.

My immense gratitude to my supervisor Prof. Dr. Andrés Guerra for his great support, guidance and opportunities offered throughout all this years. To Dr. Rolf Grieseler for the suggestions and guidance on this work and for being part of the jury in my dissertation defense. To Prof. Dr. Amaru Töfflinger for his valuable ideas and suggestions related to the work presented thesis.

I would also like to thank Dr. Lars Korte, Prof. Dr. Leandro Tessler and Prof. Dr. Francisco Rumiche for being part of the jury for my dissertation defense.

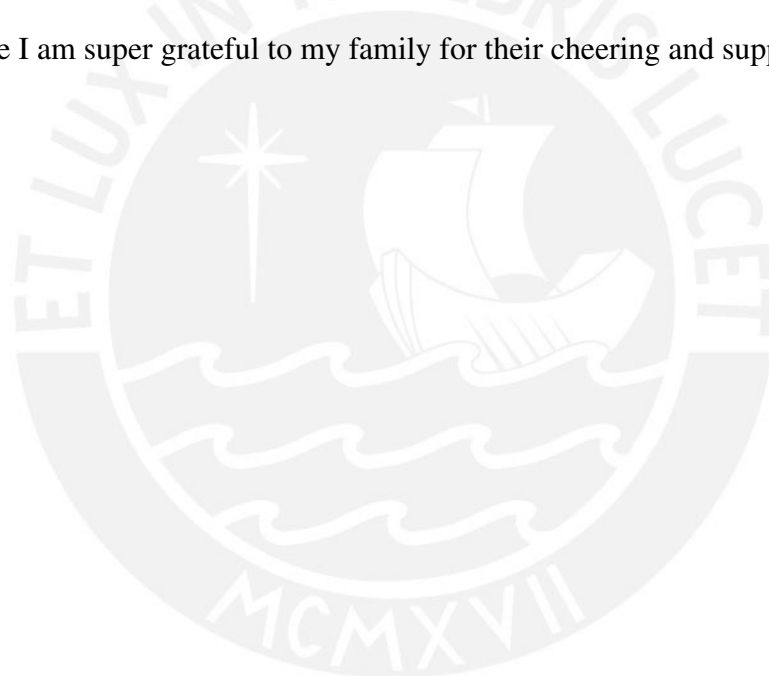
I am also very grateful to Dr. Korte for receiving me to do an internship at the Department of Perovskite Tandem Solar Cells in the Helmholtz-Zentrum Berlin (HZB). I am also thankful to Mrs. Marion Krusche for her great support with the internship arrangements as well as during the stay. I would like to extend my gratitude to Dr. Florian Ruske, Mrs. Carola Klimm and of course Alvaro Tejada for their time and assistance to take the SEM images. I am also very thankful to Alvaro for his guidance and support during the stay at HZB.

I am indebted to Priv.-Doz. Dr. Klaus Habicht for providing access to his lab at the Department of Dynamics and Transport in Quantum Materials at HZB where resistivity and Hall effect measurements were carried out. I am also very grateful to Dr. Gyanendra Panchal for his time and dedication on the Hall setup training.

I would like to extend my gratitude to Priv.-Doz. Dr. Mirosław Batentschuk for receiving me to do an internship at the Institute Materials for Electronics and Energy Technology (I-MEET) at the Friedrich-Alexander-Universität Erlangen-Nürnberg. I extend my gratitude to Dr. Andres Osvet and Dr. Roland Weingärtner for their assistance and suggestions during the stay. I would also like to express a big thanks to Loreleyn Flores for her time and guidance during my stay at I-MEET.

Thanks also to past and present members in the Materials Science and Renewable Energies (MatER) group at Sección Física - PUCP with whom I shared great moments, exchanged ideas and learned so much throughout the period of this work. A special thanks to Carlos Torres who started the work on ITO:Tb during his master thesis and provided me with an excellent starting point to take forward this project.

And of course I am super grateful to my family for their cheering and support over all these years.



## Abstract

This thesis investigates the effects of introducing terbium to indium tin oxide (ITO) and aluminum zinc oxide (AZO) thin films on their electrical, optical and light emission properties. The films were prepared by radio frequency magnetron co-sputtering with active cooling during deposition. The samples maintained a high optical transmittance in the ultra-violet and visible spectral regions. ITO:Tb showed a low electrical resistivity ranging from  $5 \times 10^{-3} \Omega \cdot \text{cm}$  to  $0.3 \Omega \cdot \text{cm}$ , whilst AZO:Tb resulted with a high resistivity which could not be measured with the available equipment. Tb-related luminescence was obtained in ITO:Tb after annealing at  $470^\circ\text{C}$  in air at atmospheric conditions. Contrastingly, AZO:Tb showed characteristic Tb luminescence in the as-grown state and further annealing treatments reduced the Tb-related intensity. For both materials, the optical transmittance was measured at each annealing temperature to track the changes in the optical parameters such as optical band gap and Urbach energy. Additionally, exciton binding energy in the case of AZO:Tb was also registered. Together with cathodoluminescence and photoluminescence (PL) measurements, the compromise between the achieved light emission intensity, optical and electrical properties was assessed for each material. Temperature dependence of the Tb-related luminescence and thermal quenching was assessed by temperature-dependent PL measurements from 83 K to 533 K under non-resonant indirect excitation. Thermal quenching activation energies suggest an effective energy transfer mechanism from the host to the Tb ions. In the case of ITO:Tb, it is assumed that a short-range charge trapping process and subsequent formation of bound excitons to Tb ion clusters is occurring at low sample temperatures. This indirect excitation mechanism is modeled using a spherical potential-well and a tight-binding one-band approximation models. For AZO:Tb, a similar approach is carried out, although the excitons are assumed to be bound to Tb ion clusters or Tb complexes that arise from the coordination with AZO intrinsic defects.

# Table of contents

<b>1</b>	<b>Introduction</b>	<b>1</b>
<b>2</b>	<b>Background theory</b>	<b>4</b>
2.1	Optical models for band-gap estimation in thin films . . . . .	4
2.1.1	Tauc-Lorentz model . . . . .	4
2.1.2	Band-fluctuations model . . . . .	6
2.1.3	Elliot-Band-fluctuations model . . . . .	7
2.1.4	Drude model . . . . .	7
2.2	Luminescence of rare-earth ions . . . . .	8
2.2.1	Rare-earth activation . . . . .	10
2.2.2	Excitation of Rare-earth ions . . . . .	11
<b>3</b>	<b>Methodology</b>	<b>12</b>
3.1	Sample preparation by RF magnetron sputtering and annealing treatments .	12
3.2	Elemental and structural characterization . . . . .	14
3.2.1	Scanning electron microscopy . . . . .	14
3.2.2	Energy-dispersive X-ray spectroscopy . . . . .	15
3.2.3	X-ray diffraction . . . . .	17
3.3	Optical characterization by UV-Vis-NIR spectroscopy . . . . .	20
3.4	Luminescence characterization . . . . .	21
3.4.1	Photoluminescence . . . . .	21
3.4.2	Cathodoluminescence . . . . .	23
3.5	Electrical characterization . . . . .	25
3.5.1	Van der Pauw technique . . . . .	25
3.5.2	Hall effect measurements . . . . .	26

<b>4</b>	<b>Impact of Tb incorporation on the optical, electrical and light emission properties of ITO</b>	<b>29</b>
4.1	Elemental composition and structural characteristics . . . . .	29
4.2	Influence on the optical properties . . . . .	32
4.3	Annealing induced luminescence activation . . . . .	38
4.4	Concentration quenching effect . . . . .	40
4.5	Thermal quenching and excitation mechanism of Tb <sup>3+</sup> luminescent centers in ITO . . . . .	41
4.6	Effects on the electrical properties . . . . .	46
4.7	Summary . . . . .	47
<b>5</b>	<b>Impact of Tb incorporation on the structural, optical and electrical properties of AZO</b>	<b>49</b>
5.1	Effect of post-deposition annealing treatments . . . . .	50
5.1.1	Elemental composition and structural properties . . . . .	50
5.1.2	Optical properties . . . . .	56
5.1.3	Luminescence activation/deactivation . . . . .	63
5.2	On the excitation mechanism of optically active Tb <sup>3+</sup> centers in AZO . . . . .	67
5.2.1	Electrical Properties of AZO . . . . .	73
5.3	Summary . . . . .	75
<b>6</b>	<b>Conclusions</b>	<b>77</b>
	<b>References</b>	<b>80</b>

# Chapter 1

## Introduction

Over the past few decades rare-earth (RE) doped wide band gap semiconductors have attracted great attention as efficient luminescent materials for optoelectronic applications, like photon downshift, as well as down- and up-conversion systems [1, 2], optical amplifiers [3, 4], electroluminescent devices [5, 6], lasers [7, 8], non-contact luminescent temperature sensors [9–11], and photonic structures [12–14]. Recently, RE based down- and up-conversion layers have been effectively integrated in solar cells [15–17]. This is attributed to two principal features. First, a large band gap suppresses the thermal quenching effect at room temperature and, in some cases, even at higher temperatures [18]. This allows RE-related light emission output, for instance, in the visible spectral range covering the colors red ( $\text{Eu}^{3+}$ ), green ( $\text{Tb}^{3+}$ ) and blue ( $\text{Tm}^{3+}$ ) [18–20]. Second, RE-related light emission exhibits long fluorescence lifetimes and narrow spectra, since they result from intra-4f electronic transitions, which are weakly sensitive to the host atomic environment [21–23]. Furthermore, the host's semiconducting properties allow the tailoring of the electrical properties of the material without dramatically compromising its optical properties and light emission capabilities.

These features make RE doped wide band gap semiconductors suitable for light emission applications, as an alternative to direct band gap semiconductor based devices [5, 6], and light conversion applications which can be integrated in solar cells [15–17]. However, the RE-related light emission intensity is sensitive to the host environment, oxygen content, disorder-induced states and other localized electronic states [5, 20–28]. In particular, it is well established that not all the REs embedded in a host are active for light emission, but can be activated through post-deposition thermal treatments [20–23, 28]. These treatments have two effects that may enhance the RE-related light emission intensity. First, annealing may induce the coordination of RE ions with neighboring host ions in a non-centrosymmetric



---

arrangement, thus enhancing the probability of intra-4f electronic transitions. Second, electronic defects such as dangling bonds may also play an important role in energy transfer mechanisms from the host to RE ions. In general, the density of localized states and host related luminescent centers can be thermally enhanced or quenched, affecting the overall RE light emission output [21–29].

In this context, little is known about the light emission features of RE-doped transparent conductive oxides (TCOs) like, for instance, indium tin oxide (ITO) or aluminum doped zinc oxide (AZO), among others. Functional light emitting materials like RE doped TCOs could open applications, such as in low voltage direct current electroluminescent devices [6], or energy-downshift transparent, anti-reflective, and electrically conductive layers. In contrast to traditional wide band gap semiconductors, the electrical conductivity could be high enough to still use the material as a transparent and luminescent electric contact. However, there are only very few and recent published works where TCOs like ITO or AZO have been doped with REs, and very low or no RE-related light emission intensity has been achieved in these systems [26, 30–33]. In contrast, there are reports on the light emission of RE-doped pure binary metal oxides such as zinc oxide (ZnO) [34–36], aluminum oxide (Al<sub>2</sub>O<sub>3</sub>) [37], indium oxide (In<sub>2</sub>O<sub>3</sub>) [38, 39], and tin oxide (SnO<sub>2</sub>) [40, 41]. These materials exhibit an optical transparency suitable for light output from luminescent centers, and a wide band gap capable of overcoming the thermal quenching effect at room temperature. Their optical and electrical properties can be engineered for instance by tailoring the oxygen content during the deposition process or by post-deposition annealing treatments, reducing or increasing in this way the amount of oxygen vacancies, thus reducing (increasing) the electrical conductivity whilst increasing (reducing) its transparency [42]. The absence of Tb emission in previous reports from these ternary compounds might be related to an effective competition between host related recombination centers and radiative recombination involving the REs, in addition to an inhibited thermal activation of the REs due to the absence of a proper crystal symmetry surrounding them.

This thesis addresses the impact of Tb inclusion and following post-deposition annealing treatments on the optical, electrical and luminescent properties of ITO and AZO thin films. Furthermore, it is also the aim of this work to shed some light on the capability of RE doped TCOs to become optically active, while retaining important properties of the host material such as a low resistivity and high optical transmittance in the visible spectral region. In order to make these TCOs active luminescent materials that could make it feasible the improvement, or even develop new, optoelectronic applications, such as in photovoltaics or light-emitting devices, the first objective would be to achieve the characteristic Tb luminescence. And

consequently, investigate which are the conditions and consequences of enabling these materials as luminescent RE hosts. Thus, the scope of this work covers the following: a brief summary of Tb embedded TCOs (Chapter 1), a background theory covering the optical models employed as well as the basics of rare-earth luminescence and its corresponding excitation (Chapter 2), a description of the sample preparation, thermal treatments and methods employed for sample characterization (Chapter 3), the results obtained and a discussion of the results obtained for ITO:Tb (Chapter4) and AZO:Tb (Chapter 5) and the conclusions of the work (Chapter 6).



# Chapter 2

## Background theory

### 2.1 Optical models for band-gap estimation in thin films

This section presents a brief summary of the optical absorption models used to determine and describe the optical properties of the materials investigated in this work. Starting with the Tauc-Lorentz model used to describe the dielectric function of a TCO and the band-fluctuations approach which takes into account the variations at the band edges due to the thermally- and structurally-induced disorder, these models are employed in order to estimate the band gap and Urbach energy of the samples investigated. A further model enhancement for excitonic materials is presented with the Elliot-band-fluctuations model in which the Elliot model is convoluted with the band-fluctuations approach in order to take into account the excitonic absorption enhancement. Finally, the Drude model is presented for the free carrier absorption which has an impact on the dielectric function, mainly in the infrared spectral region, and especially for high carrier concentrations.

#### 2.1.1 Tauc-Lorentz model

The Tauc-Lorentz model has been used to model the dielectric function of amorphous semiconductor [43] and, more recently, it has also been used to describe the dielectric function of transparent conductive oxides [44–46]. In a crystalline semiconductor free of defects, the absorption spectrum would abruptly end at the band gap energy. In amorphous semiconductors, the absorption spectrum exhibits a tail that extends into the gap region and stems from the disorder that is characteristic in these materials. This feature makes the band gap difficult to estimate experimentally [47]. Tauc [48] proposed plotting the quantity  $(\hbar\omega \cdot \epsilon_2^{1/2})$ , where  $\epsilon_2$  is the imaginary part of the dielectric function, against the photon

energy  $E = \hbar\omega$  for amorphous germanium in order to depict a linear region which can be described by taking the positive square root of

$$\varepsilon_2^{Tauc} = A^{Tauc} \frac{(E - E_g^{Tauc})^2}{E^2}, \quad (2.1)$$

where  $\varepsilon_2^{Tauc}$  is the imaginary part of the dielectric function,  $E_g^{Tauc}$  is the Tauc band gap,  $A^{Tauc}$  is a proportionality coefficient and  $E$  is the energy of the incident photon. Thus,  $E_g^{Tauc}$  can be estimated with a linear fit from the so called "Tauc-plot". A similar approach can be used for direct band gap crystalline semiconductors where the quantity  $(\hbar\omega \cdot \varepsilon_2^2)$  is depicted against  $\hbar\omega$ . Tauc's model can be used to describe interband transition mechanism, but does not take into account defect-related or intraband absorption which also take place [43]. The Lorentz model presents a frequency-dependent description of the dielectric function which arises from the classical depiction of an atom in which electrons are bound to the nucleus by a restoring force similar to that of a spring. By assuming an infinite mass for the nucleus and neglecting the small magnetic force due to the interaction between the electron and the magnetic field of the light wave, the model yields a symmetric function for  $\varepsilon_2$  [49]. Nonetheless, amorphous materials generally exhibit asymmetric shapes for  $\varepsilon_2$ . Jellison and Modine [43] developed an enhanced model that can describe this asymmetric shape. The model consists of a convolution of Tauc model and the Lorentz calculation for  $\varepsilon_2$  that is expressed by

$$\varepsilon_2^{TL} = \begin{cases} \frac{AE_0C(E-E_g^{TL})^2}{(E^2-E_0^2)^2+C^2E^2} \frac{1}{E} & E \geq E_g^{TL} \\ 0 & E \leq E_g^{TL}, \end{cases}$$

where the TL superscript represents the parameters in the Tauc-Lorentz model and the four fitting parameters are the proportionality constant  $A$ , the peak transition energy  $E_0$ , the broadening term  $C$  and the band gap  $E_g^{TL}$ .

The real part of the dielectric function,  $\varepsilon_1$ , has a more complicated expression and can be calculated by the Kramers-Kronig relation. It is important to remark that it does not consider the Urbach tail states and although this model was originally developed for amorphous materials, it has been used for crystalline materials with direct gap as well [50].

### 2.1.2 Band-fluctuations model

The band-fluctuations (BF) model describes the experimentally found shape of the fundamental absorption based on equivalently treated thermally-induced and structurally induced band-fluctuations. These fluctuations arise from the disorder-induced local variations at the energy band edges, the thermally-induced potential fluctuations (lattice vibrations), as well as any other deviations from the ideal periodicity of the lattice. Although the absorption tails arising from these deviations can be analyzed with the Urbach rule, which describe an exponential dependence ( $e^{\beta\hbar\omega}$ ) of the absorption coefficient for the tail region, the rule does not account for the optical band gap. The BF model accounts for both the tail and the band gap by introducing a weight distribution function that contains the underlying statistics behind the fluctuations. The weight function is a sigmoidal function that has the Urbach slope  $\beta$  (reciprocal of the Urbach energy  $E_U$ ) as a width parameter. Then, the behaviour of the fundamental absorption thus can be monitored via the estimation of the optical band gap  $E_g$  and the Urbach slope  $\beta$ . A detailed description of the model can be found in Guerra et al. [50]. The model was developed for direct and indirect electronic transition materials. For ITO and AZO, the particular case for direct electronic transitions was employed. Following the relationship between the absorption coefficient  $\alpha$  and the imaginary part of the dielectric function  $\varepsilon_2$ , given by  $\alpha = \frac{E}{\hbar c n} \varepsilon_2$ , the absorption coefficient can be expressed as

$$\alpha(\hbar\omega) = -\frac{1}{2} \frac{\alpha_0}{\hbar\omega} \sqrt{\frac{\pi}{\beta}} \text{Li}_{1/2} \left( -e^{\beta(\hbar\omega - E_g)} \right). \quad (2.2)$$

Here  $\text{Li}_{1/2}(z)$  is the polylogarithm function of order  $1/2$  of  $z$ .  $\beta$  is the Urbach slope, and  $\alpha_0$  is a coefficient proportional to the electronic transition matrix element.

The advantage of using this model for retrieving the optical band gap and Urbach energy is based on the fact that materials with large Urbach tails will exhibit a bias on the band gap when using traditional models. This is due to the large overlap of the Urbach tail with the fundamental absorption onset. Typically, for values of  $E_U$  above 60 meV, a significant deviation between the actual band gap and the retrieved  $E_g$  is found [28, 50–53]. Furthermore, in amorphous materials the band gap estimation is quite challenging due to the tails that extends into the gap region. Since Eq. (2.2) takes into account Urbach tails, the retrieved band gap is typically free of this bias [50].

### 2.1.3 Elliot-Band-fluctuations model

When a photon is absorbed, the resulting electron in the conduction band and hole in the valence band can be attracted to each other by the electrostatic Coulomb force. This attraction correlates their motion and the electron-hole pair is called an exciton. When a photon interacts with an exciton, a coupled state forms called exciton-polariton. The optical absorption in this picture is the conversion of a photon into an exciton. A polariton is a coupled electromagnetic and polarization wave travelling inside a medium. In this case, the electromagnetic wave is associated to the photon, while the polarization wave to the electric dipole moments of the excitons. As polaritons go through the medium they can excite other excitons by their recombination and subsequent emission of electromagnetic waves. In principle, both waves cannot be separated and, in this scheme, their energy will not be lost by photons when getting through the medium. Thus, the energy would be converted from photons to excitons and viceversa. It can occur that when going through the medium, the polariton does not experience loss of energy resulting in no optical absorption inside the medium. For the absorption to occur, polaritons must be scattered by phonons. After this inelastic scattering, some excitons will recombine and their recombination energy will leave the medium in the form of emitted photons with a slightly different energy [54]. Elliot calculated the excitonic-enhanced band-edge absorption coefficient that allows the determination of the exciton binding energy, although it lacks broadening effects [55, 56]:

$$\alpha = \frac{AE_b^{1/2}}{E} \left( 2E_b \sum_{n=1}^N \frac{\delta[E - E_g + E_b/n^2]}{n^3} + \frac{\Theta[E - E_g]}{1 - e^{-2\pi\sqrt{E_b/(E-E_g)}}} \right) \quad (2.3)$$

here  $E_b$  is the exciton binding energy,  $E$  is the photon energy,  $E_g$  the band gap,  $A$  is a energy-independent constant and  $\Theta$  is the Heaviside step function. The broadening due to phonon interaction, thermal disorder and structural disorder in the material can be taken into account by introducing the band-fluctuations approach described in the previous section. Thus, the model is the result of a convolution between the Elliot formula shown in Equation (2.3) and the band-fluctuations distribution described in the previous section. We use this approach to calculate the free exciton binding energy,  $E_b$  from optical absorption data. The extended model has been developed within our research group [57].

### 2.1.4 Drude model

The presence of free carriers in a material have an impact in the dielectric function. In particular, free carriers induce the optical absorption in the infrared region, depending

on the carrier concentration and mobility. When a semiconductor has a high free-carrier concentration (above  $\sim 10^{18} \text{ cm}^{-3}$ ), the excess carriers fill more states in the conduction band (electrons) or valence band (holes). Thus, the Fermi level start shifting to a higher energy inside the conduction band and the semiconductor exhibits metallic behaviour. When the carrier concentration  $N$  of the semiconductor increases, the absorption coefficient of the free carrier absorption ( $\alpha_{FCA}$ ) also increases, so the optical absorption takes place with more probability at low photon energies [58]. The dielectric function given by this model is

$$\varepsilon = \varepsilon_{\infty} \left( 1 - \frac{\omega_p^2}{\omega^2 - i\omega\Gamma} \right), \quad (2.4)$$

where  $\varepsilon_{\infty}$  is the high-frequency dielectric constant and  $\omega_p$  is the plasma angular frequency given by

$$\omega_p = \left( \frac{e^2 N}{\varepsilon_0 \varepsilon_{\infty} m^*} \right)^{1/2}. \quad (2.5)$$

For semiconductors,  $\omega_p$  is in the infrared region. Finally,  $\Gamma$  is defined as  $\Gamma = \frac{e}{m^* \mu}$ , where  $e$  is the electron charge,  $m^*$  is the free carrier effective mass and  $\mu$  is the drift mobility of the carriers.

## 2.2 Luminescence of rare-earth ions

The rare-earth (RE) or lanthanide series is composed of 15 elements with atomic numbers from 57 to 71. Within the periodic table, they are located in the first row of the f-block. Following the Aufbau principle and Madelung's energy ordering rule, the 4f orbitals start being filled after the 5p and 6s subshell have been filled. Although these orbitals are part of the valence configuration, they are shielded from the chemical environment by the 5s and 5p orbitals that are already filled. This shielding occurs in their ground state as well as in any higher oxidation state.

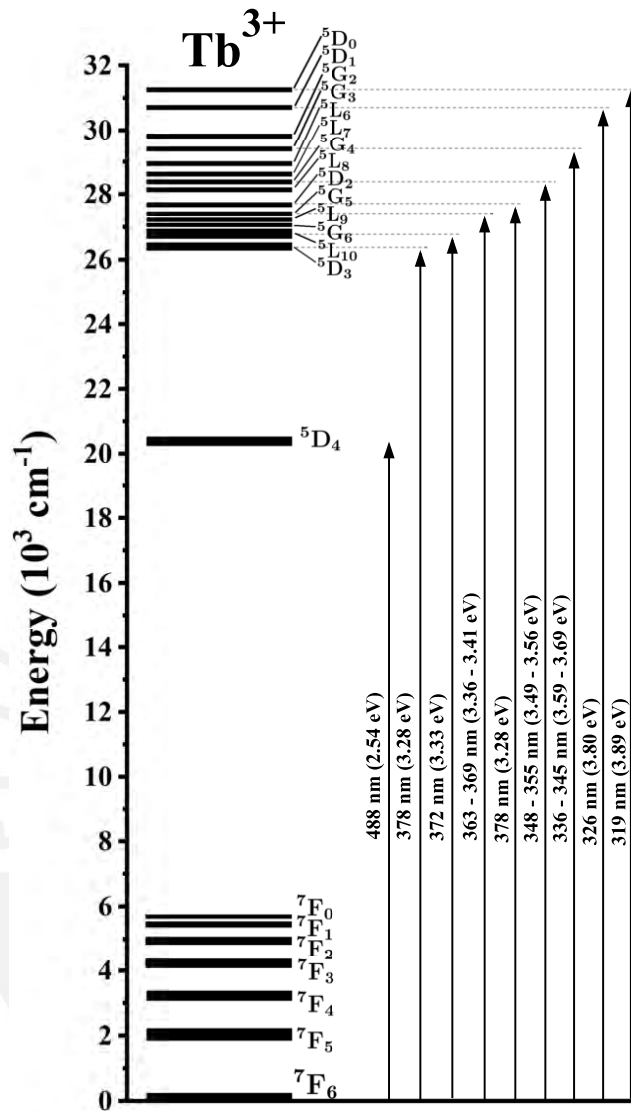


Fig. 2.1 Partial energy diagram for the Tb<sup>3+</sup> ion. The main luminescent levels are the <sup>5</sup>D<sub>3</sub> and <sup>5</sup>D<sub>4</sub>, while the fundamental is <sup>7</sup>F<sub>6</sub>. Adapted from Baur et al. [59]

This implies that the chemical environment of the rare-earth ion has little impact on the energy levels of the 4f orbitals. Every RE atom has a ground state as well as excited states. These states are degenerate for a given electronic configuration of a 4f-configuration element. Said degeneracy is lifted when electron-electron interactions and spin-orbit coupling are taken into account, resulting in a large number of non-degenerate levels for each RE [60].

When introducing Tb in a host material, both Tb<sup>3+</sup> and Tb<sup>4+</sup> valence states can be present. The latter is known not to give any emission and can also act as luminescence killer of



Tb<sup>3+</sup> emission due to its broad and strong absorption in the visible region. Tb<sup>3+</sup> ions show characteristic emission in the UV range but mostly in the visible range. Figure 2.1 shows the energy levels corresponding to the Tb<sup>3+</sup> characteristic transitions. The main excited energy levels from which electronic transitions exhibiting luminescence are observed are <sup>5</sup>D<sub>3</sub> and <sup>5</sup>D<sub>4</sub>. The energetic differences between these two levels and their nearest energy level below are wide in comparison to those located above the <sup>5</sup>D<sub>3</sub> and below the <sup>7</sup>F<sub>0</sub>, thus favoring photon emission.

The spectroscopic levels described correspond to the electronic levels for the free ion in a spherical symmetry. When a ligand bonds with this ion, the geometry is not spherical anymore and depends on the symmetry of the surrounding coordination. The representation of the ligands that are coordinated to the lanthanide can be thought as points around the ion that generate an electrostatic ligand or crystal field surrounding the lanthanide ion. This electric field further split the spectroscopic levels (those in Figure 2.1) into sublevels and their fine structure will determine the corresponding symmetry around the ion [61].

### 2.2.1 Rare-earth activation

In general, there are three kinds of electronic transitions that can take place in rare-earths: intra-4f level, 4f-5d and charge transfer transitions. Not all these electronic transitions are allowed, thus making the RE ion inefficient at absorbing light. Nonetheless, the permitted transitions are described by selection rules which, whenever the RE ion is under the influence of a non-centrosymmetric crystal field, can allow the forbidden transitions. Laporte's parity selection rules says that electronic states with same parity are unable to interact with each other via electric dipole interaction, thus making the f-f (intra-4f) transitions forbidden. When the ion is affected by the crystal field, the interactions result in mixed opposite parity electronic states, thus relaxing the selection rules and making the electric dipole intra-4f transition partially allowed. Note that the terms "forbidden" and "allowed" transitions are not exactly accurate, as they refer to the degree of probability for a transition to occur. A forbidden transition is less likely to happen, while an allowed transition has a higher probability to take place [62]. Overall, RE luminescence is influenced by its atomic environment within the host where it is embedded. In turn, said environment can be influenced by thermal treatments which could alter the structure resulting in a favorable condition for RE-related light emission.

### 2.2.2 Excitation of Rare-earth ions

The excitation of RE ions can occur directly, i.e. the energy matches an intra-4f absorption transition, and indirectly involving another ion, electronic state, defect or compound, called sensitizer. The sensitizer intervenes by absorbing light from the excitation source and transferring it to the RE ion. Since the dipole strengths of intra-4f transitions are rather small, direct excitation does not usually result in highly luminescent materials. In the indirect excitation case, depending on the excited states of the sensitizer, the energy could be transferred back from the RE ion to the sensitizer, thus acting as a luminescence quencher [61].

Sensitization of a rare-earth ion in a solid host or matrix can be done by energy transfer from a surrounding host ion in an excited state. This type of energy transfer is by means of quantum mechanical resonance and, in the case of RE excitation, the host ion would be called donor while the RE ion acceptor. This mechanism is known as Förster mechanism of resonant energy transfer which relies on the Coulomb interaction and dipole-dipole coupling between the acceptor and donor. The energy is transferred non-radiatively from the excited donor to an electron in the acceptor. Dexter [63] extended this theory including higher order multipolar and exchange interaction effects. In the former case, such as, for instance dipole-dipole or dipole-quadrupole, the energy transfer probability will depend on the overlapping of the donor emission and the acceptor absorption spectra. Thus, it will depend on the degree of resonance between both. When emission and absorption transitions are of electric dipole character, the Förster resonant transfer probability is proportional to  $R^{-6}$ , where R is the separation distance between donor and acceptor.

In the case of the exchange interaction energy transfer, also known as Dexter energy transfer, the energy donor and an acceptor must be very close to each other so that their wavefunctions overlap and the excitation energy is transferred from donor to acceptor due to a quantum mechanical exchange interaction between both. The Dexter energy transfer probability is proportional to a decreasing exponential of the separation distance R. As the exchange interaction requires the overlapping of the donor and acceptor electron clouds, the acceptor ion must not be farther than the second nearest site in the host matrix. Although this interaction requires the spectral overlap for resonance as in the multipolar interaction, the spectral intensities will not depend on it. If the acceptor ion is located next to the donor and the emission or absorption transitions are electric dipole forbidden, the probability of the exchange interaction transfer can be larger than for multipolar interactions [64].

# Chapter 3

## Methodology

This chapter presents the experimental methods and theoretical background employed to investigate and analyze the impact of Tb introduction and annealing treatments on ITO and AZO thin films prepared by radio frequency magnetron sputtering. Elemental composition was estimated using Energy Dispersive X-ray spectroscopy (EDS). Structural properties were studied by means of scanning electron microscopy (SEM) and X-ray diffraction (XRD), optoelectronic properties via UV-Vis-NIR transmittance spectrophotometry, while luminescence properties were studied via cathodoluminescence (CL) and (temperature-dependent) photoluminescence (PL). Photoluminescence excitation (PLE) was also employed on a few selected samples. Electrical properties were investigated by means of Van der Pauw method and DC Hall effect.

### 3.1 Sample preparation and annealing treatments

One of the most used physical techniques to prepare transparent conductive oxides thin films is sputtering. It consists of the removal of mass from a material (a target) by means of collisions of energetic ion bombardment [65]. This provides the vapor influx of the material to be deposited on a strategically positioned substrate surface. Among the different sputtering techniques, one of the most used is radio frequency magnetron sputtering (RFMS) which is particularly effective for non-conductive target materials. The samples studied in this work were prepared with a RF magnetron co-sputtering system designed in our laboratories. A schematic is shown in Figure 3.1 a). It shows the sputtering targets employed to prepare the AZO:Tb films. The sample holder was rotated at a constant frequency and cooled actively with a circulating water system set at 13 °C in order to reduce the temperature of

Table 3.1 Sputtering and annealing parameters for the preparation of ITO:Tb and AZO:Tb samples.

	ITO:Tb	AZO:Tb
Targets	90:10 wt% In <sub>2</sub> O <sub>3</sub> :SnO <sub>2</sub> Tb	98:2 wt% ZnO:Al <sub>2</sub> O <sub>3</sub> Tb
Power	ITO 100 W Tb 0 and 10 W	AZO 100 W Al 60 W Tb 0 to 65 W
Substrates	Fused Silica (FS) / Si	
Base pressure	$\sim 1.0 \times 10^{-6}$ mbar	
Ar influx	30 sccm	
Working pressure	$1.0 \times 10^{-2}$ mbar	
Sample holder Temperature	$\sim 80$ °C	
Sample holder Rotation frequency	No rotation	4 min <sup>-1</sup>
Annealing atmosphere	Air	Air, Argon
Annealing temperature range	150 °C - 650 °C	FS: 200 °C - 700 °C Si: 200 °C - 1000 °C

the substrates. A similar approach was employed for the ITO:Tb films where only ITO and Tb targets were used, while the sample holder was placed still to obtain a Tb gradient as shown in Figure 3.1 b). For all the samples, high purity argon gas was employed as the sputter gas and was constantly introduced at a working pressure of  $\sim 1 \times 10^{-2}$  mbar during the deposition process. An undoped set of ITO and AZO films were prepared and annealed in similar conditions to be taken as reference samples in order to evaluate the effect of both Tb inclusion and annealing treatments on their properties. In the case of AZO, an Al target was purposely employed for all AZO and AZO:Tb samples as a way to increase Al concentration. Full setup parameters employed for sample preparation and annealing treatments are shown in Table 3.1.

In order to study the impact of post-deposition annealing treatments, the samples were annealed inside a quartz tubular vacuum furnace at atmospheric pressure within air ambient. One set of AZO samples and one set of AZO:Tb samples were annealed under argon ambient at a pressure close to  $4.0 \times 10^{-1}$  mbar. Temperature behaviour for  $\sim 60$  minutes inside the furnace is shown in Figure 3.2, monitored with a thermocouple at the point where samples were to be placed for the treatments. The procedure was in thermal-shock, i.e. the tube was introduced into the furnace after temperature stabilization was achieved. Heating rates were estimated from the linear region of the curves between minutes 2 and 5. Annealing treatments to the samples were done for 4 hours after the tube was introduced. Afterwards, the tube and

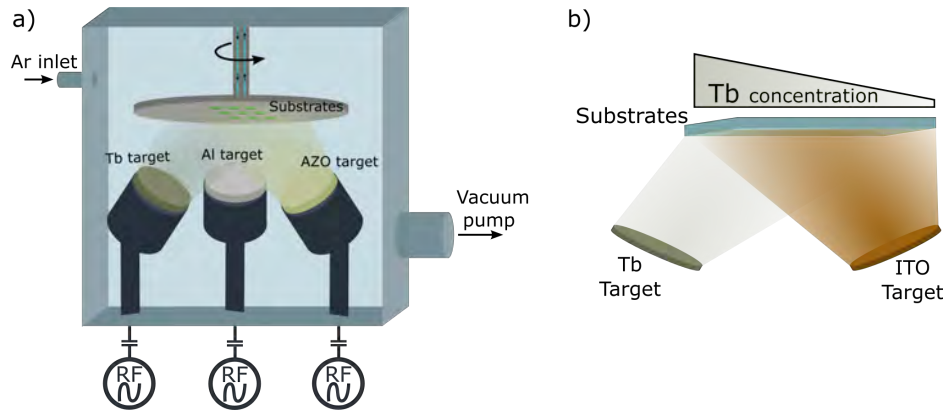


Fig. 3.1 a) Schematic of the sputtering chamber for AZO:Tb sample preparation. Sample holder and magnetrons were water cooled, the former being rotated during deposition. b) Schematic configuration of ITO and Tb targets in order to obtain a Tb gradient in the samples.

samples were taken out of the furnace and soft cooled till room temperature (RT). Cooling behaviour can be observed also in Figure 3.2. One set of AZO and one of AZO:0.8 at.%Tb samples were annealed in argon ambient at  $1.5 \times 10^{-2}$  mbar for comparison purposes.

## 3.2 Elemental and structural characterization

In order to investigate the effects on the elemental composition of ITO and AZO films when introducing Tb, energy dispersive X-ray analysis was carried out on samples in both as-grown and annealed states. Their structural characteristics were studied by taking scanning electron micrographs of the surface and cross-section, while X-ray diffractograms were obtained in the Bragg-Brentano configuration in order to estimate their structural parameters.

### 3.2.1 Scanning electron microscopy

One way to investigate the structural properties of a material is by means of scanning electron microscopy. This technique is based on the interaction between a beam of accelerated electrons and the material to be investigated. This interaction produces different kind of signals, as can be seen in Figure 3.3, such as secondary (SE), back-scattered (BSE) and Auger electrons, as well as characteristic X-rays and cathodoluminescence (CL). The interaction volume, generally described as "pear-shaped", and escape depth within the sample also vary with the type of signal [66].

In this work, SEM images of AZO and AZO:Tb surfaces and cross-sections were taken with a ZEISS Merlin scanning electron microscope equipped with a field-emission gun

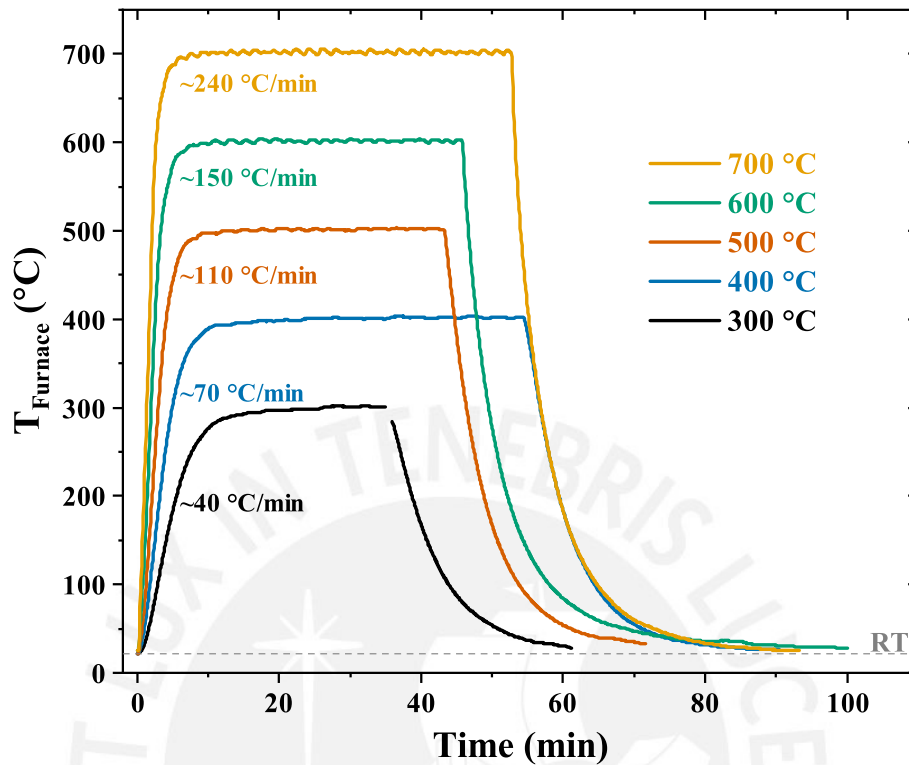


Fig. 3.2 Behaviour of the temperatures measured at the site of the sample during annealing process. Approximate heating rate for each shown temperature can be observed at the left side of the curves. Cooling region corresponds to the soft natural cooling of the samples after taking out the quartz tube from the furnace.

provided by the Department of Perovskite Tandem Solar Cells at the Helmholtz-Zentrum Berlin. Necessary adjustments to obtain the images were done to the gun current, electron acceleration voltage and working distance. Samples on Si substrate were carefully prepared for top, cross-section and 25° tilted cross-section views.

### 3.2.2 Energy-dispersive X-ray spectroscopy

Generated Characteristic X-rays can be detected with an energy dispersive spectrometer (EDS). The incoming X-rays experience inelastic scattering in the detector generating electron-hole pairs which are separated by an electric field inside. Typically, a silicon drift detector (SDD-EDS) is used, where the separated electrons are collected in a central anode. The energy of the X-ray photon is determined by the charge accumulated at the anode and its value is assigned to a certain energy bin. The measurement is shown as a histogram

where the horizontal axis is a series of energy bins, and the vertical axis is the number of photons whose energy correspond to a certain bin. [66, 67].

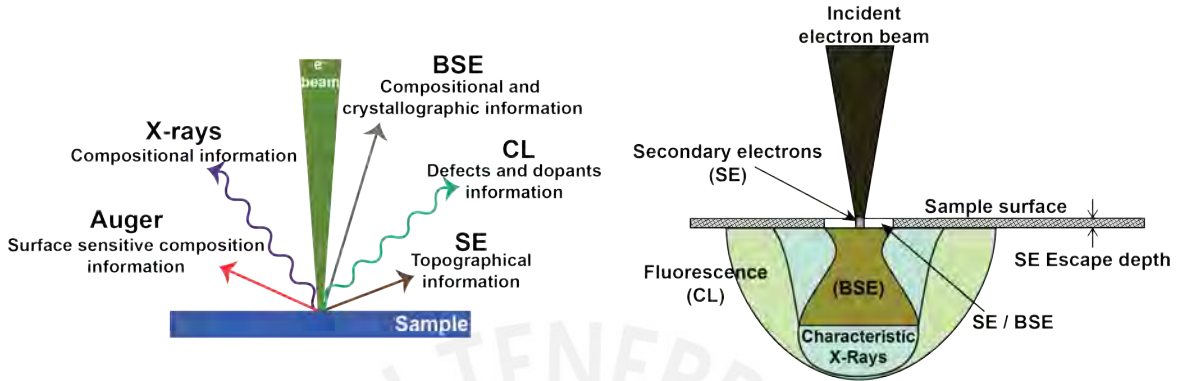


Fig. 3.3 Schematic drawing of signals created and the corresponding information they give from the sample (left) and of the interaction volume between incident electrons and the material tested (right). The escape depth is also sketched with different colors. Both the interaction volume and the escape depth define the spatial resolution of each signal.

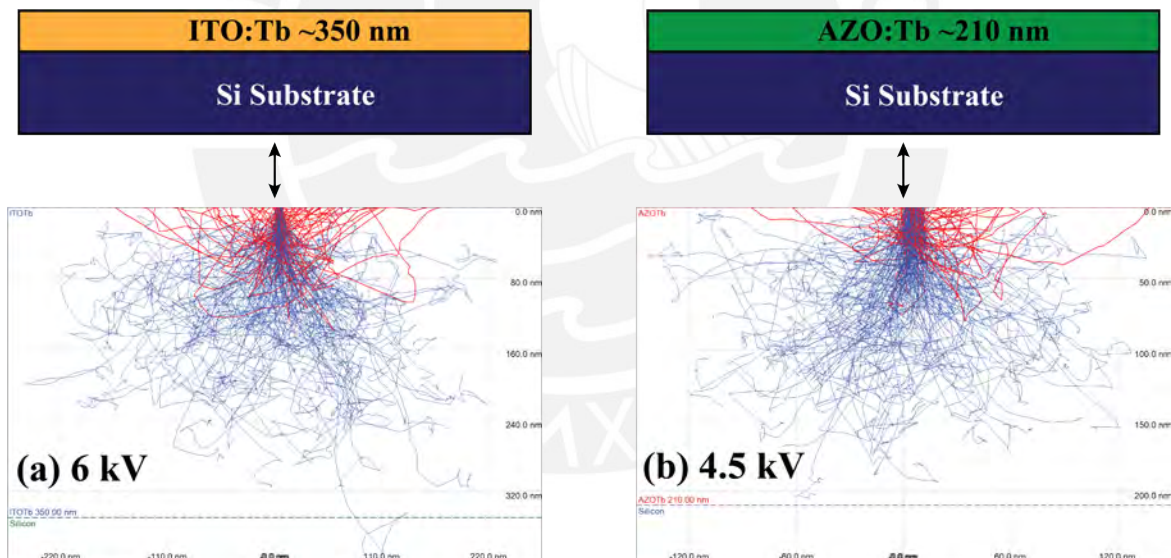


Fig. 3.4 Monte Carlo simulation of the penetration depth and trajectories of secondary (blue lines) and back-scattered (red lines) electrons in ITO:Tb (a) and AZO:Tb (b). The corresponding acceleration voltages of 6 kV and 4.5 kV, respectively, were taken as the acceleration voltages when measuring the samples. The simulation was made in the CASINO program.

A penetration depth simulation was performed in the program Monte Carlo simulation of electron trajectory in solids (CASINO v2.51) [68–71] in order to estimate the acceleration voltages needed to obtain information from the film only. Figure 3.4 shows the penetration

depth and trajectories in an ITO:Tb film (a) with a thickness of 350 nm, while (b) shows the same in an AZO:Tb sample of 210 nm. Both thicknesses values correspond to the smallest thickness of each set of samples, thus incident electrons will not interact with the substrate when testing thicker film samples.

The elemental composition of the samples measured in this work was estimated using a scanning electron microscope FEI Quanta 650 equipped with a tungsten filament and an EDAX energy dispersive X-ray detector, provided by the Materials Characterization Center at PUCP (CAM-PUCP). The quantification was made with EDAX TEAM EDS analysis system, employing the standardless ZAF correction procedure [67, 72]. Electrons were accelerated with 6 kV for ITO and ITO:Tb films, while 4.5 kV was applied to measure AZO and AZO:Tb samples, and the magnification was fixed at  $\times 200$ .

### 3.2.3 X-ray diffraction

When X-rays pass through a material, they get scattered mostly by electrons within it. Scattering power increases with atomic number ( $Z$ ). For instance, Pb ( $Z = 82$ ) is used as X-ray shielding, while Be ( $Z = 4$ ) is used in windows for X-ray transmission. By assuming a simple model where the X-rays are scattered by parallel planes formed by atoms and each plane is a source of scattering, the diffracted radiation features can be described as constructive and destructive interference (Bragg's law). Bragg's law states that for constructive interference to occur, the path difference between the scattered waves must be an integer multiple number of wavelengths. For the  $n$ th order of diffraction, Bragg's law can be written as

$$n\lambda = 2d \sin \theta. \quad (3.1)$$

If X-rays with a known, single wavelength  $\lambda$  irradiate the material, and the angles  $\theta$  are measured at which diffraction peaks appear, the interplanar spacing  $d$  can be determined [73]. There are different geometrical approaches to measure XRD from a sample. For polycrystalline materials, most X-ray diffractometers are configured in the symmetrical or Bragg-Brentano setup, which operating principle can be seen in Figure 3.5. As the sample is not exactly on the circumference, the diffracted beam will be slightly defocused at the detector, mainly due to the beams that come from around the center of the sample. Curved samples would not be practical, thus a close approximation to these ideal conditions can be achieved by placing the sample as shown in Figure 3.5 or even tangent to the focusing circle [74].



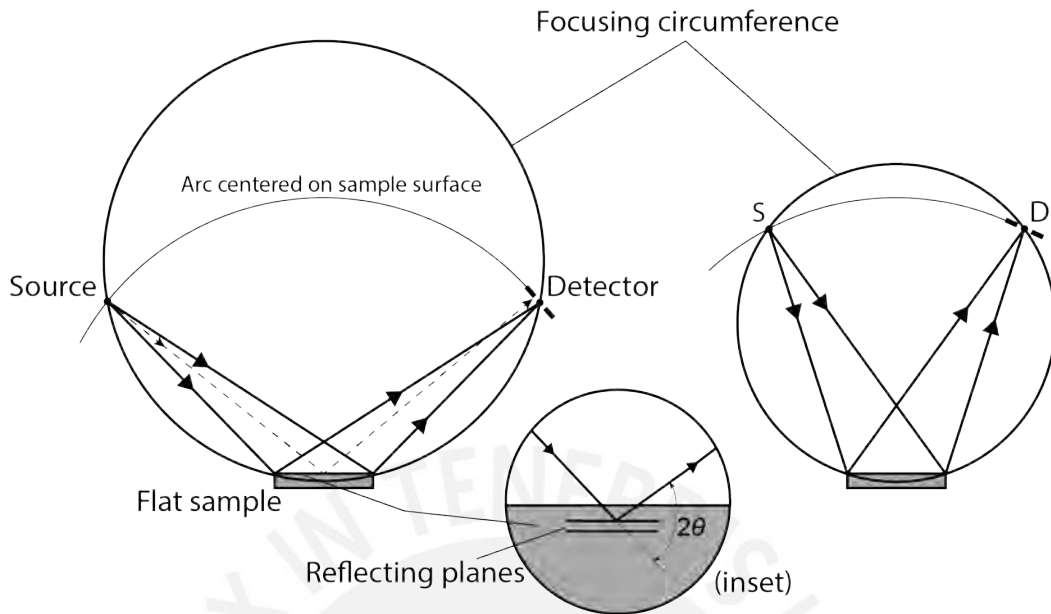


Fig. 3.5 Operating principle of symmetrical or Bragg-Brentano configuration for low angle (left) and high angle (right) of incidence. The source (S) and detector (D) can be moved in opposite directions simultaneously along the arc centered on the sample surface. An imaginary focusing circumference is also sketched and it can be seen that its size is reduced when increasing the angle of incidence. The diffracted beam will be defocused at the detector due to the sample being not aligned within the circumference.

To investigate thin films, using a fixed small angle for the X-ray source can be favorable due to strongly reduced penetration depths and an increased size of the irradiated area on the sample. This grazing incidence configuration is shown in Figure 3.6. The incident X-rays are made parallel by means of a parabolic Göbel mirror which acts also as a filter. The detector is continuously varied along the arc of the circumference centered on the sample to register the diffraction peaks at each  $2\theta$  position.

The structure of the ZnO, AZO and AZO:Tb samples in this work was investigated using a Bruker D8 Discover in the Bragg-Brentano (BB) as well as in grazing incidence (GI) configuration, measured at the Materials Characterization Center at PUCP (CAM-PUCP). BB measurements were done using a rotatory sample holder with fixed X, Y, Z positions. No rotation was applied for every measurement. The X-ray source was a Cu anode and a Ni film was employed to filter the Cu- $K_{\beta}$  X-rays. Automatic slits were placed at both the primary and secondary arms on the goniometer. GI measurements were carried out using a XYZ sample holder, maintaining fixed X and Y positions, while changing Z according to a Z scan correction procedure done for each set of samples. The beam was made parallel by

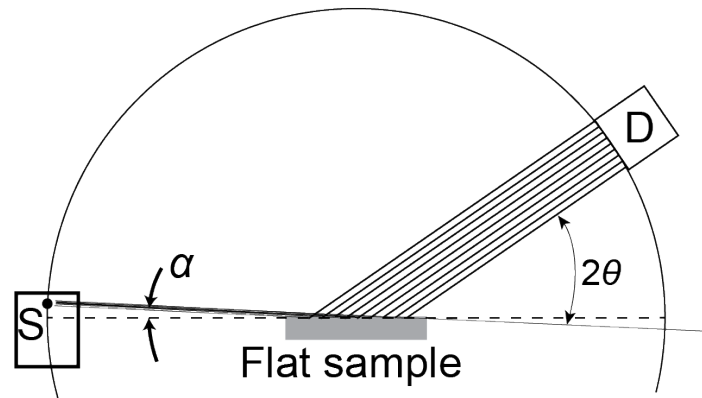


Fig. 3.6 Operating principle of the grazing incidence configuration. The X-ray source is fixed at a small angle ( $0.1 < \alpha < 3^\circ$ ) and the incident rays are parallel to each other. The  $2\theta$  angle is continuously varied by tracking the detector round the arc of the circumference centered on the sample.

means of a parabolic Göbel mirror which also filtered the  $\text{Cu-K}\beta$  rays. Incident angle was kept at  $2^\circ$  for all samples.

Diffractograms were analyzed by subtracting the background and identifying the peaks by comparison with powder diffraction files, such as PDF 89-4598 for ITO and ITO:Tb and PDF 36-1451, for ZnO, AZO and AZO:Tb. Afterwards, crystallite size in the samples was estimated with the Scherrer equation,

$$D = \frac{K\lambda}{\beta \cos \theta}, \quad (3.2)$$

where  $\theta$  is angle of incidence,  $\lambda$  is the X-ray wavelength,  $K$  is the Scherrer constant which is a correction factor that accounts for the particle shape in the polycrystalline sample, and  $\beta$  is the breadth of the diffraction maximum.  $\beta$  can be defined as the integral breadth, which is defined as the ratio of the diffraction peak area and the maximum intensity of the peak.  $\beta$  would be the width of a rectangle with the same area and height as the peak [75]. The Scherrer constant  $K$  can take values close to 1, for instance 0.89 for spherical crystallites and 0.94 for cubic crystallites. By using the integral breadth  $\beta$ , the evaluation of equation (3.2) is approximately independent of the distribution in size and shape and  $K$  can be assumed to be 1 [76].

Additionally, Rietveld refinements were carried out for the ITO, ITO:Tb, ZnO and AZO samples with the software TOPAS5 from BRUKER. Initial parameters to carry out Rietveld refinements for ITO and ITO:Tb were taken from the PDF 89-4598, while for pure ZnO and

AZO films initial values were taken from the PDF 36-1451 [77]. This approach is similar to that used in the literature to investigate ZnO, AZO and GZO [78, 79] where the original model was taken from Abrahams and Bernstein [80] for ZnO.

### 3.3 Optical characterization by UV-Vis-NIR spectroscopy

When a sample is irradiated by light with a certain angle of incidence, the light goes through its surface to interact with the volume of the sample. Thus, it is to be expected that its surface and interfaces play an important role for its optical behaviour. Light could be absorbed at the surfaces or in the volume, and afterwards it could leave the sample by being transmitted through it. Light can also interact with the sample by being specularly reflected or diffusely scattered at the surface.

Usually, the ratio of the intensity of these signals to the total incident light intensity ( $I_0$ ) are defined as

- *Transmittance* ( $T$ ), ratio of the transmitted light intensity  $I_T$  and  $I_0$ ,  $T \equiv \frac{I_T}{I_0}$ .
- *Specular reflectance* ( $R$ ), ratio of the specularly reflected intensity  $I_R$  and  $I_0$ ,  $R \equiv \frac{I_R}{I_0}$ .
- *Optical Scatter* ( $S$ ), ratio of the intensity of scattered light  $I_S$  and  $I_0$ ,  $S \equiv \frac{I_S}{I_0}$ .
- *Absorptance* ( $A$ ), ratio of the absorbed light intensity  $I_A$  and  $I_0$ ,  $A \equiv \frac{I_A}{I_0}$ .

The conservation of energy states that  $T + R + A + S = 1$ .

Measurement of the transmittance  $T$  could be one of the most simple methods to study the optical properties of the material. To measure it, a spectrophotometer is used which can detect in the UV, visible and part of the middle infrared spectral regions. An schematic of the setup is shown in Figure 3.7. There are special attachments for the setup to measure the specular reflectance and the backscattered light such as an integrating sphere, where the light is collected and measured with a detector [81].

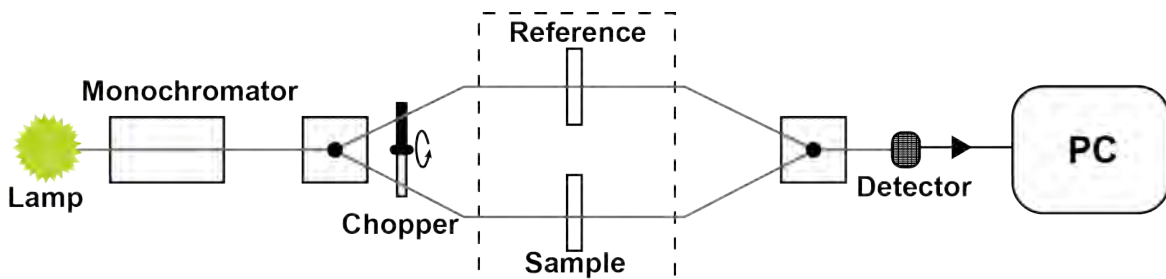


Fig. 3.7 A simple schematic of a double beam dispersive spectrophotometer.

For this work, single optical transmittance measurements were carried out to analyze the optoelectronic properties of the samples. The measurements were performed using a Perkin Elmer Lambda 950 double beam UV-Vis-NIR spectrophotometer. Analysis of the transmittance spectra was made with a modified envelope method [82] to obtain the thicknesses and optical constants such as refractive index, absorption coefficient and the complex dielectric function. The band gap energy was estimated by modeling the absorption coefficient with a band-fluctuations (BF) model for direct materials [50]. For the particular cases of both ITO and ITO:Tb samples, a full spectrum analysis using Drude and Tauc-Lorentz oscillators was performed to determine the charge carrier concentration and mobility by means of the software SpectraRay from SENTECH instruments, considering that the Tauc-gap is not the real band gap. The optical system was modeled by two layers with different Drude parameters but same Tauc-Lorentz parameters. This approach was taken due to, first, the growth-induced microstructure sputtered ITO layers exhibit, and second, the low penetration depth in the high absorption spectral region where the Tauc-Lorentz oscillator has the most influence [83–88]. Additionally, the absorption coefficients of ZnO, AZO and AZO:Tb samples were modeled with a convoluted Elliot-BF model to take into account the excitonic interactions that influence the photonic absorption near the band-edge.

## 3.4 Luminescence characterization

### 3.4.1 Photoluminescence

When a photon of a certain energy within the optical spectrum (UV, Visible or NIR) is absorbed by an electron, it goes into an excited state. Photoluminescence occurs when this optically excited electron returns to its ground state by emitting new photon(s) with energies also within the optical spectrum [89]. A schematic diagram of the setup can be seen in Figure 3.8. The light source could be a lamp together with a monochromator to select the excitation wavelength or only a laser beam. The light emitted from the sample goes through a second monochromator which selects the wavelength to be analyzed and finally gets into the detector. The main components are connected to a computer to monitor and control the parameters. In the setup in which both excitation and emission monochromators are present, two types of spectra can be registered:

- The emission spectrum, which is obtained by fixing the excitation wavelength of the light source with the excitation monochromator (or just using a laser) and the emitted light intensity from the sample is measured by sweeping through a range of wavelengths with the emission monochromator.

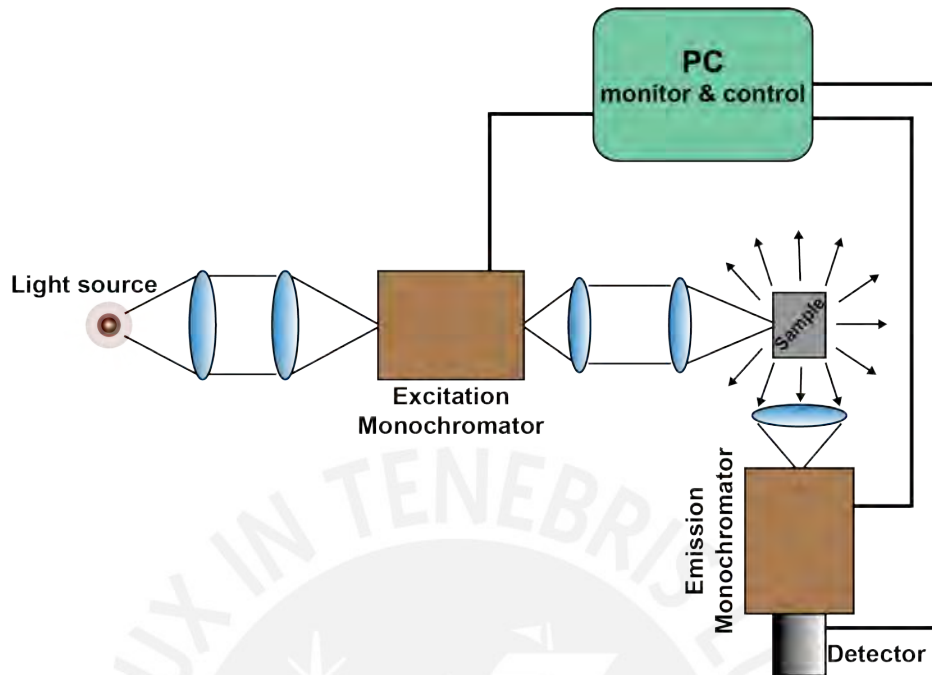


Fig. 3.8 A simple schematic diagram of a PL setup where both emission and excitation spectra could be registered. Both the lamp and excitation monochromator could be replaced by a laser as light source.

- The excitation spectrum, where the emission monochromator is fixed at a certain emission wavelength of interest whilst the excitation wavelength is swept within a spectral range.

To investigate the photoluminescent emission of the samples in this work, PL measurements were performed in a back reflection geometry using a Renishaw micro-Raman inVia spectrometer. The excitation wavelengths were 325 nm and 488 nm from an He-Cd and Argon laser, respectively. The former as means to make a quasi-resonant excitation with the band gap in the case of ITO/ITO:Tb and band-to-band excitation in the case of AZO/AZO:Tb, while the latter was used to make resonant excitation with the  $^5D_4 \rightarrow ^7F_6$  transition of the  $Tb^{3+}$  ion.

To further investigate potential excitation mechanisms of the Tb ions, temperature dependent PL measurements were carried out using a Linkam cooling stage to control the temperature with a liquid nitrogen inlet in the temperature range from 83 K to 533 K. The procedure was to cool down the sample to the lowest temperature at first and then measure PL at each temperature set-point with increasing steps of 20 K.

### Spectra analysis

In order to study the impact of annealing treatments on the  $Tb^{3+}$  luminescence intensity in both ITO and AZO, PL (and CL) spectra were analyzed by subtracting the baseline or background from the full spectrum in order to get the Tb-related light emission spectrum. In the case of ZnO and AZO, the near-band-edge or excitonic emission was also taken as a separate region. For instance, Figure 3.9 shows a PL spectrum of AZO:Tb and ITO:Tb and the corresponding areas or integrated emission intensities for the background (host-related) in red and the Tb-related emission in blue. To investigate the behaviour of the Tb-related luminescence with annealing treatments and Tb concentration, a normalization of the integrated emission was done by taking the ratio of each area to the total area. Thus, the normalized integrated background intensity is  $A_1 / (A_1 + A_2)$ , while the normalized intensity corresponding to the Tb-related emission is  $A_2 / (A_1 + A_2)$ .

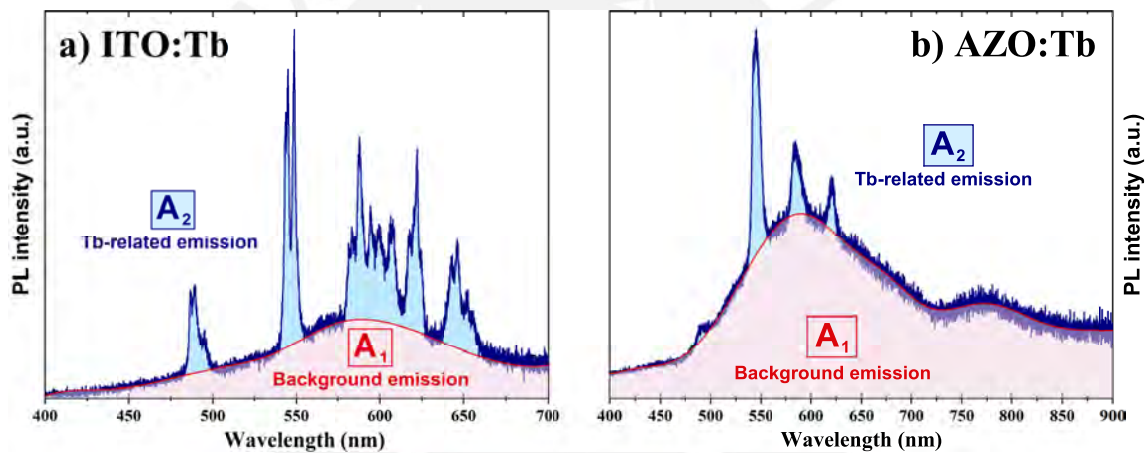


Fig. 3.9 Spectral intensity areas corresponding to the background ( $A_1$ ) and Tb-related emission ( $A_2$ ).

### 3.4.2 Cathodoluminescence

In cathodoluminescence, the excitation source are highly energetic electrons, also called "hot electrons", which are accelerated from the filament of a SEM cathode. As seen in section 3.2.1, one of the signals that comes from the interaction between the beam of electrons and the material tested is cathodoluminescent light, which is emitted by means of different radiative electronic transitions. The fundamental principle behind the generation of cathodoluminescence is based on the inelastic scattering of the incident electrons within the material. The hot electrons reduce their kinetic energy by transferring it, for instance, to weakly bound valence electrons, promoting them to the conduction band, thus generating an

electron-hole pair. As there is a very high density of energetic electrons being scattered, the excitation density is also very high in comparison with PL. In general, for a "pure" material, possible energy transitions and resulting photon emission are given by its intrinsic properties such as band gap energy ( $E_g$ ) and defect energy levels, rather than extrinsic impurity atoms. Electrons at the top of the valence band can receive a wide range of energies which will depend on the details of the inelastic scattering process and, in turn, the spectrum registered from the recombination of electrons and holes would result in a broad band CL emission.

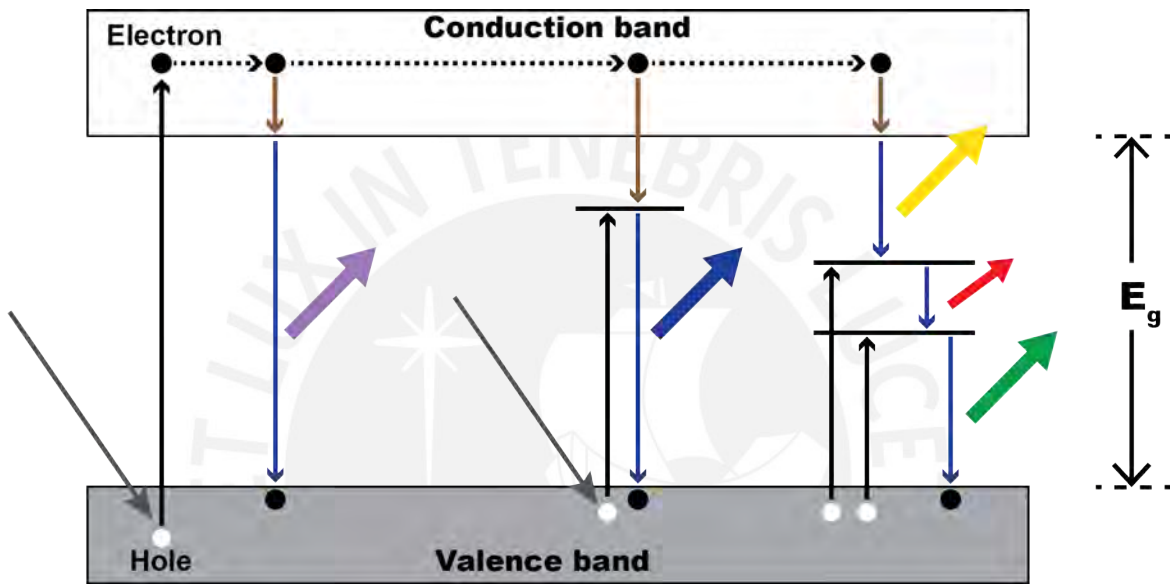


Fig. 3.10 Schematic of possible CL transitions. The initial excitation is by inelastic scattering of a hot electron to promote a valence band electron to the conduction band. Thermalization of this excited electron to the conduction band edge could lead to a recombination with a hole in the valence band followed by the emission of a photon with the corresponding transition energy. The excited electron might find another way to return to the valence band by transitioning non-radiatively (or radiatively) to an impurity level inside the band gap, followed by a radiative recombination with a hole. The wide range of energies that can excite electrons from the valence band could also promote them directly to these impurity levels, after which a radiative recombination could follow.

When the material has extrinsic impurity atoms, energy levels will appear inside the band gap, also known as donor or acceptor levels. Valence electrons could transition to these well-defined impurity levels with a corresponding energy transferred from the hot electrons scattering. The subsequent electron-hole recombination will create photons with a sharp, well-defined energy which can be observed as a narrow peak in a CL spectrum. [67]. Figure 3.10 shows a schematic of the possible cathodoluminescence excitation and emission processes.



Similarly, when an impurity is present with incomplete inner shells, such as a rare-earth or transition metal ion, the excitation and radiative deexcitation of the inner shell transition result in cathodoluminescent emission [66].

To investigate the cathodoluminescence of the samples in this work, CL measurements were carried out using a Horiba HCL-I312 spectrometer equipped with a parabolic mirror attached to a FEI Quanta 650 SEM. The electron beam was accelerated with 5kV for ITO:Tb to reduce the substrate signal. In the case of AZO:Tb films, 10kV was used in order to increase the Tb-related intensity.

## 3.5 Electrical characterization

### 3.5.1 Van der Pauw technique

The Van der Pauw technique is widely employed to estimate the resistivity of a semiconducting thin film samples with arbitrary shape. The only parameter needed is the film thickness, although there are a few additional conditions that the sample should comply: it must be homogeneous, isotropic, and flat with no holes within. The four contacts should be point-like and positioned on the periphery of the sample [90, 91]. The resistivity of the sample is measured by driving a current through two adjacent contacts and measuring the voltage between the other two. A typical Van der Pauw arrangement schematic can be seen in Figure 3.11(a) for a square-shaped sample. By introducing a current through contacts 1 and 2 and measuring the voltage between 3 and 4, the resistance  $R_a = R_{12,43} = V_{43}/I_{12}$ , can be calculated. Analogously,  $R_b = R_{23,14} = V_{14}/I_{23}$  can be determined. Van der Pauw showed that the resistivity  $\rho$  can be estimated from these two resistance measurements

$$\rho = \frac{\pi d}{\ln 2} \left[ \frac{R_a + R_b}{2} \right] f \quad (3.3)$$

where  $d$  is the sample thickness and  $f$  has to be obtained by solving the following transcendental equation

$$\frac{R_a - R_b}{R_a + R_b} = \frac{f}{\ln 2} \operatorname{arccosh} \left\{ \frac{1}{2} \exp \frac{\ln 2}{f} \right\} \quad (3.4)$$

For consistency checks on measurement repeatability and accuracy, ohmic contact quality and sample uniformity, the measurement configuration can be permuted for each pair of



contacts and the polarity of the current be reversed for each configuration [92], resulting in the following averaged resistances

$$\begin{aligned} R_a &= \left( \frac{R_{12,43} + R_{21,34} + R_{34,21} + R_{43,12}}{4} \right) \\ R_b &= \left( \frac{R_{23,14} + R_{32,41} + R_{41,32} + R_{14,23}}{4} \right) \end{aligned} \quad (3.5)$$

This will give a more accurate value for the resistivity in Eq. (3.3).

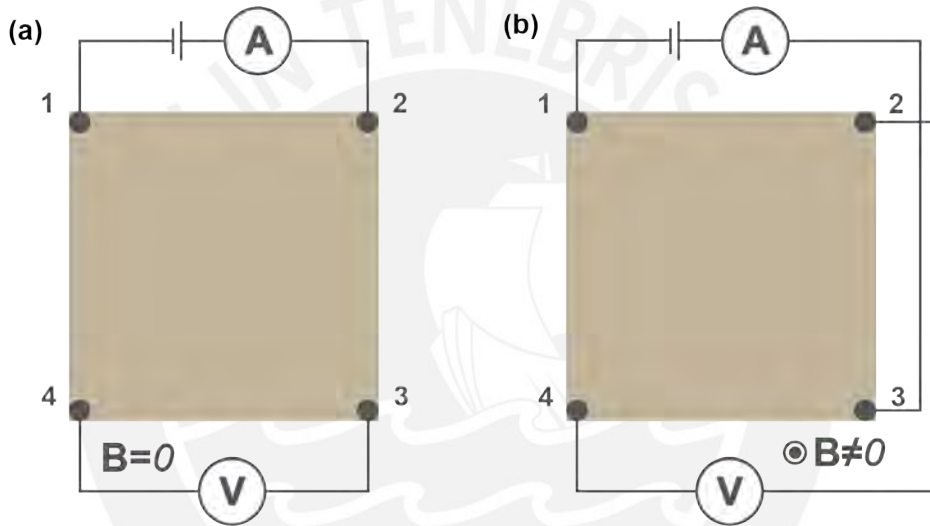


Fig. 3.11 Schematic of the Van der Pauw configuration for (a) resistivity and (b) Hall measurements.

### 3.5.2 Hall effect measurements

For Hall effect measurements, the Van der Pauw configuration is as depicted in Figure 3.11(b). The measurement is carried out with a magnetic field perpendicular to the sample, while the current is delivered at opposite contacts, e.g. 1 and 3, and the Hall voltage is measured at the other two opposite contacts, 2 and 4. Ideally, the Hall voltage contacts should be placed on a equipotential line, but in practice this may not be the case. As a consequence, a misalignment offset voltage appears when  $B = 0$ . This offset is usually corrected by repeating the measurement with a reversed magnetic field direction. An additional constant offset voltage occurs due to thermoelectric effects in the contacts. This constant offset can be eliminated measuring the Hall voltage with a reversed current polarity [93]. The mean Hall voltage between contacts 2 and 4 would be

$$\bar{V}_{H24} = \left[ \frac{V_{H24}(B_+, i_+) + V_{H24}(B_+, i_-) + V_{H24}(B_-, i_+) + V_{H24}(B_-, i_-)}{4} \right] \quad (3.6)$$

where  $B_{+,-}$  and  $i_{+,-}$  refer to different polarities for the magnetic induction and the applied current [92]. Analogously, the mean Hall voltage  $\bar{V}_{H13}$  can be obtained between contacts 1 and 3 by applying a current through 2 and 4. Thus, the Hall coefficient is

$$R_H = \frac{d}{iB} \left( \frac{\bar{V}_{H24} + \bar{V}_{H13}}{2} \right) \quad (3.7)$$

In general, the Hall coefficient can be defined by

$$R_H = \pm \frac{r}{qn} \equiv \pm r\rho\mu \quad (3.8)$$

where  $r$  is the Hall scattering factor,  $R_H > 0$  for holes and  $R_H < 0$  for electrons. It can be seen that the majority carrier concentration  $n$  and mobility  $\mu$  can be obtained from Eq. (3.7) and Eq. (3.8), while the sample resistivity  $\rho$  can be obtained as described in the previous section. The Hall scattering factor  $r$  takes into account the energy-dependence of the scattering rate and typically takes values  $r \approx -1/2 - 2$  [92], depending on the dominant scattering mechanism and the shape of the energetic bands of the semiconductor. Typically, the so-called Hall mobility is defined by choosing  $r = 1$ . Accordingly,  $n$  would be defined as the Hall carrier density [93].

Resistivity measurements of ITO and ITO:Tb samples on (10 mm × 10 mm) square fused silica wafers were carried out in a homemade 4-probe setup in the van der Pauw configuration. The setup consisted of a source measure unit Keithley 2450 which acted as current source, voltmeter and ammeter, a multimeter Keithley 2701 together with a 7709 matrix module for measurement permutation and a probe station. Four gold coated spring tips were used to make electrical contact with the films. Uniform pressure on all four contacts was assessed by means of current-voltage measurements, in which all samples showed an ohmic behaviour.

Resistivity and Hall effect measurements of ZnO and AZO samples were made with a Lakeshore Model 8404 AC/DC Hall Effect measurement system in the Laboratory for transport measurements, affiliated to the Department of Dynamics and Transport in Quantum Materials at HZB. The system was controlled with a LabView script that allowed measurements varying both the current into the sample and the intensity of the magnetic field. In order to estimate the  $R_H$ , measured values of  $V_H$  were plotted against  $i \cdot B$ , according to

Equation (3.7). Then,  $R_H$  was obtained from the slope of a linear fit on the data, considering the thickness  $d$  estimated via transmittance measurements. Both  $n_H$  and  $\mu_H$  were calculated following Equation (3.8) with the previously determined value for  $\rho$ . Errors were estimated by error propagation of the fitted uncertainties.



## Chapter 4

# Impact of Tb incorporation on the optical, electrical and light emission properties of ITO

This chapter presents the effects of introducing Tb ions in ITO on its optical and electrical properties. These are also affected after post-deposition annealing treatments are carried out in order to optically activate the luminescence of Tb ions. Luminescence was studied by comparing the light emission intensity at each annealing temperature for different Tb concentrations. The electrical resistivity was compared to that of the pure ITO by analyzing the free carrier absorption spectral region and by four-point probe measurements. To investigate the excitation mechanism of luminescent Tb ions, the Tb-related emission intensity was assessed against the sample temperature. The results suggest a thermal quenching process that can be evaluated by means of an isoelectronic trap model, presuming an indirect excitation mechanism by the formation of excitons bound to Tb<sup>3+</sup> clusters.

### 4.1 Elemental composition and structural characteristics

Knowledge of the elemental composition of each sample both before and after annealing treatments provides insight about the impact of these treatments on the properties of the material. In general, it is known that rare-earths have great affinity to oxidize, thus it is expected that for a higher RE concentration, the oxygen concentration should also increase, even during the deposition. For the samples investigated in this work, a mass spectrometer detected traces of oxygen gas and water vapour that could act as oxygen sources during the deposition.

Figure 4.1 shows the elemental concentration (In, Sn, O) vs Tb concentration of the as-grown (AG) samples and after annealing treatments for an undoped ITO film and a 0.86 at.% Tb doped ITO film. The increase of oxygen in samples with increasing Tb concentration can be noticed in Figure 4.1 a), where concentrations for all elements were estimated as described in Section 3.2.2. Additionally, both In and Sn concentrations decrease when increasing Tb. This might be due to a possible substitutional introduction of Tb into the ITO lattice by occupying In b- or d-sites, which would also be occupied by substitutional Sn ions. In the case of pure ITO (0 at.% Tb) there is oxygen deficiency in the sample. Oxygen deficient regions near the surface have also been observed when depositing sputtered ITO on low temperature substrates [94–96]. Figure 4.1 b) shows some variations in the atomic concentrations when increasing annealing temperature in the case of pure ITO (open symbols). Particularly, at  $\sim 180^\circ\text{C}$  there is an increase in oxygen concentration that might be due to the air annealing induced oxidation of  $\text{Sn}^{2+}$  into  $\text{Sn}^{4+}$ . For ITO:Tb (filled symbols), the elemental composition does not seem to change noticeably, although there is a slight increase of oxygen when increasing the temperature.

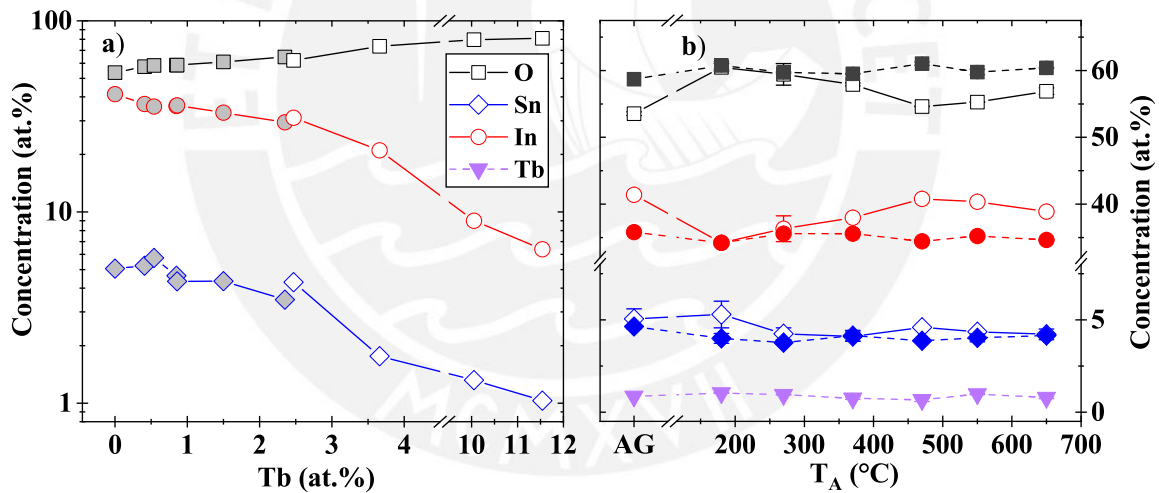


Fig. 4.1 a) Atomic concentration of as grown Tb doped ITO thin films deposited on silicon (open symbols) and fused silica (filled symbols) substrates, as obtained from EDS. b) Atomic concentration of pure ITO (open symbols) and 0.86 at.% Tb doped ITO (solid symbols) films versus annealing temperature.

Figure 4.2 shows that the AG pure ITO sample have a mixed polycrystalline and amorphous state, whilst the sample with 0.86 at.% Tb present an amorphous structure. It should be noted that the amorphous state in both cases might be induced due to the combination of active cooling during deposition and the introduction of Tb ions. After the annealing process in air at  $550^\circ\text{C}$ , both pure and Tb doped samples show a noticeable crystallization. By observing

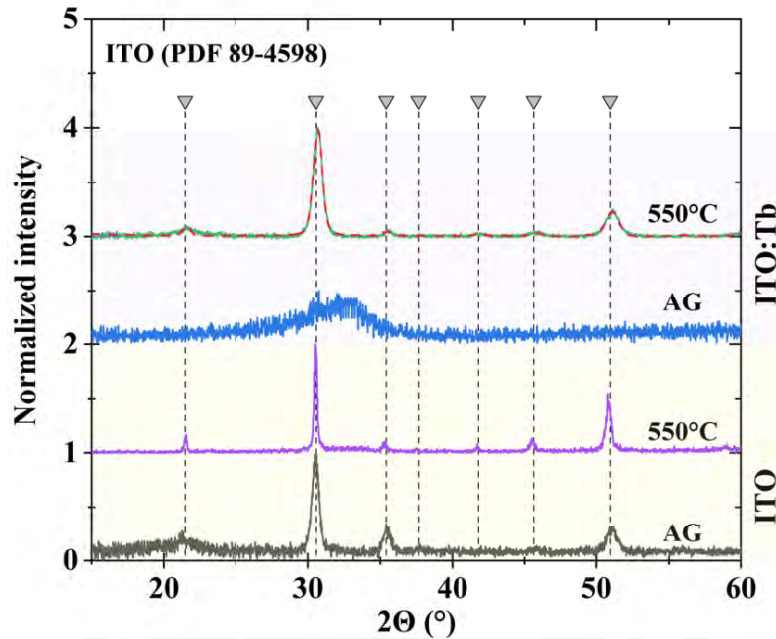


Fig. 4.2 X-ray diffraction patterns of the ITO and 0.86 at.% Tb doped ITO samples before and after annealing at 550 °C. PDF reference peak positions of ITO are also plotted. The corresponding crystallite size and microstrain estimated with Rietveld refinement are summarized in Table 4.1. Diffractograms were normalized and shifted for better visibility.

the diffraction peak widths of the annealed samples, it can be inferred that the crystallite size of the Tb doped samples is smaller than that of pure ITO.

The crystallite sizes and microstrains of these samples were estimated by Rietveld refinement of the diffractograms shown in Figure 4.2 and the results can be compared in Table 4.1. The amorphous phase of the ITO:Tb sample for the AG state is expected due to a bigger ionic radius of  $Tb^{3+}$  ions in comparison to that of  $In^{3+}$ . Nonetheless, it can be noticed that the diffraction peaks for the 550 °C sample correspond to the PDF lines and no peaks associated to terbium sub-oxide ( $TbO_x$ ) crystallites was found [97–99]. This further supports the idea that Tb ions are substitutional in ITO.

Thus far, the introduction of Tb in a quantity up to 11.5 at.% into ITO induces an amorphous structure during preparation. Furthermore, as Tb concentration increases, the atomic composition of O increases, whilst that of Sn and In decreases. As both Tb and O concentrations increases,  $TbO_x$  might also increase, and as no related peaks were measured, their amorphous phase could still be present. When post-deposition air annealing treatments are carried out, the crystallinity of the material vastly improves and the elemental concentration does not significantly change.

Table 4.1 Crystallite size and microstrain of pure ITO and 0.86 at.% Tb doped ITO layers, before and after annealing treatment at 550 °C. The values were obtained from a Rietveld analysis of the diffractograms depicted in Figure 4.2. Retrieved lattice parameters are 10.093(4) Å and 10.092(3) Å for the AG and 550 °C annealed ITO, respectively, and 10.095(2) Å for the Tb doped ITO sample annealed at 550 °C.

Sample	Crystal size (nm)		Lattice strain (%)	
	AG	550 °C	AG	550 °C
ITO	36.5(55)	59.1(77)	1.41(6)	0.54(3)
ITO:Tb <sup>3+</sup>	-	21.0(9)	-	1.82(3)

## 4.2 Influence on the optical properties

One of the most important optical characteristics of ITO is its transparency in the visible spectral region due its wide band gap from 3.5 eV to 4.3 eV [100]. Furthermore, its degenerate nature due to the very high doping bestows an important IR photon absorption by the free carriers.

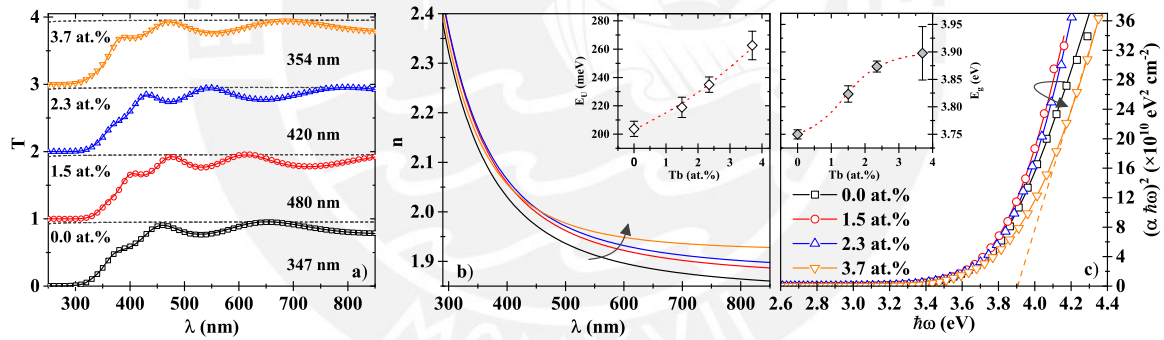


Fig. 4.3 Optical transmittance of as-grown Tb doped ITO thin films grown on fused silica substrates for different Tb concentrations alongside the substrate transmittance (dashed gray lines). Solid lines are fits using a modified Swanepoel method [82]. The corresponding thickness and Tb concentration are denoted in nm and at.%, respectively (a). Refractive index (b) and absorption coefficient (c) calculated from the optical transmittance measurements. The absorption coefficient is plotted in the  $(\alpha\hbar\omega)^2$  scale. Solid curves are fits using a band-fluctuations model for direct semiconductors (Equation (2.2)). The dashed line highlights the linear behaviour of the fundamental absorption in this scale, which is the behaviour expected from theory for a direct semiconductor [54]. Only 60 data points out of 600 are plotted to avoid visual clutter. Dotted lines in inset graphs are a guide to the eye.

Figure 4.3 depicts the optical transmittance and the corresponding retrieved refractive index  $n(\lambda)$  versus photon wavelength  $\lambda$ , and absorption coefficient  $\alpha(\hbar\omega)$  versus photon energy

$\hbar\omega$ , of the as grown ITO:Tb<sup>3+</sup> films for different Tb concentrations, covering the fundamental absorption and transparent spectral regions. All samples exhibited a high optical transmittance in the visible spectrum, independent of the Tb content or annealing temperature. A systematic increase of  $n$  with increasing Tb concentration is observed, in agreement with the effect of oxygen in the refractive index and material densification [101], whereas the variation of the fundamental absorption is tracked by changes in the optical band gap ( $E_g$ ) and Urbach energy ( $E_U$ ), depicted in the inset graphs of Figure 4.3. The latter parameters are determined by fitting the absorption coefficient with a fundamental absorption model for direct semiconductors. The band-fluctuations model for direct materials described by Equation (2.2) was used. Table 4.2 summarizes the Urbach energies and band gaps calculated by fitting Eq. (2.2) to the absorption coefficient. Additionally, the  $(\alpha\hbar\omega)^2$ -gap for direct semiconductors is also listed [54].

Table 4.2 Optical band gap  $E_g$  retrieved with Eq. (2.2), fundamental  $(\alpha\hbar\omega)^2$ -gap and Urbach energy  $E_U$  of ITO with different Tb concentrations.

Tb (at.%)	$E_g$ (eV)	$(\alpha\hbar\omega)^2$ (eV)	$E_U$ (meV)
0	3.75(8)	3.73(3)	203.7(53)
1.5	3.82(14)	3.80(9)	218.8(71)
2.3	3.87(10)	3.85(7)	234.9(53)
3.7	3.89(48)	3.84(4)	262.5(100)

Here, the increment of  $E_g$  and  $E_U$  observed with increasing Tb concentration is most probably associated to the induced lattice distortion by the presence of Tb ions in the ITO host, the formation of charged defects, and possible presence of suboxides species, even in form of nanoclusters which are not measurable with XRD. The diffractogram of the 550 °C annealed Tb doped sample in Figure 4.2 shows that the preferred growth direction is similar to that of the 550 °C annealed undoped one. No peaks related to terbium oxide [97–99] were found in the diffractograms, which could suggest that Tb ions are being incorporated into the ITO lattice, occupying In<sup>3+</sup> or that they are being incorporated in the form of TbO<sub>x</sub> in an amorphous state. Furthermore, it is known that RE clustering can occur when introducing REs in a host [102, 103], and attempts to experimentally study them have been made in the past [104–106]. In particular, for the case of 1.5 at.% Tb doped SiO<sub>2</sub> [106], Tb clusters tend to form at temperatures equal or higher than 1000 °C with a size around 15 nm. At this point, it is not clear whether these clusters are composed by Tb only or by a combination of Tb oxides. In this case, clustering has not been observed. However, the presence of Tb or Tb oxides clusters within the ITO matrix cannot be discarded. Besides this, Tb ions disrupt the



lattice, thus inducing strain, inhibiting the formation of larger grains during deposition and inducing the formation of oxygen vacancies, all of which lead to a larger Urbach energy. Since Tb addition promotes the formation of charged vacancies when disrupting the lattice [84, 107, 108], an optical band gap shift attributed to the Burstein-Moss effect could be expected. Nevertheless, the formation of Tb suboxides could also play a role in the band gap widening. XRD patterns depicted in Figure 4.2 and lattice strain shown in Table 4.1 confirm the Tb-induced lattice distortion. A similar distortion has also been reported for Cu doped non-crystalline SnO<sub>2</sub> [109], and Nd, Eu and Tb doped In<sub>2</sub>O<sub>3</sub> sol gel films [26].

Both Tb doped and undoped ITO layers exhibited an increase in the infrared absorption as well as an increase of  $E_g$  and  $E_U$  with increasing annealing temperature. Both features are related to a annealing-induced increase in the charge carrier density, see Figures 4.4, 4.5 and 4.6. It has been shown that thermal treatments up to 350 °C increase the electrical conductivity of ITO layers when performed either in inert or reactive atmospheres [42, 110–112]. Nevertheless, for temperatures above 350 °C, electrical conductivity drops depending on the annealing atmosphere used [112]. The reason behind this behaviour is a competition between the thermally-induced activation/deactivation of charged defects along with a variation in the electronic mobility, affecting the electrical conductivity. Typically, for annealing temperatures below 350 °C, Sn ions change their oxidation state from Sn<sup>2+</sup> to Sn<sup>4+</sup>, thus acting as donors when occupying In<sup>3+</sup> sites [113, 112]. On the other hand, annealing treatments in an air atmosphere induce oxygen diffusion into the ITO matrix, therefore reducing the amount of charged oxygen vacancies. This diffusion usually increases the oxygen concentration near the surface of the ITO layer [42]. However, the extent of this diffusion will depend on the available sites or vacancies for oxygen to bond. That is, for nearly saturated samples, oxygen diffusion from the atmosphere will require more energy than in non-saturated ones to diffuse into. Here, EDX analysis depicted in Figure 4.1 showed no major variation of the oxygen content in Tb doped ITO upon annealing. Whilst, for undoped ITO, oxygen reaches the saturation value after the first annealing treatment at 180 °C, from 53.5 at.% to 60.5 at.%, in agreement with previous reports on samples grown in a similar fashion [42].

In order to assess and discern the impact of annealing treatments on the charge carrier density and mobility, the complex refractive index  $\tilde{n}$  is described by a combination of Tauc-Lorentz and Drude-Lorentz models depicted in Eq. 4.1, and fit to the optical transmittance of ITO and ITO:Tb for each annealing temperature.

$$\begin{aligned}\tilde{n}^2 = \varepsilon_1 + i\varepsilon_2 = \varepsilon_1(\infty) &- \frac{\omega_p^2}{v^2 + i\omega_\tau v} \\ &+ \sum_l \frac{\Omega_{p,l}}{\Omega_{0,l}^2 - v^2 - i\Omega_{\tau,l}v} \\ &+ \sum_l^{\text{TL}} \tilde{\varepsilon}_l\end{aligned}\quad (4.1)$$

with

$$\text{Im}(\text{TL}\tilde{\varepsilon}_l) = \frac{A_l E_{0,l} C_l (E - E_{g,l})^2}{(E^2 - E_{0,l}^2)^2 + C_l^2 E^2} \frac{1}{E} \Theta(E - E_{g,l})$$

Here,  $\varepsilon_1$  and  $\varepsilon_2$  are the real and imaginary part of the complex dielectric function  $\tilde{\varepsilon}$ , respectively.  $v$  and  $E$  are the photon wavenumber and photon energy, respectively.  $\tilde{n}$  is the complex refractive index.  $\text{TL}\tilde{\varepsilon}_l$  is the Tauc-Lorentz dielectric function contribution, from which the real part is obtained by a Kramers-Kronig transformation [43].  $\Theta$  is the Heavyside function.

The fitting parameters in this expression are the Tauc-Lorentz oscillator strength  $A_l$ , peak central energy  $E_{0,l}$ , broadening parameter  $C_l$ , Lorentz oscillator strength  $\Omega_{p,l}$ , frequency center  $\Omega_{0,l}$  and damping  $\Omega_{\tau,l}$ , and Drude plasma frequency  $\omega_p$  and collision frequency  $\omega_\tau$ . The last two being related to the charge carrier density  $N$  and mobility  $\mu$  by

$$\omega_p = \sqrt{\frac{Ne^2}{\varepsilon_0 m_e^*}}\quad (4.2)$$

and

$$\omega_\tau = \frac{e}{\mu m_e^*},\quad (4.3)$$

with  $\varepsilon_0$ ,  $e$  and  $m_e^*$  the vacuum permittivity, elemental charge and electron effective mass, respectively.

Sample layers had to be modelled as a two-film stack with the same Tauc-Lorentz and Lorentz oscillators parameters, but distinct Drude parameters. This is typically attributed to the growth-induced microstructure sputtered ITO thin films exhibit and the low penetration depth in the high absorption spectral region where Tauc-Lorentz has the most influence [83–

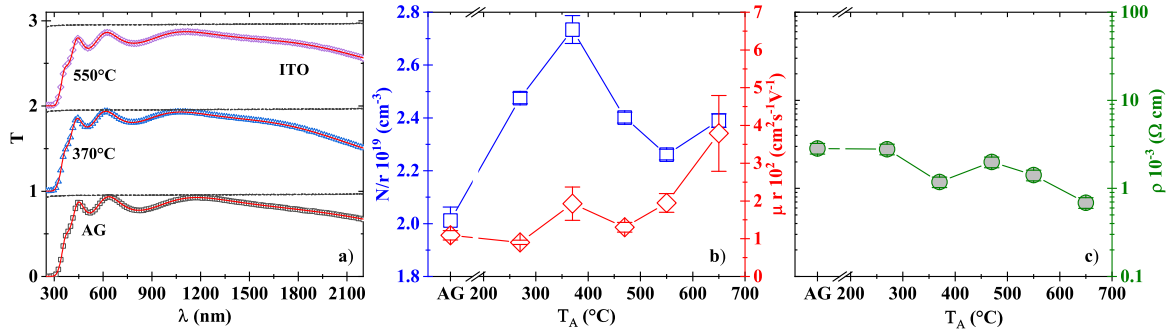


Fig. 4.4 Optical transmittance (a), charge carrier and mobility (b) and electrical resistivity (c) of ITO thin films versus annealing temperature, as determined from the Drude model.  $r$  denotes the ratio between the electron effective mass and the electron rest mass,  $r = \frac{m_e^*}{m_e}$ .

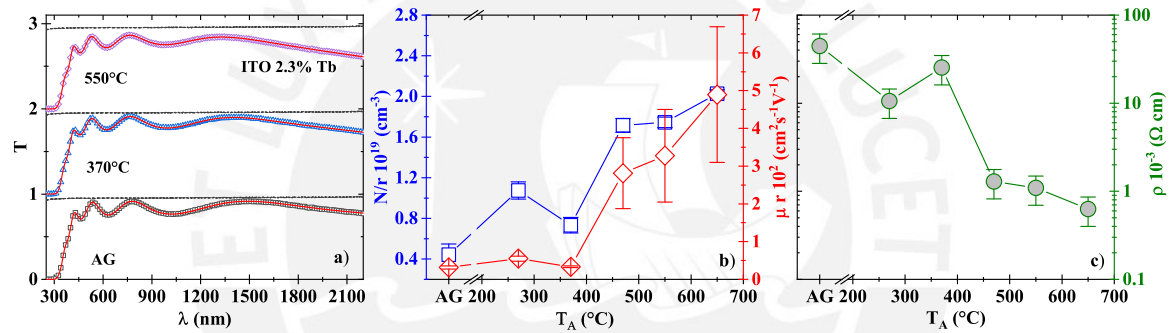


Fig. 4.5 Optical transmittance (a), charge carrier and mobility (b) and electrical resistivity (c) of 2.3 at.% Tb doped ITO thin films versus annealing temperature, as determined from the Drude model.  $r$  denotes the ratio between the electron effective mass and the electron rest mass,  $r = \frac{m_e^*}{m_e}$ .

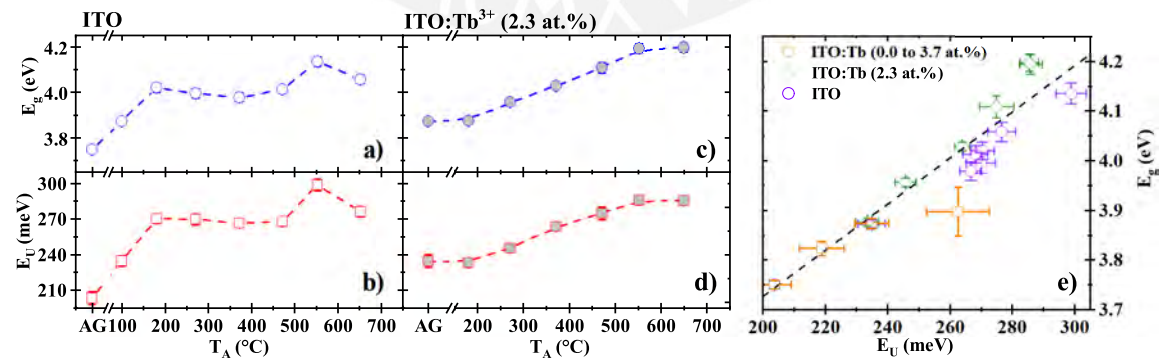


Fig. 4.6 Optical band gap and Urbach energy versus annealing temperature for the undoped (a)(b) and Tb doped (c)(d) ITO layers. Optical band gap versus Urbach energy for different annealing treatments and Tb concentrations (e). The dashed line is a guide to the eye.

88, 114]. The first layer, or bottom layer, exhibits poor electrical properties, whereas the top layer is more conductive. According to Lee and Ok Park [86], the initial region within the first  $\sim 80$  nm is more resistive due to disordered growth. As the film grows thicker, crystallinity increases inducing a resistivity reduction by the increase of the carrier density. Both  $\text{Sn}^{4+}$  ions and oxygen vacancies have more probability to be located at thermodynamically favorable sites in a well-ordered crystallized structure.

In most cases here, the optical transmittance fit is achieved by three Tauc-Lorentz oscillators and one Lorentz oscillator. Figure 4.4 and Figure 4.5 depict the infrared analysis on the optical transmittance of ITO and 2.3 at.% Tb doped ITO films for different annealing treatments, respectively.  $N$  and  $\mu$  are calculated from  $\omega_p$  and  $\omega_\tau$  in terms of the electron effective mass  $m_e^*$ . These are shown for the top ITO layer in the mentioned figures. In these systems,  $m_e^*$  is a fraction  $r$  of the rest mass of an electron  $m_e^* = rm_e$ , which is typically around  $r \sim 0.35$  [115]. Two features are noted in these figures. First, Tb doped ITO has a higher resistivity than the undoped ITO films. The charge carrier density of Tb doped ITO is significantly lower than undoped ITO. Tb ions might be replacing Sn and/or In ions, inhibiting the formation of  $\text{Sn}^{4+}$  and thus limiting the charge carrier density. Additionally, for annealing temperatures below  $400^\circ\text{C}$ , the electron mobility is also smaller due to the induced lattice disorder. Second, the charge carrier density of the undoped ITO sample exhibits a maximum value after  $370^\circ\text{C}$  annealing and drops for higher annealing temperatures. This effect is in agreement with the formation of  $\text{Sn}^{4+}$  for lower annealing temperatures. The observed drop of  $N$  for higher temperatures would be associated to oxygen diffusion into the film occupying vacancies and the formation of Sn-O complexes deactivating donor Sn ions [116]. This behaviour is typically accompanied with an increase in  $\mu$ , also observed Figure 4.4 and Figure 4.5 [117, 118].

Finally, the effect of thermally-induced and Tb-impurity-induced structure variations on the fundamental absorption are traced by  $E_U$  and  $E_g$ . These are plotted in Figure 4.6, for different annealing treatments and Tb concentrations. In this sense,  $E_U$  is used as an indirect measure of the lattice distortion. It can be noticed that larger lattice distortions, either induced by the presence of Tb ions or by thermal treatments in air, are correlated to a widening of the optical band gap. This could be attributed to the increase of oxygen vacancies when introducing Tb into the lattice. This would increase the charge carrier concentration inducing a blue-shift of the optical band gap. On the other hand, the formation of Tb suboxides, together with the increase of oxygen vacancies, would enhance the disorder reflected in the growth of  $E_U$ .

### 4.3 Annealing induced luminescence activation

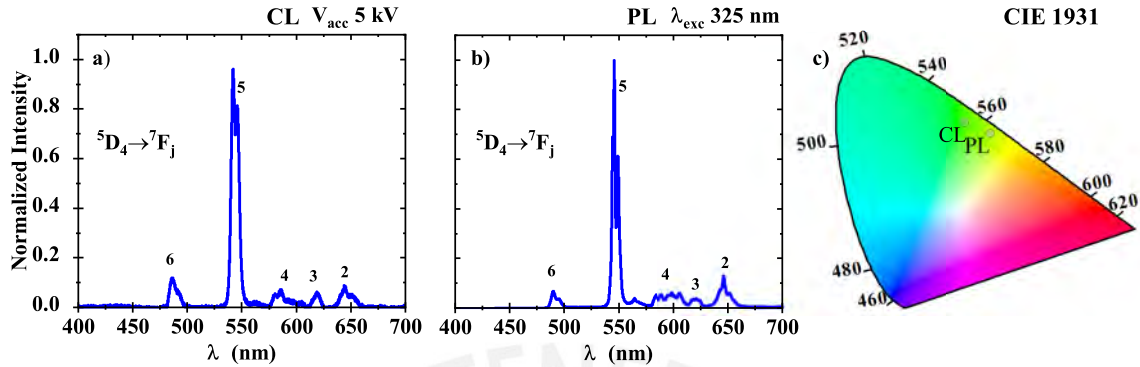


Fig. 4.7 Room-temperature cathodoluminescence (a) and photoluminescence (b) spectra of a 2.3 at.% Tb doped ITO thin film after annealing at 550 °C in air for three hours. The PL excitation wavelength was 325nm. The corresponding coordinates in the CIE1931 color space are also depicted (c).

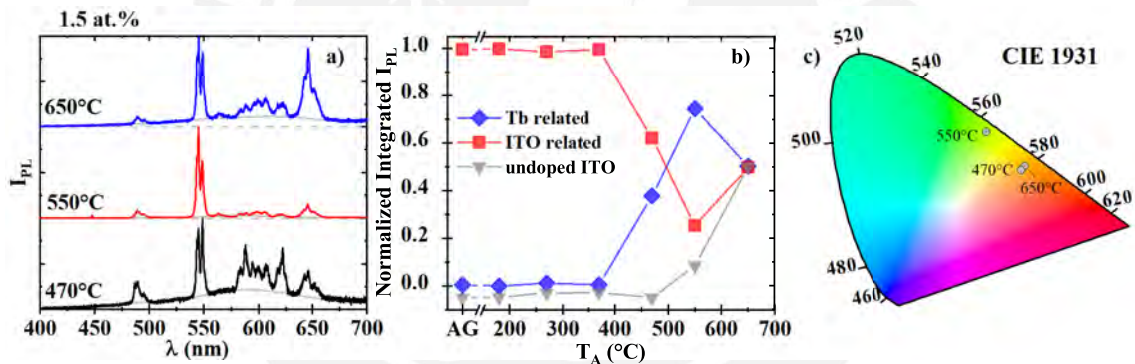


Fig. 4.8 Room-temperature photoluminescence spectra of 1.5 at.% Tb doped ITO after three distinct annealing temperatures (a). Normalized integrated photoluminescence intensity for both the Tb-related and host-related emission. Additionally the light emission intensity evolution of an undoped ITO sample is included (b). The latter is shifted -0.5 for viewing reasons only. The PL excitation wavelength was 325nm. CIE1931 color space denoting the color shift of the Tb doped ITO spectra after each annealing treatment (c).

It is well established that not all the Tb ions embedded in a host are optically active for emission and that these can be activated by post-deposition thermal treatments [20–22, 28]. The underlying mechanisms behind the thermally-induced activation and light emission enhancement are typically associated to: (i) the coordination of Tb ions with neighboring atoms in a non-centrosymmetric crystal field state, (ii) the thermally-induced promotion of energy transfer paths from the host to the REs after excitation [21, 22, 27], (iii) and the inhibition of back transfer energy processes. These establish a competition between the

recombination in RE color centers and host-related radiative and non-radiative recombination centers [21, 119].

Here, the highest Tb-related light emission intensity is achieved after annealing at 550 °C. Figure 4.7 depicts the CL and PL spectra of 2.3 at.% Tb doped ITO under excitation by electrons at a 5 keV acceleration voltage and 325 nm light excitation, respectively. Characteristic Tb-related electronic transitions are identified. Additionally, the Commission International del'Eclairage (CIE1931) colorspace coordinates are also depicted in this figure for comparison purposes to track color differences.

Samples doped with 1.5 at.% and 2.3 at.% Tb are the ones exhibiting the highest emission intensity. In order to try to avoid the impact of the concentration quenching effect, the luminescence-activated sample used for further analysis is the one doped with 1.5 at.% Tb. When increasing Tb concentration together with the number of activated ions, the probability for luminescence quenching can increase (see Fig. 5.2.12. in Guerra [120]). Figure 4.8 depicts the variation of the PL light emission spectra with annealing temperature, where a 325 nm laser was used. Almost no emission associated to Tb ions was registered for annealing temperatures below 470 °C. For these annealing temperatures, a strong host related background dominates the emission. After 550 °C annealing, the Tb emission reaches a maximum, with the  $^5D_4 \rightarrow ^7F_5$  electronic transition ( $\sim 545$  nm), the most probable one. After 650 °C, host-related emission increases again. This is in agreement with an increased host emission observed in the undoped ITO sample treated at the same annealing conditions, thus suggesting a recombination competition between optically active Tb ions and host-related recombination centers.

Notably, after 650 °C annealing, the  $^5D_4 \rightarrow ^7F_2$  electronic transition (peak wavelength  $\sim 650$  nm) emission intensity is increased until it is almost as high as the  $^5D_4 \rightarrow ^7F_5$  ( $\sim 545$  nm), shifting the apparent emission color to orange. Such unconventional variation of the 4f-shell electronic transition probabilities suggests a modification of the crystal field surrounding Tb ions, probably due to the presence of Tb ions in distinct crystalline sites with a non-centrosymmetric crystal field. In the present case, a crystallization after annealing treatments is observed, thus a variation of the crystal field could be expected. Tb ions would replace In and/or Sn ions, see Figure 4.1, thus distorting the lattice and occupying b and/or d sites in the ITO bixbyite crystalline structure. This might be the source behind the observed unconventional emission after the 650 °C annealing treatment, depicted in Fig. 4.8.

## 4.4 Concentration quenching effect

The impact of the Tb concentration on the Tb-related light emission intensity for the ITO host is depicted in Figure 4.9. It shows slight variations in the relative intensities between the spectra as the Tb concentration increases. These variations typically occur when the crystal field surrounding the  $Tb^{3+}$  ions changes. The concentration quenching effect can also be observed, as the Tb-related light emission is quenched with the RE concentration increase above a critical value. This is a consequence of the enhanced energy transfer probability between Tb ions due to their proximity. This enhancement increases the probability of back-transfer processes in which the recombination takes place in a localized state of the host [121]. In this sense, whilst the Tb-related emission is quenched by the concentration quenching effect, host-related emission is enhanced.

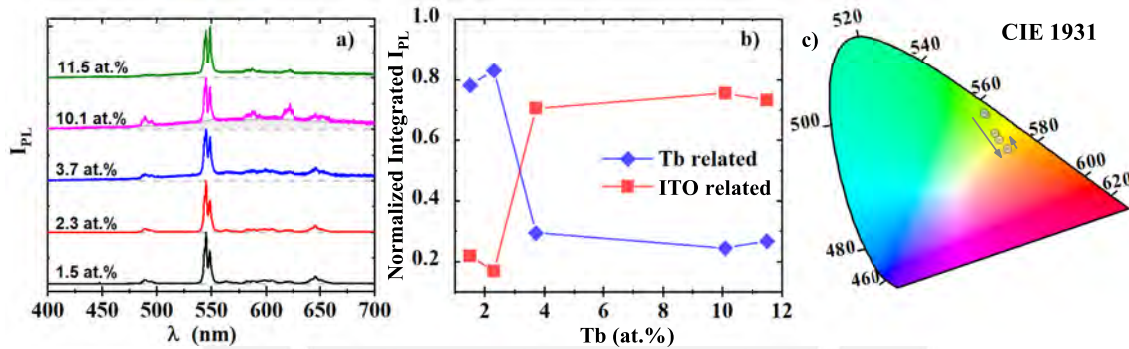


Fig. 4.9 Room-temperature photoluminescence spectra of Tb doped ITO for distinct Tb concentrations. Note the increase in the background emission associated to host-related radiative recombination of ITO (a). Normalized integrated photoluminescence intensity for both the Tb-related and host-related emission (b). The PL excitation wavelength for the measurements was 325nm. CIE1931 color space denoting the coordinates of the spectra for each Tb concentration (c).

In particular the ITO host has a peak around 600 nm with a broad emission at room temperature. This was confirmed by measuring the PL spectrum of an undoped ITO sample. Naturally, the presence of the host emission in the spectra will have an impact in the visible color. The latter is depicted in CIE1931 colorspace in which a shift to a red color is observed when increasing the Tb amount due to the involvement of the host emission.



## 4.5 Thermal quenching and excitation mechanism of Tb<sup>3+</sup> luminescent centers in ITO

Temperature-dependent photoluminescence measurements were performed on the 1.5 at% Tb doped ITO sample annealed at 550 °C, in the temperature range from 83 K (−190 °C) to 533 K (260 °C). Figure 4.10 summarizes the variation of the emission spectra versus the sample temperature. At low temperatures, well defined Stark splitting lines can be observed, in agreement with the crystallization of the material after treatments at 550 °C.

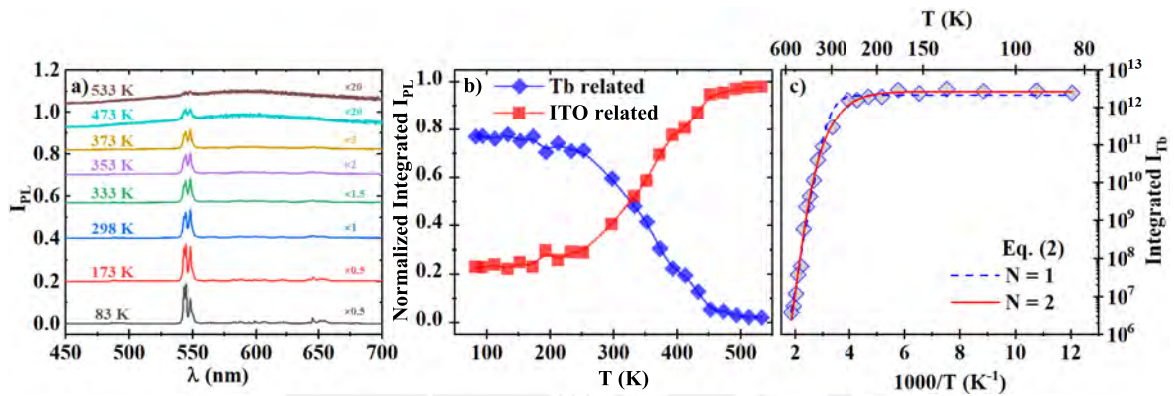


Fig. 4.10 Photoluminescence spectra of 1.5 at.% Tb doped ITO after annealing at 550 °C at distinct sample temperatures and excited with a 325nm laser. Here, the spectra at eight temperatures are depicted with vertical shifts and re-scaling for viewing reasons only (a). Normalized integrated photoluminescence intensity for both the Tb-related and host-related emission (b). Arrhenius plot of the Tb-related integrated photoluminescence (c). The fits correspond to equation (4.4) for one and two activation energies. The best fit is achieved when considering two activation energies.

The overall light emission intensity is quenched with increasing sample temperature, in contrast to the reported behaviour for Tb doped crystalline AlN [18] and amorphous AlN and SiN [22]. In fact, at temperatures above 373 K, the emission corresponds mainly to the host, as can be seen from the integrated normalized emission in Figure 4.10.

An Arrhenius analysis is performed on the Tb-related integrated photoluminescence to assess the activation energies of the underlying thermal quenching process. The integrated emission is modeled by means of a single ( $N = 1$ ) and dual ( $N = 2$ ) quenching channel Arrhenius equation [122, 123],

$$I(T) = \frac{I_0}{1 + \sum_{n=1}^N \exp\left(-\frac{\epsilon_n^b}{k_B} \left(\frac{1}{T} - \frac{1}{T_n}\right)\right)}. \quad (4.4)$$



Table 4.3 Best fitted parameters using equation (4.4) for single (N = 1) and dual (N = 2) thermal quenching processes. The reduced  $\chi^2$  is also shown for comparison purposes. Fits were performed in a logarithmic scale.

	Single	Dual
$I_0$	$1.424E5 \pm 8.5E3$	$1.57E5 \pm 7.6E3$
$T_1$ (K)	$312.6 \pm 4.6$	$290.6 \pm 8.5$
$T_2$ (K)	-	$341.2 \pm 10.6$
$\varepsilon_1^b$ (meV)	$344.5 \pm 14.9$	$152.0 \pm 38.0$
$\varepsilon_2^b$ (meV)	-	$453.9 \pm 39.4$
$\chi^2$	0.036	0.014

Here  $k_B$  is the Boltzmann constant,  $T$  is the sample temperature,  $\varepsilon_n^b$  are the thermal activation energies, which can describe one or more possible thermal quenching channels.  $T_n$  are related to the relative ratios of the competing thermal quenching processes. The best fit parameters are summarized in Table 4.3.

The estimated activation energies could be interpreted as binding energies of excitons that are bound to Tb impurities. Thus, a brief description of isoelectronic traps will be described and related to the energies obtained.

The observed Tb-related emission under 325 nm (3.81 eV) excitation could be the result of an overlap of direct resonant excitation of 4*f*-shell electrons from the <sup>7</sup>F<sub>6</sub> to the <sup>5</sup>D<sub>1</sub> or <sup>5</sup>D<sub>2</sub> energy levels, and host-assisted indirect excitation mechanisms. The former is considerably limited by the 4*f*-shell cross section, whilst the latter can be attributed to distinct energy transfer processes. Indirect excitation mechanisms could be (i) Auger excitation of Tb ions near neutral dangling bonds [29, 22], (ii) dipole mediated resonant energy transfer from electron-hole (*e* – *h*) pairs [27], (iii) excitation by charge transfer from the host or a metal (lanthanoid) ion with a different oxidation state [124–126] and (iv) excitation by energy transfer from the recombination of bound excitons to Tb ions [18].

Auger excitation (i) requires the proximity of Tb ions to neutral dangling bonds. Moreover, this mechanism is phonon assisted since a resonant energy transfer is not required and the excess energy can be taken by phonons. Here, no enhancement of the Tb-related light emission intensity is observed with the sample temperature, in contrast to the reported behaviour for Tb doped AlN and SiN [18, 22], suggesting this is not the most relevant mechanism for Tb doped ITO. On the other hand, dipole-mediated energy transfer (ii) is of long-range interaction. However, it must be resonant, thus limiting the probability of

this mechanism in contrast to the other ones. Additionally, photoluminescence excitation spectra (not shown here) did not exhibit characteristic resonant bands when monitoring the  $^5D_4 \rightarrow ^7F_5$  emission band. Charge transfer (iii) requires a change in oxidation state and is typically accompanied with an additional broad emission band [125, 127], which is not observed here. Therefore, the excitation mechanism is attempted to be modeled by means of (iv) energy transfer from recombination of bound excitons to Tb ions.

It is widely accepted that RE ions induce isovalent or isoelectronic cluster traps by substituting atoms with the same ionization as the atom they replace. [128–131, 18, 132, 133]. There are some features that can be taken into account for this, such as that the ionic radius of Tb<sup>3+</sup> (0.923 Å) is bigger than that of In<sup>3+</sup> (0.81 Å), which it is assumed to be substituting, and that Pauling's electronegativity of Tb<sup>3+</sup> (1.2) is smaller than that of In<sup>3+</sup> (1.78) [134, 135]. Baldereschi [128] derived a simple electronegativity rule relating the pseudopotential depths for the outer *s* and *p* states, both of which are lower for heavier atoms. If the isovalent impurity is heavier than the host atom it replaces, the impurity is less electronegative than the replaced atom. This difference in electronegativity will create a short-range potential surrounding the impurity which is attractive to holes. Furthermore, the difference between the ionic radii of Tb<sup>3+</sup> and In<sup>3+</sup> generates distortion in the ITO lattice. There is an additional potential due to this distortion surrounding the Tb impurity that will increase the attraction of holes [18]. Therefore, the isovalent trap will be positively charged due to hole trapping and will afterwards attract an electron by long-range Coulomb interaction, creating a bound exciton. There would be no charge transfer (*h+*) neither from In<sup>3+</sup> or Sn<sup>4+</sup> lattice sites/interstitials nor from generated *e* – *h* pairs to the Tb<sup>3+</sup> ion to form Tb<sup>4+</sup>, which is known to be a non-luminescent center and could also act as a Tb<sup>3+</sup> luminescence killer [136].

The binding energies of a hole bound to an isovalent cluster trap were calculated using both the spherical potential-well (SPW) and the Koster-Slater (KS) models. Different from the calculation done by Lozykowski [18] for RE doped thin films, both fitted energies were used to calculate the parameters corresponding to each model, assuming the lowest energy for *n* = 1 (singlet) and the largest for *n* = 2 (dimer), *n* being the number of RE ions forming the cluster. Subsequently, these calculated parameters were employed to estimate the corresponding energies for larger clusters, *n* ≥ 3, see Figure 4.11.

In the SPW model, the binding of a hole trapped to a RE-cluster isovalent trap can be described by a three-dimensional spherical potential-well with an effective depth  $-V_0$  and radius  $\rho_1$ . In the case of clusters with *n* > 1, the model assumes the cluster to contribute a potential well with the same depth  $-V_0$  and an effectively enlarged radius,  $^{\text{eff}}\rho_n = n^{1/3}\rho_1$ . The binding energy of a hole bound to a *n*-cluster is given by [137]

$$\varepsilon_n^b = \frac{\hbar^2 \beta_n^2}{2m^* \rho_n^2}, \quad (4.5)$$

with

$$\beta_n = - \left( \frac{2m^* V_0^{eff} \rho_n^2}{\hbar^2} - \beta_n^2 \right)^{1/2} \times \cot \left[ \left( \frac{2m^* V_0^{eff} \rho_n^2}{\hbar^2} - \beta_n^2 \right)^{1/2} \right]$$

and

$$\rho_n^{eff} = n^{1/3} \rho_1.$$

Here  $m^*$  is the average effective mass. Baldereschi [128] suggested that for covalent materials  $m^*$  is  $0.9 m_0$  and for III-V compounds it  $1.2 m_0$ ,  $m_0$  being the free electron mass at rest. Since ITO has a more covalent than ionic bonding structure, it is assumed that  $m^*$  is simply equal to  $m_0$ . The parameters calculated with this model are shown in Table 4.4.

Table 4.4 SPW and KS parameters obtained from Eqs. 4.5 and 4.7 using the activation energies derived from the thermal quenching behaviour of the luminescence.

SPW	$\rho_1$ (nm)	$0.29 \pm 0.02$
	$V_0$ (eV)	$1.67 \pm 0.04$
KS	T (eV)	$5.08 \pm 0.35$
	J (eV)	$1.79 \pm 0.03$

The obtained small radius effectively suggests that there may be a strong localization of the effective impurity potential. Oxygen atoms in the cubic bixbyite structure of ITO have four different bond lengths with respect to the b- or d- sites that the Tb ion would occupy: 2.13 Å, 2.18 Å, 2.19 Å and 2.23 Å [138]. Furthermore, it has been suggested that the Tb-O bond length is 2.35-2.57 Å in polymers [139], mononuclear complexes [140] and simulations [141]. Hence, the calculated effective radius of influence for this short-range impurity potential is relatively close to these Tb-O bond length values.

For the KS model, a one-band one-site tight-binding approximation is employed, assuming a Hubbard density of states [142]. This approximation requires only two parameters, i.e. the

matrix element of the impurity potential  $J$ , and the effective valence band width of the host  $T$ , see Eq. (4.6) for  $n = 1$  and Eq. (4.7) for  $n > 1$ .

$$\varepsilon_1^b = J \left( 1 - \frac{T}{4J} \right)^2 \quad (4.6)$$

$$\varepsilon_n^b = \frac{1}{2} \left[ J - \frac{2n-1}{2n-2} T + \left( J + \frac{T}{2n-2} \right) \times \left( 1 + \frac{n-1}{2} \frac{T}{J} \right)^{1/2} \right] \quad (4.7)$$

The hole binding energies derived from these equations are approximately equal to binding energies of excitons bound to the RE isovalent impurity, with respect to the free exciton energy [142, 129]. Eqs. (4.6) and (4.7) were used to calculate  $J$  and  $T$  values, with the experimental binding energies obtained from the thermal quenching analysis.

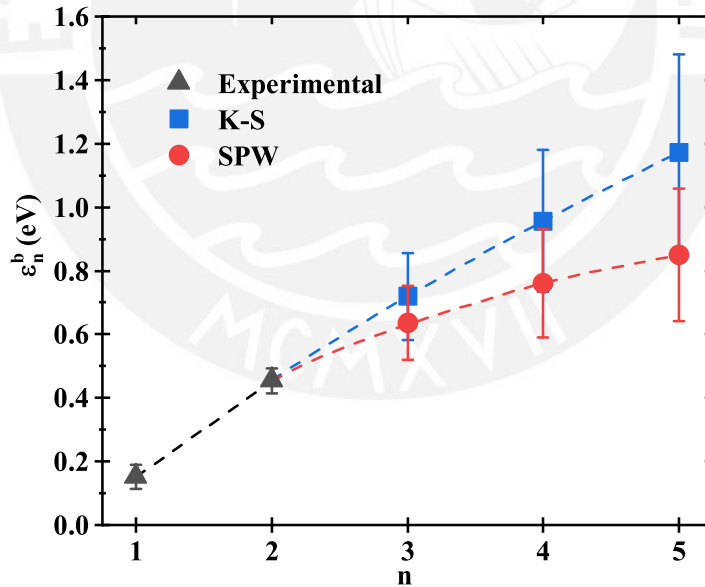


Fig. 4.11 Exciton binding energies calculated by the SPW and KS approaches for different cluster sizes. Experimental values correspond to those determined by the thermal quenching effect. Dashed lines are a guide to the eye.

The uppermost valence band width for ITO is around 6 eV, as estimated by both simulated [143, 138] and experimental [144] methods. Our calculated value for  $T$ , given in Table 4.4, represents a good approximation.

Figure 4.11 depicts the exciton binding energies for distinct cluster sizes obtained from the SPW and KS models by using the previously determined thermal quenching activation energies. This is assuming the latter activation energies are the necessary energy to break bound excitons and/or release trapped holes, and thus inhibit the RE excitation. Still, further research is necessary to confirm if this indeed could be the main excitation mechanism in this and other TCO materials hosting luminescent RE ions.

## 4.6 Effects on the electrical properties

All samples exhibited an ohmic behaviour when measured using four probes in the Van der Pauw geometry. The effect of Tb incorporation and annealing treatments on the electrical resistivity  $\rho$  of ITO is depicted in Figure 4.12. It is important to highlight that, contrary to the resistivity shown in Figs. 4.4 and 4.5, the values shown in Figure 4.12 correspond to the whole ITO system, i.e. the two layers with different Drude parameters. As-grown Tb doped ITO exhibits its lowest  $\rho$  value for Tb concentrations around 0.5 at.%. Layers grown with active cooling and for Tb concentrations below 1.0 at.% have an oxygen concentration below 60 at.%. Thus, it is suggested, that in the as-grown state, a low Tb concentration can enhance the electrical properties of ITO thin films grown with active cooling. At higher Tb concentrations, lattice distortion plays an important role in quenching the electrical conductivity.

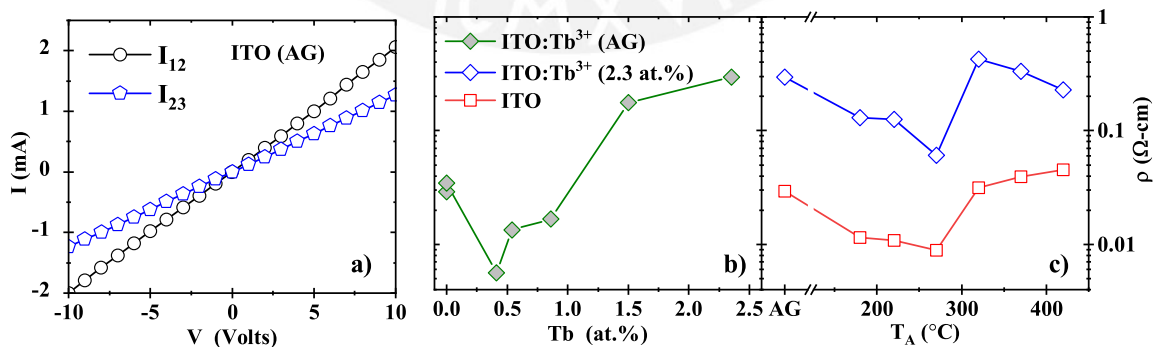


Fig. 4.12 Current-voltage curves of an as grown (AG) ITO sample for two permutations passing the current through the contacts 1 and 2, and then by the contacts 2 and 3 (a). Electrical resistivity versus Tb atomic concentration without thermal treatments (b). Electrical resistivity versus annealing temperature for the undoped and Tb doped cases (c).

The dependence of the electrical resistivity of ITO and 2.3 at.% Tb doped ITO films with the annealing temperature is depicted also in Figure 4.12. As annealing treatments proceed,  $\rho$  decreases till 250 °C. For higher temperatures the resistivity increases again. This behaviour is in agreement with that reported for ITO thin films annealed in air [145, 42, 111, 146]. At first, annealing induces the formation of charged defects, improving the film conductivity. However, after annealing at higher temperatures in air, oxygen diffusion inside the layer may quench the number of charged vacancies [146, 42], and the formation of Sn-O and/or Tb-O complexes prevent the promotion of Sn<sup>4+</sup> [146, 111, 116, 118, 117, 145]. A similar behaviour is observed in the case of Tb doped ITO films grown by sol-gel [30].

## 4.7 Summary

Tb ions have been embedded effectively in ITO thin films by co-sputtering. Samples were grown by actively cooling the substrates during the deposition process in order to limit grain sizes and induce an amorphous phase to subsequently allow the thermally induced RE activation by means of post-deposition annealing treatments. This strategy proved useful since Tb-related light emission was achieved for annealing temperatures above 400 °C. Under these conditions, electrical resistivity measurements showed that Tb doped ITO thin films exhibit a higher resistivity than that of pure ITO for concentrations above 1.0 at.%, whilst a lower resistivity is observed for smaller Tb concentrations. On the other hand, the observed behaviour of the resistivity of Tb doped ITO versus annealing temperature is similar to that of the non-doped ITO film resembling the behaviour reported previously in the literature [146, 111]. The behaviour of the charge carrier density depicted in Figure 4.4 suggests that oxygen diffusion occurs at temperatures higher than 250 °C, whilst ITO crystallization takes place at lower temperatures [42], both processes affecting the electronic properties of the material.

The optical absorption edge is strongly affected by the Tb concentration. This is probably due to the Tb affinity to oxidation, which enhances the formation of Tb-O complexes, and to the induced lattice distortion increasing disorder related localized states. The effect of thermal treatments and Tb concentration in the structure is traced by the Urbach energy and optical band gap. Both increase with annealing temperature and Tb concentration, suggesting, at least for samples with Tb concentrations below 1.0 at.%, an increase in the charge carrier density caused by charged defect states, such as oxygen vacancies, that may be responsible for the observed reduction in the electrical resistivity at this concentration regime and for samples grown with active cooling. As Tb concentration increases, the probability for oxygen to occupy those vacancies would be enhanced, as more oxygen might be introduced.

Furthermore, higher Tb concentration would also lead to growth of smaller grains, thus decreasing charge mobility.

Annealing treatments in Tb doped non-degenerate wide band gap semiconductors usually do not induce an optimal Tb ion activation temperature [147, 29, 21, 148]. In these hosts, predominant energy transfer processes change with annealing treatments at high temperatures due to modifications in their structure, although at these temperatures more ions could be effectively activated by occupying sites. [148]. In contrast to this behaviour, here the light emission intensity versus annealing temperature suggests that there is an optimum annealing temperature for which Tb ions are effectively activated to be excited. This might be related to a competition between the energy transfer to Tb ions and host related luminescent centers. Moreover, after annealing at 650 °C, the  $^5D_4 \rightarrow ^7F_2$  Tb electronic transition is considerably enhanced, shifting the emission color to red. This unexpected enhancement might be attributed to a particular crystal field surrounding Tb ions. A deeper analysis with crystal field calculations is needed in order to get a better idea of the atomic environment surrounding these luminescent centers. For instance, these activated ions may be occupying an In b- or d- site substitutionally, or perhaps are situated in an environment corresponding to a Tb or Tb oxide cluster.

Finally, temperature-dependent photoluminescence measurements on the 1.5 at.% Tb doped ITO showed a continuous decrease of the Tb-related light emission intensity. Two activation energies were determined from the luminescence thermal quenching. By assuming that the main excitation mechanism is due to the recombination energy of excitons bound to RE-ion isovalent traps being transferred to those RE-ions in the trap, the estimated activation energies were used to determine the spherical potential-well and Koster-Slater models parameters. The calculated singlet effective interaction radius ( $\rho_1$ ) is slightly larger with respect to the Tb-O bond length, whilst the effective valence band width ( $T$ ) is in agreement with values reported in the literature [143, 138, 144].

## **Chapter 5**

# **Impact of Tb incorporation on the structural, optical and electrical properties of AZO**

This chapter presents the effects of introducing Tb ions in AZO on its structural, optical and electrical properties. These are also influenced by post-deposition annealing treatments, in particular the luminescence of the material. This property was studied by comparing the light emission intensity at each annealing temperature for different Tb concentrations. To investigate the excitation mechanism of luminescent Tb ions, the Tb-related emission intensity was assessed by varying the sample temperature for selected samples. The results suggest a thermal quenching process that can be evaluated by means of a trap model, also presuming an indirect excitation mechanism by the formation of excitons bound to Tb<sup>3+</sup> clusters.



## 5.1 Effect of post-deposition annealing treatments

### 5.1.1 Elemental composition and structural properties

As in the case of ITO, Tb was introduced by co-sputtering in ZnO and AZO thin films and the deposition process was carried out also by actively cooling the substrates during deposition. The deposition conditions can be seen in Table 3.1. The elemental composition against Tb concentration for the as-grown state samples measured with EDS can be seen in Figure 5.1. Fluctuations in Al and Tb concentrations might be attributed to the deposition conditions where a manually controlled impedance matching system was employed for the Al target and was periodically checked in order to reduce the reflected power to the lowest possible value. Al concentration was to be obtained around the range 2 at.% to 4 at.%. Notwithstanding, an increase of Al can be observed up to 1.7 at.%Tb where it slightly exceeds 4 at.%, after which it decreases for the highest Tb concentration. The Zinc concentration gets reduced when increasing Tb. This could be due to the occupation of the Tb ions in the ZnO lattice by substituting Zn ions. Additionally, O concentration also noticeably increase with Tb. Notice how for pure AZO (0.0 at.%Tb), there is an oxygen deficiency which is expected when growing AZO without additional oxygen during deposition [149]. When Tb is introduced incrementally, it can be observed how both Zn and O concentration shift oppositely. This might be due to the very strong Tb affinity for oxygen [150].

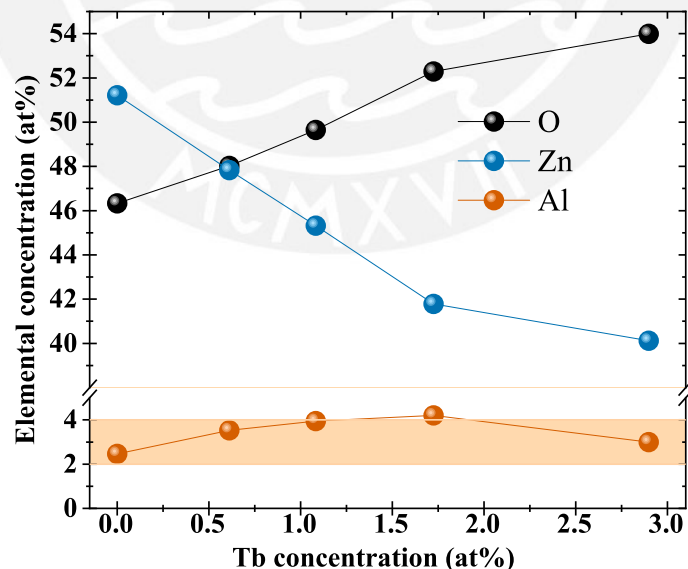


Fig. 5.1 Elemental composition of Al, Zn and O against Tb concentration for the air annealed samples. The shaded region represents the expected values for Al concentration.

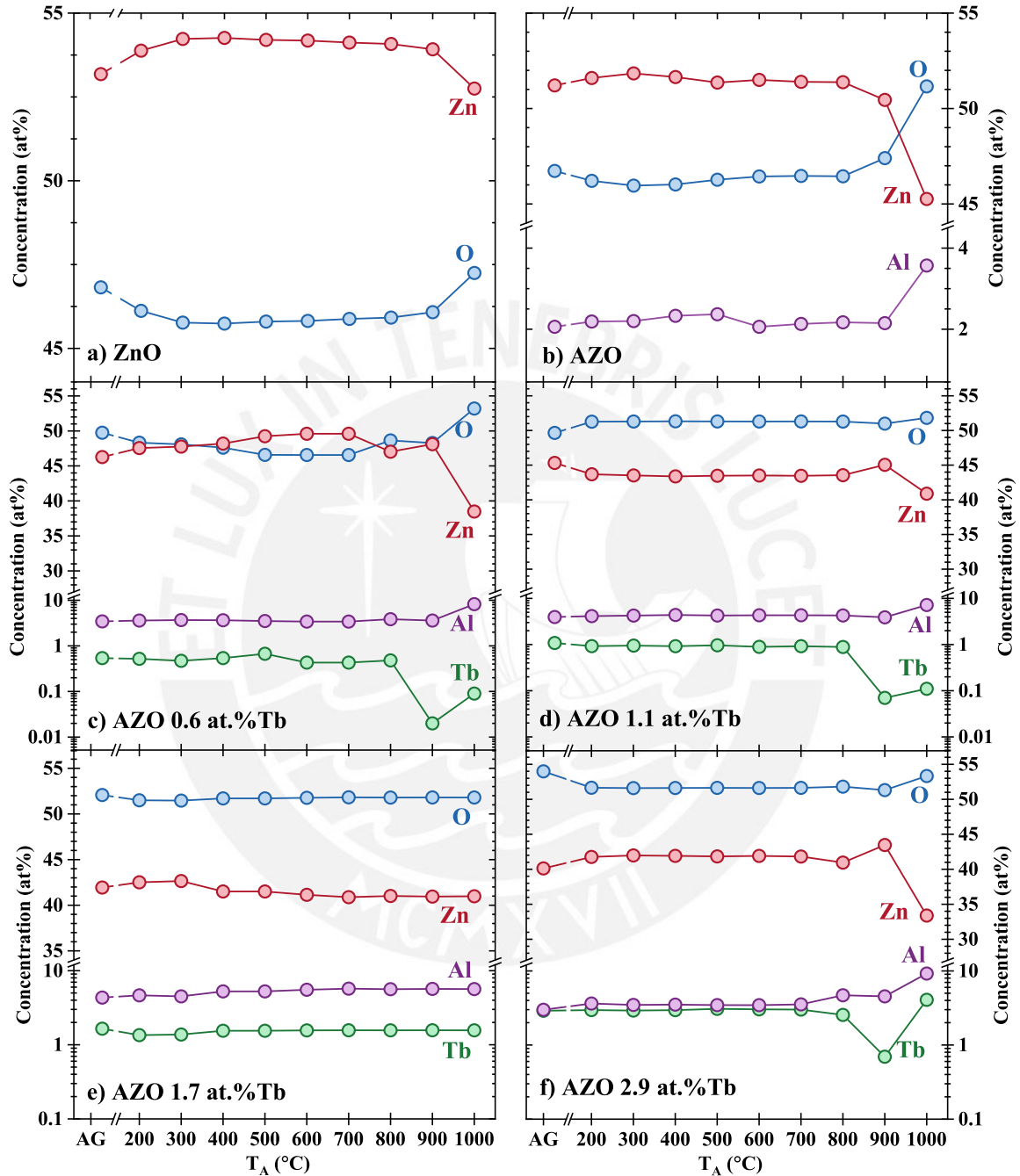


Fig. 5.2 Elemental composition against annealing temperature for pure ZnO, pure AZO and AZO:Tb with different Tb concentrations. Written values of Tb concentration correspond to the as-grown samples.

After annealing treatments, the elemental composition does not change considerably up to 700 °C for all samples, as can be seen in Figure 5.2. For higher temperatures, a slight O concentration increase can be noticed for most of the samples due to the oxygen diffusion towards oxygen vacancies. Thus a variation on the Tb, Zn and Al concentrations is also observed. Furthermore, the impact of introducing Tb on the oxygen concentration can also be noticed.

When ZnO and AZO are prepared by RF sputtering, usually there is a preferred orientation growth that can also be affected by the substrate surface, deposition temperature, growth atmosphere and working pressure [151, 152]. This preferred orientation is usually along the c-axis, which is perpendicular to the film surface, and can be explained by the model proposed by van der Drift, "survival of the fastest" [153]. This model states that the growth starts with nuclei oriented towards different directions. Each nucleation center will have their own growth rate that will be largest for those directions with the least surface energy. In other words, the plane that has the least surface free energy will dominate the crystalline structure of the film as crystals will grow the fastest along that direction. In ZnO, the (002) plane (c-axis) has the minimum surface free energy [154], thus the growth direction would be parallel to the c-axis. This can be noticed for both pure ZnO and pure AZO films in the diffraction patterns in Figure 5.3. The only preferred growth direction is on the (002) plane. To help identify the peaks observed, lines corresponding to the powder diffraction file for wurtzite ZnO have also been drawn (PDF 36-1451).

Annealing treatments improved the crystallinity of the films by making the grain size bigger after each treatment. This can be seen in Figure 5.4 where the crystallite size was determined by Rietveld refinement described in Section 3.2.3. Additionally, the estimated microstrain for both ZnO and AZO is also shown to decrease with the annealing temperature. Despite the limited accuracy of the estimations due to the detection of only the (002) and (004) peaks, the grain size and microstrain behaviour with the annealing temperature show a similar trend in both sets of samples. SEM images presented in the insets of Figure 5.5 a) and b) show the columnar growth along the c-axis perpendicular to the film surface.

Conversely, Tb introduction may affect the structure of ZnO by decreasing the grain size [34]. Boyn [155] reported that RE ions introduced in II-VI semiconductors can occupy lattice sites by substituting the metal ions, and also interstitial sites where the impurity associates with an intrinsic defect forming a complex. Due to the larger ionic radius of  $Tb^{3+}$ , when the ions are introduced in the lattice, either as a substitutional or interstitial ion, it will be distorted and its crystallinity reduced. Furthermore, increasing annealing temperature could increase the stress in the film [36]. It also may improve crystallite growth depending on the concentration

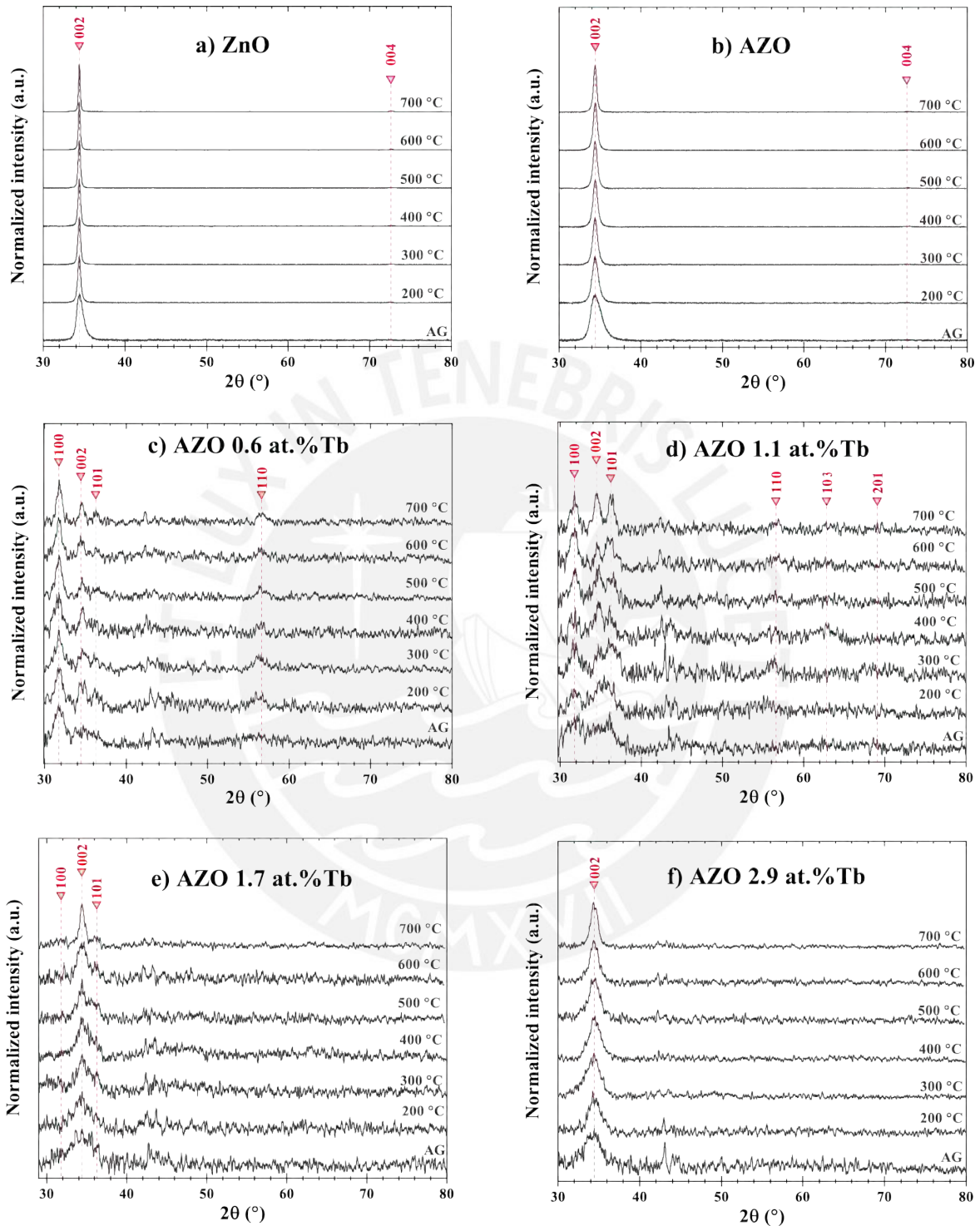


Fig. 5.3 X-ray diffractograms of pure ZnO in a), pure AZO in b) and AZO with different Tb concentration in c)-f) for the as-grown state and annealing temperatures between 400 °C and 700 °C.

of Tb in the sample [156, 157]. Reportedly, rare-earth ions in AZO increase (decreases) the crystallite size when doped with Eu (Gd,Sm), while the opposite effect occurs with the microstrain [32, 31, 33]. The samples containing Tb in this work suggest a nanocrystalline structure as can be seen in Figure 5.3 c)-f). These diffractograms show broader peaks along the planes corresponding to the ZnO wurtzite structure in comparison to the pure AZO samples. No other peaks were detected.

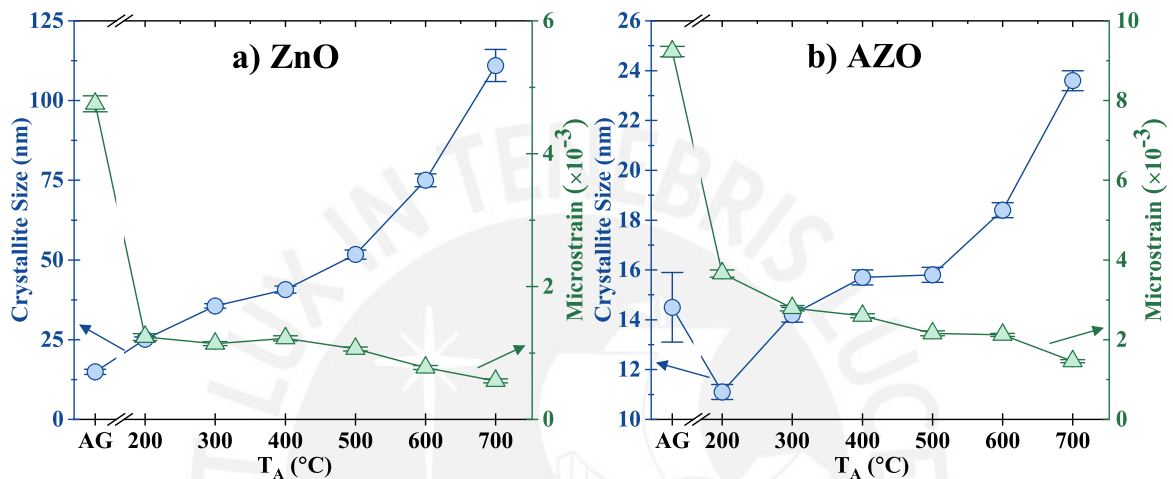


Fig. 5.4 Crystallite size and microstrain for a) ZnO and b) AZO at each annealing temperature shown, estimated from Rietveld refinement of the diffractograms shown in Figure 5.3 a) and b), respectively. Error bars correspond to the errors estimated from the refinement.

For the samples with 0.6 at.% and 1.1 at.% Tb, there is no clear preferential orientation. Similarly to the undoped cases, annealing treatments enhance the crystallinity of the films. Contrastingly, the samples with 1.7 at.% and 2.9 at.% Tb do show a preferential orientation along the (002) plane, although the intensity is rather low in comparison with the undoped cases. Notice that for most diffractograms shown in Figure 5.3, especially in all the lower intensity AG states, there are small peaks at around 42°. These peaks also appeared when measuring the fused silica substrate alone. Overall, Tb introduction in AZO induces structural disorder and the grains that show a preferential direction, for instance along the (002) plane, seem to be fewer in comparison with pure AZO, where the intensities are much higher.

SEM images in Figure 5.5 show the top view of the 400 °C annealed samples. In a), pure ZnO shows bigger, clearly defined grains. In the inset figure, the columnar growth perpendicular to the surface is evident. However, small crystallites can be observed near the Si surface which appear to have random orientations. In b), something similar can be observed for AZO, although the smaller columns have a comparable orientation to those bigger crystallites. These structural characteristic in both pure samples can be associated to the van der Drift



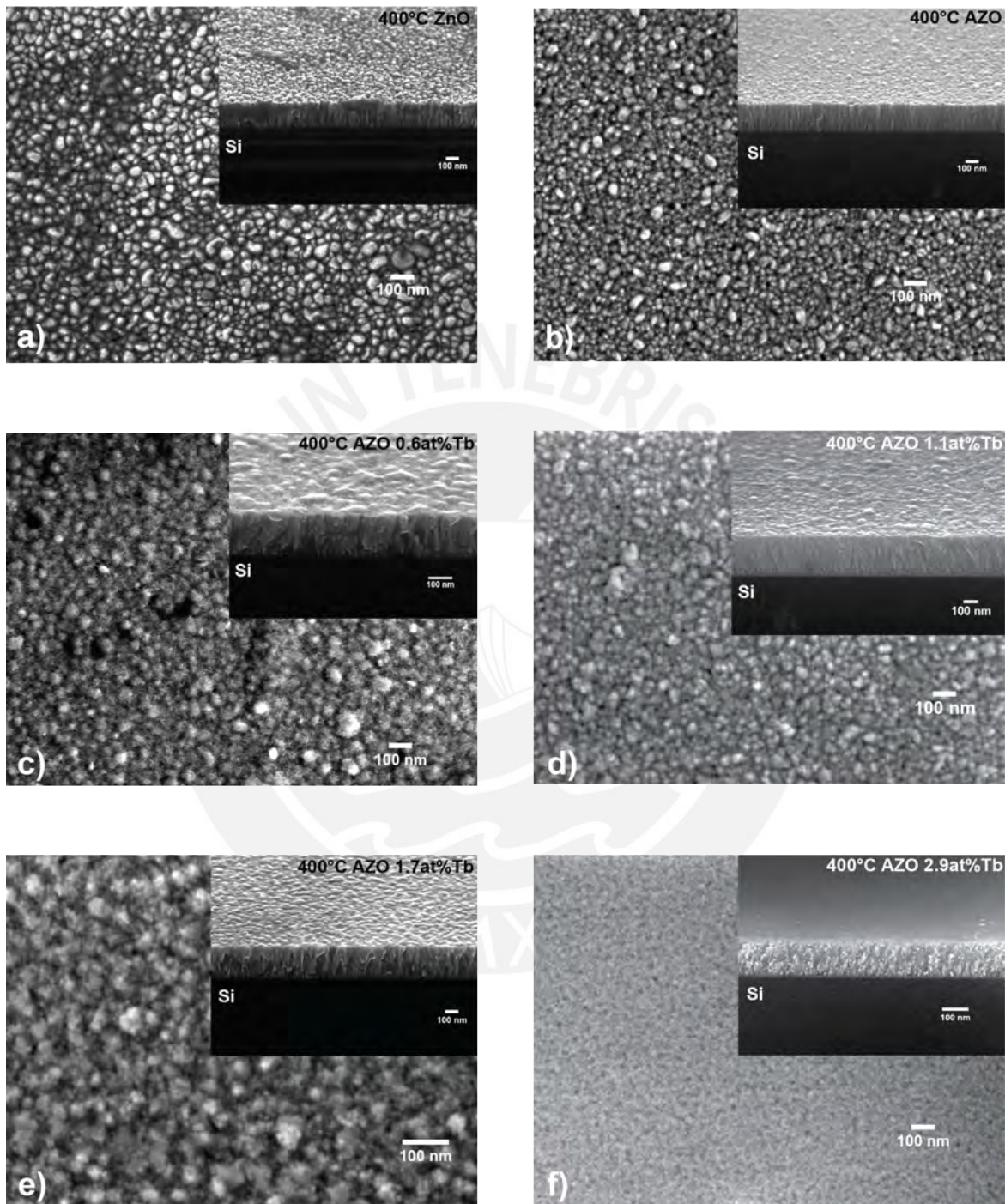


Fig. 5.5 Top view and 25° tilted cross-section (insets) SEM images of pure ZnO in a), pure AZO in b) and AZO with different Tb concentration in c) to f). All samples shown were annealed at 400 °C.

model where the more vertically oriented planes dominate the growth of the film after the first initial stage where nuclei with different orientations are formed. For the Tb embedded samples, taking the top-view images were more challenging as images appeared with white artifacts that increased their intensity with time. These artifacts could be attributed to electrons being accumulated at the surface. This might imply that samples containing Tb increase their electrical resistivity. Hu and Peterson [158] proposed that doping ZnO with rare-earths such as scandium or yttrium increase considerably the resistivity due to a phase segregation of insulating rare-earth oxide layers located at grain boundaries that also slows grain growth. The insets in Figure 5.5 c) to f) show smaller grains in comparison to the undoped cases, which may be attributed to the effect of Tb oxide layer formation surrounding the oriented grains that inhibit their growth.

### 5.1.2 Optical properties

Transmittance measurements together with optical models developed in our research group were used to determine the thickness and optical constants such as the complex refractive index ( $n$ ), absorption coefficient ( $\alpha$ ), optical band gap ( $E_g$ ) and Urbach energies ( $E_U$ ). These models and methods were briefly described in Section 2.1. Experimental transmittance and the corresponding fits can be seen in Figure 5.6 for ZnO in the spectral range from 250 nm to 1350 nm. The figure also shows the estimated  $n$  (curves) and  $\alpha$  (points in Tauc-plot) for each annealing temperature. To describe the absorption coefficient, first we assume that the band edge is at lower energies than the "shoulder"-like region and the band-fluctuations (BF) model was used to describe the absorption coefficient in this region. The solid lines in the Tauc-plot in Figure 5.6 are the fitted curves for each temperature. The insets show a decrease of the estimated  $E_U$  and  $E_g$  with the temperature.

However, these results do not take into account the characteristic excitonic behavior of ZnO, i.e., the BF model alone does not consider the excitonic transitions that are responsible of the shoulder-like section. To account for this transitions, a combination of the Elliot model and the BF model (EBF) was used to describe  $\alpha$ . Figure 5.7 shows the absorption coefficient fit (black curve) on the left, for the as-grown, 400 °C and 700 °C annealed samples. The red curve is the continuum component and the blue, purple and green curves correspond to the discrete components of first, second and third-to-tenth order, respectively. It can be noticed that as the annealing temperature increases, the excitonic region is more noticeable. The center figure shows the estimated band gaps in red and the exciton binding energies in blue against annealing temperature. The band gap noticeably decreases when annealed at 200 °C and then reduces slowly when further increasing the annealing temperature.

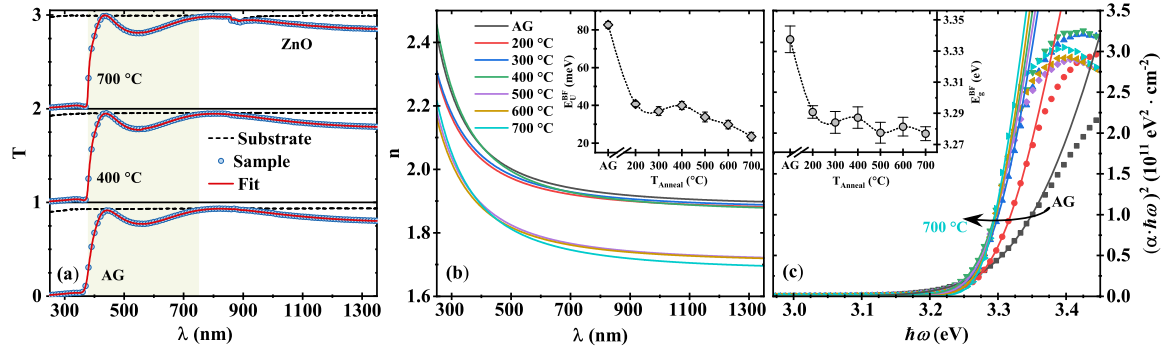


Fig. 5.6 Transmittance fits for pure ZnO films (a), estimated refractive index (b) and absorption coefficients in Tauc-plot (c) for each annealing temperature. The band-fluctuations model was used to describe the absorption coefficient as can be seen in solid lines. It can be noticed that the band gap decreases with annealing temperature. The insets show the estimated band gaps  $E_g$  and Urbach energies  $E_U$  against annealing temperature.

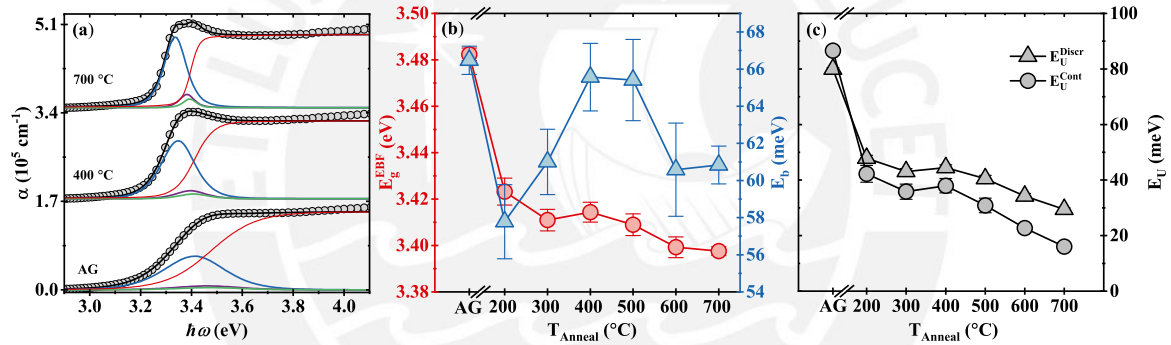


Fig. 5.7 Experimental and fitted absorption coefficient (a), band gap  $E_g$  and binding energies  $E_b$  against annealing temperature (b) and Urbach energies  $E_U$  versus annealing temperature (c) for pure ZnO.

The estimated binding energies are around 60 meV which is similar to the known value in the literature [159, 160]. The figure on the right shows the decreasing Urbach energy for the discrete ( $E_U^{Discr}$ ) and continuous ( $E_U^{Cont}$ ) components of the model.  $E_U^{Discr}$  accounts for the contribution to the broadening from the lattice disorder related to the discrete states transitions, whilst  $E_U^{Cont}$  for the broadening due the disorder related to the continuum states. In the as-grown state both Urbach energies are highest, which seems reasonable as the sample have shown a lower crystallinity according to the X-ray diffractogram (see Figure 5.3 a)). Increasing annealing temperature reduces the Urbach energy which also correlates to the behaviour with the diffractograms as the crystallinity is improved. Furthermore, it also correlates to the enhanced excitonic transitions observed in the absorption coefficient.



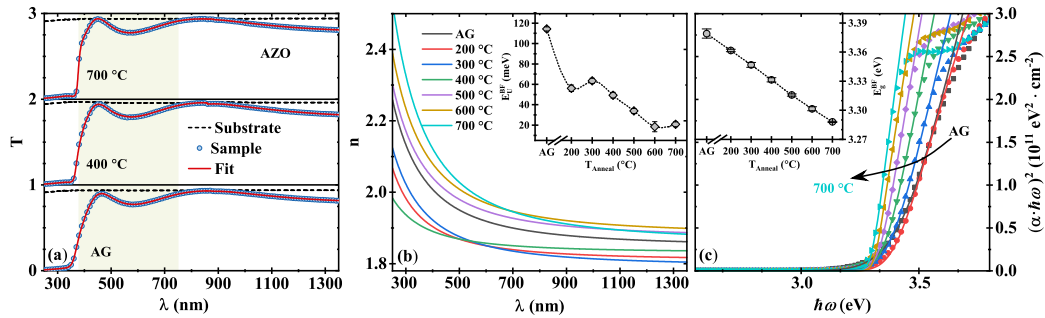


Fig. 5.8 Transmittance fits for pure AZO films (a), estimated refractive index (b) and absorption coefficients in Tauc-plot (c) for each annealing temperature. The band-fluctuations model was used to describe the absorption coefficient as can be seen in solid lines. It can be noticed that the band gap decreases with annealing temperature. The insets show the estimated band gaps  $E_g$  and Urbach energies  $E_U$  against annealing temperature.

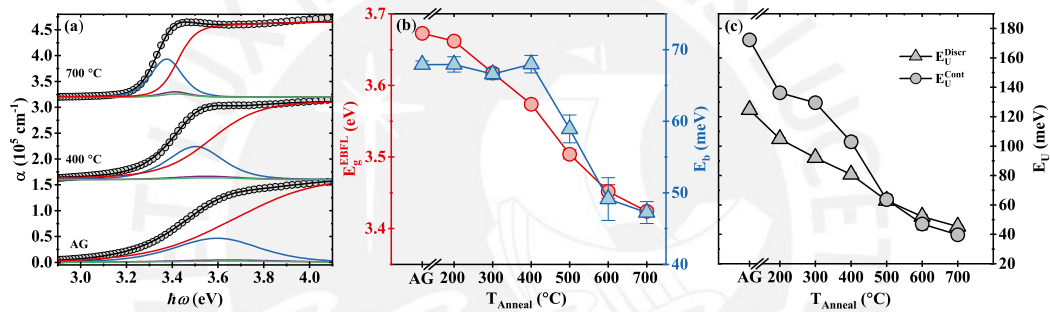


Fig. 5.9 Experimental and fitted absorption coefficient (a), band gap  $E_g$  and exciton binding energies  $E_b$  against annealing temperature (b) and Urbach energies  $E_U$  versus annealing temperature (c) for pure AZO. Errors were obtained from the fit and some of the corresponding error bars are smaller than the symbol size.

Figure 5.8 (a) shows the optical transmittance of AZO in the as-grown state and the annealing temperatures displayed. The estimated refractive index for each annealing temperature is shown in (b), while the absorption coefficient (data points) displayed in a Tauc-plot in (c) depicts the red-shift of the absorption edge when calculated with the BF model. The insets show the estimated Urbach energies and the band gap where both parameters tend to decrease when increasing the annealing temperature. In contrast to the band gap behaviour with the temperature for ZnO, the decrease is almost linear for AZO. Figure 5.9 (a) shows the absorption coefficient for AZO (circles), the corresponding EBF model fit (black line) and the model's discrete (blue for first order, purple for second, green for third-to-tenth orders) and continuum (red line) components. As the annealing temperature increases, the excitonic band is more defined. This could be due to an enhancement of excitonic transitions attributable to an improvement of the crystallinity of the film as can be seen also in the X-ray

diffraction patterns in Figure 5.3 (b). The estimated band gap and excitonic binding energy for each annealing temperature can be seen in (b). The band gap estimated with both BF and EBF models decreases after each annealing step, while the binding energy remains around 68 meV up to 400 °C, after which it decreases with further increases of the temperature. One possible source for the band gap reduction might be attributable to a reduction of the carrier concentration with the temperature increase, following the Burstein-Moss effect, as oxygen has a higher probability to occupy oxygen vacancy sites. A discussion on this with the estimated Hall carrier concentration will be presented in Section 5.2.1. Another possible source for the band gap decrease could be hinted at by the microstrain reduction presented in Figure 5.4, which shows a similar behaviour as the band gap, especially for the ZnO films. The decrease of microstrain could imply a reduced bonding strength thus reducing the energy needed for an electron to make a transition to the conduction band, i.e. the band gap would be reduced. Furthermore, the crystallite size reduction could also be correlated to the band gap decrease [161, 162].

The exciton binding energy can be expressed as

$$E_b = \frac{\mu e^4}{32\pi^2 \hbar^2 \epsilon_r^2 \epsilon_0^2} = \frac{\mu}{m_0 \epsilon_r^2} \cdot 13.6eV \quad (5.1)$$

where  $\mu$  is the electron-hole pair reduced mass defined  $1/\mu = 1/m_e + 1/m_h$ ,  $\epsilon_0$  is the vacuum electrical permittivity,  $\epsilon_r$  is the dielectric constant and  $e$  is the electron charge. Generally, the hole mass is much heavier in most tetrahedrally bonded direct gap semiconductors [54], thus the reduced mass is closer to the electron effective mass.  $\epsilon_r$  values for bulk ZnO are around 8-9 [163]. Films investigated in this work, both pure and with added Tb,  $\epsilon_r$  have shown a lower value between 3.6 to 4 throughout the annealing temperature range. Thus,  $\epsilon_r$  would have a low impact on the magnitude of  $E_b$ . In consequence,  $m_e$  may have the largest influence on  $E_b$ . Annealing treatments could alter the band structure thus affecting the electron effective mass. It appears that up to 400 °C, at which the binding energies remain constant, the bands are not affected by the low annealing temperatures but further temperature increase does have an impact as the binding energy is reduced.

The estimated Urbach energies associated to the discrete and continuum components can be seen in (c), where both parameters decrease with the temperature increase. Similarly to ZnO, this effect can be observed in the curves (a), at lower temperatures there is a wider broadening for the discrete component, whilst in the continuum part the tail is broader. As temperature increases, the broadening of both components is reduced which can be correlated to the reduction of the Urbach energy.

When Tb is introduced, the transmittance and estimated refractive indices do not change considerably, as can be observed in Figure 5.10. The absorption coefficient near the absorption edge show a similar behaviour as in the pure AZO case. The Tauc-plot depicts a red-shift of the band edge as the annealing temperature increases and it shows this tendency when calculating  $E_g$  with the BF model in the inset figure. The Urbach energies tend to decrease also when increasing the temperature, indicating that the disorder in the film is reduced with higher temperatures.

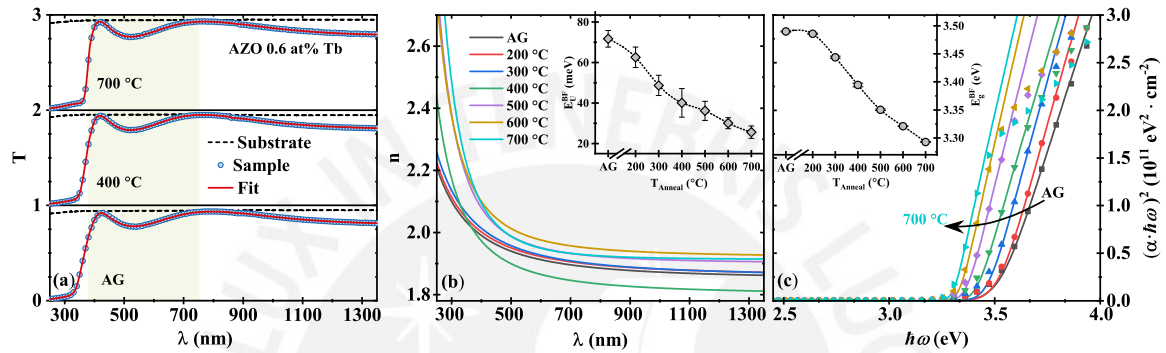


Fig. 5.10 Transmittance data and fits (a) for AZO films with 0.6 at.% Tb, estimated refractive index (b) and absorption coefficients in Tauc-plot (c) for each annealing temperature. The band-fluctuation model was used to describe the absorption coefficient as can be seen in solid lines. It can be noticed that the band gap decreases with annealing temperature. The insets show the estimated band gaps  $E_g$  and Urbach energies  $E_U$  against annealing temperature.

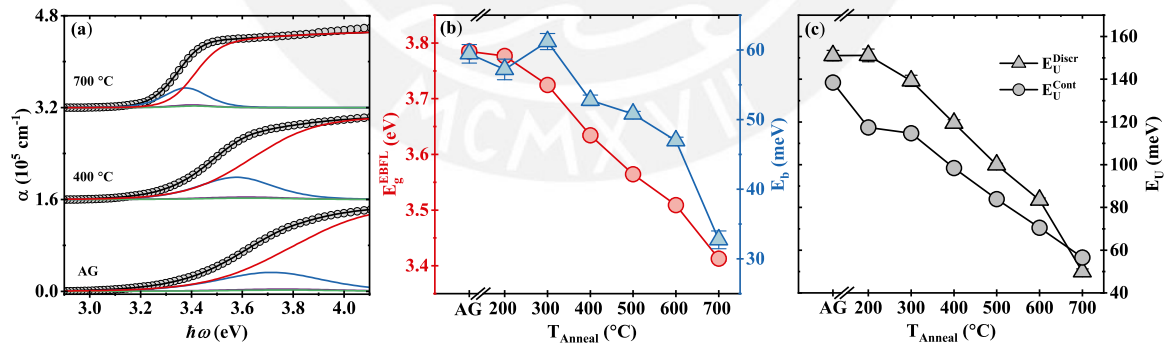


Fig. 5.11 Experimental and fitted absorption coefficient (a), band gap  $E_g$  and exciton binding energies  $E_b$  against annealing temperature (b) and Urbach energies  $E_U$  versus annealing temperature (c) for AZO films with 0.6 at.% Tb. Errors were obtained from the fit and some of the corresponding error bars are smaller than the symbol size.

When the Tb concentration increases, the transmittance is still high in the visible range as can be observed in Figures 5.12 and 5.14. The estimated band gaps with both models

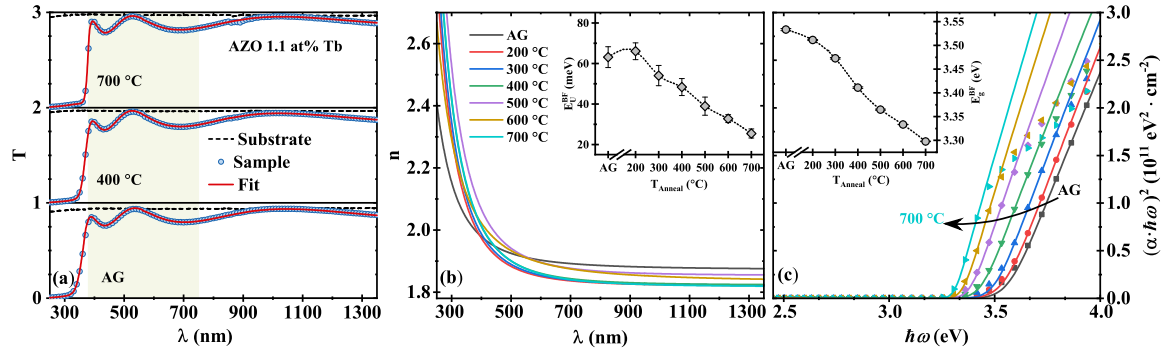


Fig. 5.12 Transmittance data and fits (a) for AZO films with 1.1 at.% Tb, estimated refractive index (b) and absorption coefficients in Tauc-plot (c) for each annealing temperature. The band-fluctuation model was used to describe the absorption coefficient as can be seen in solid lines. It can be noticed that the band gap decreases with annealing temperature. The insets show the estimated band gaps  $E_g$  and Urbach energies  $E_U$  against annealing temperature.

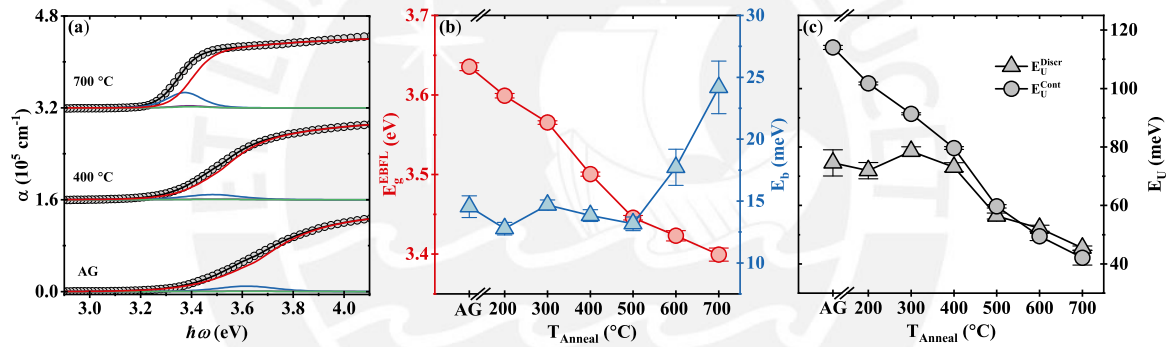


Fig. 5.13 Experimental and fitted absorption coefficient (a), band gap  $E_g$  and exciton binding energies  $E_b$  against annealing temperature (b) and Urbach energies  $E_U$  versus annealing temperature (c) for AZO films with 1.1 at.% Tb. Errors were obtained from the fit and some of the corresponding error bars are smaller than the symbol size.

show a decreasing behavior with the annealing temperature, although the EBF model gives higher values, similar to the pure ZnO and AZO cases. Tb addition to AZO may also increase the charge carrier density in the same way as Al does due to its higher oxidation state with respect to  $Zn^{2+}$ . As previously mentioned, the fact that only peaks related to the wurtzite ZnO structure are detected in XRD would hint that Tb ions are occupying Zn sites in the lattice, thus increasing charge carriers. When annealing temperature increases, the crystallinity is enhanced and oxygen would tend to occupy oxygen vacancy sites, thus reducing the carrier concentration. In consequence, the band gap would decrease according to the Burstein-Moss effect, similarly to the case of pure AZO. Tb suboxides ( $TbO_x$ ) formation can not be discarded and could have an impact on the optical properties [164]. Although

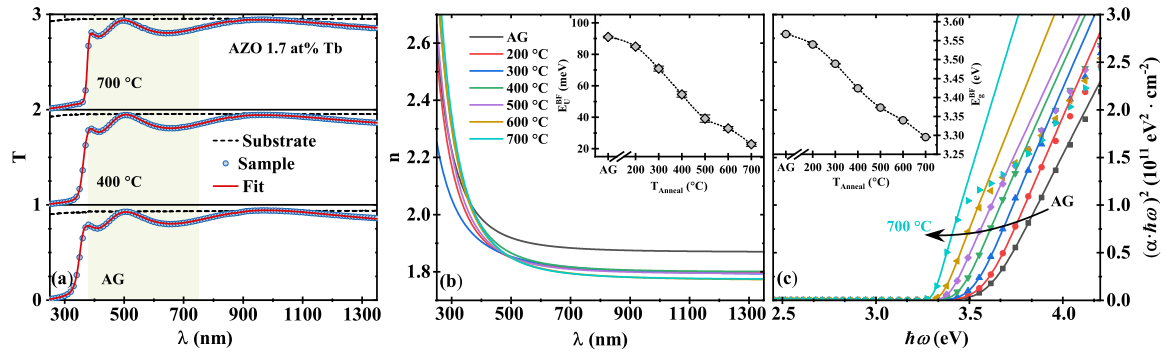


Fig. 5.14 Transmittance data and fits (a) for AZO films with 1.7 at.% Tb, estimated refractive index (b) and absorption coefficients in Tauc-plot (c) for each annealing temperature. The band-fluctuation model was used to describe the absorption coefficient as can be seen in solid lines. It can be noticed that the band gap decreases with annealing temperature. The insets show the estimated band gaps  $E_g$  and Urbach energies  $E_U$  against annealing temperature.

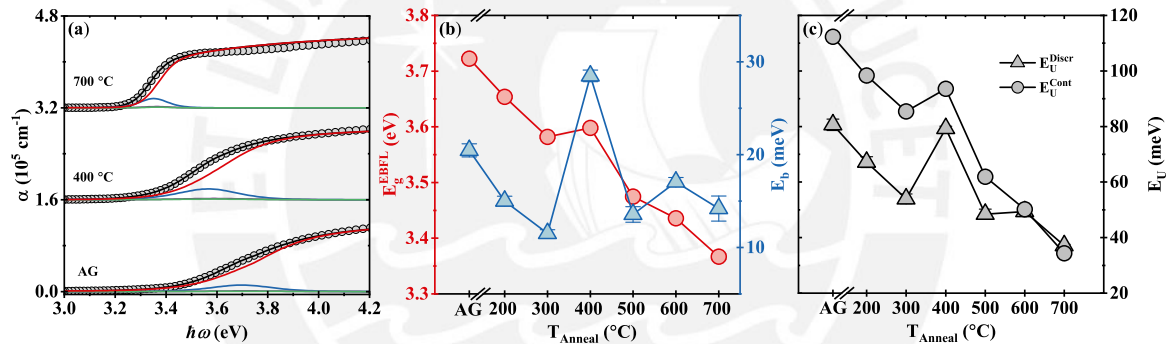


Fig. 5.15 Experimental and fitted absorption coefficient (a), band gap  $E_g$  and exciton binding energies  $E_b$  against annealing temperature (b) and Urbach energies  $E_U$  versus annealing temperature (c) for AZO films with 1.7 at.% Tb. Errors were obtained from the fit and some of the corresponding error bars are smaller than the symbol size.

TbO<sub>x</sub> tend to have oxygen vacancies at the grain boundaries which can accommodate oxygen by means of oxidation and adsorption [165], thus expecting an  $E_g$  increase,  $E_g$  is still reduced with the annealing temperature. An increase of the Urbach energies would also be expected when introducing Tb into AZO. Nonetheless, in the AG state and at low Tb concentration, the Urbach energy is less than that of AZO. This might be attributed to a local crystallization induced around the Tb ions, similar to what is observed in Al doped a-Ge [166, 167]. For all samples with Tb,  $E_U$  tend to decrease when increasing annealing temperature. This behaviour is expected from the crystallinity enhancement seen in the diffractograms in Figure 5.3. The most distinguishable change can be noticed in the binding energies estimated with the EBF model. For the sample with 0.6 at.% Tb, the binding energy is around 60 meV up to 300 °C

and then decreases. For the sample with 1.1 at.% Tb the binding energy stays at around 14 meV up to 500 °C where it starts to increase at higher temperatures. The only perceived  $E_b$  increment is for the sample with 1.7 at.% Tb, where it decreases slightly down to 12 meV at 300 °C and increases afterwards up to around 15 meV. The dielectric constant,  $\epsilon_r$  in Equation (5.1), for these samples take values from 3.6 to 4.6 around the excitonic absorption energy, hence the effect on  $E_b$  would be negligible. Analogously to the case of AZO, the changes described for  $E_b$  for each set of samples with Tb may be related to the changes in the band structure, together with the introduction of Tb as impurities could contribute to changes in the binding energy due to changes in grain size and their respective boundaries [168–170]. It is suggested that the impurities may add electron or hole traps that can form a bound electron-hole pair which in turn may affect the coulombic interaction of an exciton in the surroundings.

### 5.1.3 Luminescence activation/deactivation

Zinc oxide is well known for its near-band-edge luminescence (NBE), mainly composed by excitonic recombination, and defect-related luminescence. To study the effect of annealing on the light emission properties of ZnO, AZO and AZO:Tb cathodoluminescence and photoluminescence measurements were carried out on the samples. Figure 5.16 shows CL spectra of ZnO and AZO for different annealing temperatures from the as-grown state up to 1000 °C.

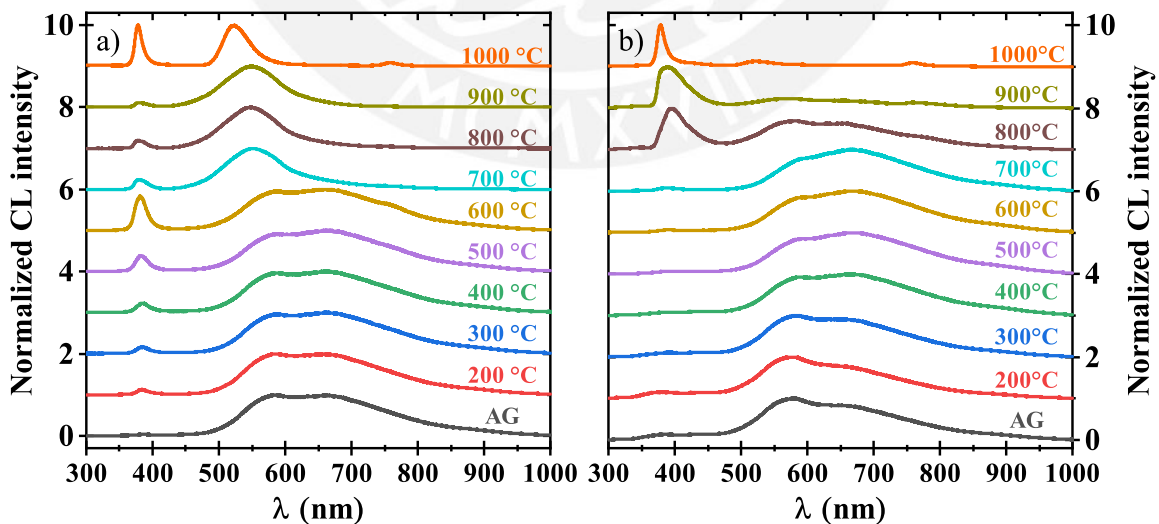


Fig. 5.16 Room temperature cathodoluminescence spectra of ZnO in a) and AZO in b) for the AG state and different annealing temperatures.



In the case of ZnO, we can notice that in the AG state, the main luminescence intensity is in the green and red spectral regions. These are associated to the light emission from recombination at certain point defects. There are some discrepancies in the literature as to whether which defects are involved in said transitions. The emission band centered at 670 nm might be due to recombination of electrons trapped at interstitial zinc sites  $Zn_i$  and holes trapped at interstitial oxygen  $O_i$  sites, according to Ahn et al. [171], assuming the  $Zn_i$  level is 0.22 eV below the conduction band minimum (CBM) [172]. However, the  $Zn_i$  energy level would be above the CBM according to the detailed first principles calculation done by Janotti and van de Walle [160] for native point defects in ZnO. Furthermore, according to these calculations, the NIR emission band centered at 760 nm is attributable to donor-acceptor transitions between oxygen vacancies  $V_O$  and zinc vacancies  $V_{Zn}$ , or also to transitions between shallow trap levels near the conduction band and  $O_i$  levels [173]. The band at 585 nm can also be attributed to recombination at  $O_i$  [174]. As temperature increases, the NBE emission at around 380 nm becomes more prominent up to 600 °C where the highest intensity is comparable to the defect emission. When further increasing the temperature, the defect-related emission again dominates the light intensity up to 900 °C. Notice that now the defect-related band shifted to 550 nm, which can be attributed to transitions between shallow trap levels and zinc vacancies  $V_{Zn}$  [173]. At 1000 °C, again the NBE emission intensity increases as much as the green band which is now centered at 525 nm, while the 760 nm NIR emission band is noticeable again.

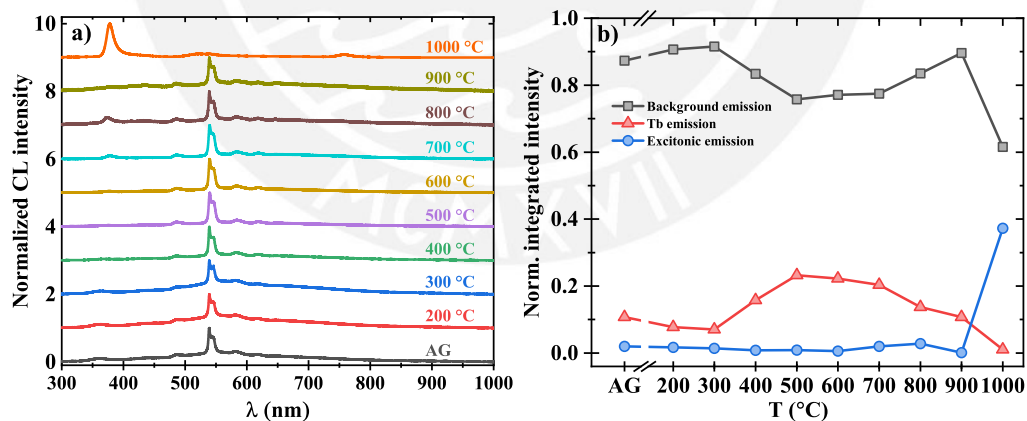


Fig. 5.17 Room temperature cathodoluminescence spectra of AZO with 0.6 at.% in a) for the AG state and different annealing temperatures. The normalized integrated intensities are shown in b), corresponding to the host-related (background), Tb-related and NBE (excitonic) emission.

In the case of AZO, a similar behavior on the defect-related light emission intensity is observed up to 700 °C. It can be noticed the broad band is composed mainly by three bands

centered at around 585 nm, 670 nm and 760 nm. The band at 585 nm has a higher intensity up to 300 °C, after which the intensity of the 670 nm band gets slightly stronger. The NBE emission intensity centered at ~380 nm is highest starting at 800 °C. At 900 °C and 1000 °C the NBE emission dominates the luminescence, while the behavior of the defect-related bands is similar to that shown by the pure ZnO sample.

When introducing Tb into AZO, characteristic Tb-related CL emission peaks appear along with a background emission that can be assigned to the defect-related transitions in ZnO/AZO. Figure 5.17 shows CL spectra of a sample with 0.6 at.% of Tb for different annealing temperatures. The NBE (or excitonic) emission can be observed at a rather low intensity until 900 °C. At 1000 °C the spectrum has a very similar shape with a dominant NBE band as the pure AZO annealed at the same temperature. In order to analyze the influence of the thermal treatments on the Tb-related and host-related emission, the areas corresponding to Tb, host (background) and NBE emission were integrated and normalized according to the procedure shown in Section 3.4.1. The Tb-related intensity from the AG state up to 300 °C remains similar. Afterwards, it increases as until 500 °C, which could be due to an increase of the optically active Tb ions due to the thermal treatments. However, the Tb-related intensity gets negligible as temperature increases until 1000 °C. On the other hand, the defect-related emission intensity has the correspondingly opposite behaviour until 900 °C, after which it drops due to a significant increase of the NBE emission at 1000 °C. The fact that there is no increase of the NBE emission when increasing annealing temperature may imply that the excitation mechanism of optically active Tb ions is of excitonic nature. This behaviour can also be noticed until 800 °C in Figure 5.18 and Figure 5.19 for samples with 1.1 at.% and 1.7 at.%, respectively. For higher temperatures there is a significant increase of the NBE emission. In both cases and unlike the case for the 0.6 at.% Tb sample, it seems that temperature increase of annealing treatments quenches the Tb-related emission.

Contrastingly, room temperature photoluminescence spectra obtained with an excitation wavelength of 325 nm (3.81 eV) of the samples with 1.1 at.% and 1.7 at.% presented in Figure 5.20 show almost no characteristic Tb emission except those in the AG state and annealed at 200 °C where a rather small band can be seen at 545 nm. Although there is a small band corresponding to the NBE emission starting at 500 °C for both samples, it seems PL band-to-band excitation mainly contributes to the emission from defect centers. This would further strengthen the idea that excitons are involved in the excitation of Tb ions. The bands located at around 760 nm for each spectrum (inside the shadowed region in Figure 5.20) could be attributable to defect transitions as previously described. However, as its intensity behavior is different as that shown in their respective CL spectrum and similar to



the PL band at 380 nm, it is assumed to be a second-order diffraction peak of this band. In the figure, these second-order peaks appear to be of higher intensity than their corresponding first-order peak due to a feature of the measurement system that also increases the noise at higher wavelengths. Other authors have also attributed this band to the second-order diffraction peak when using a 325 nm or lower wavelength laser source [175, 176].

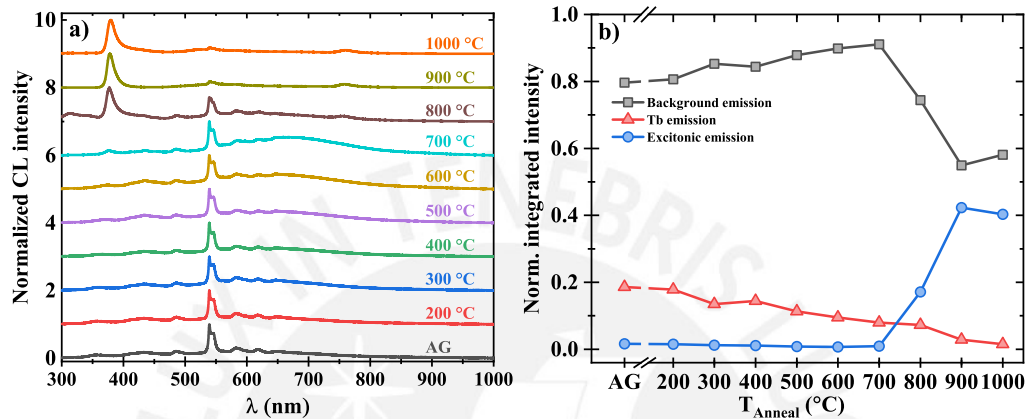


Fig. 5.18 Room temperature cathodoluminescence spectra of AZO with 1.1 at.% in a) for the AG state and different annealing temperatures. The normalized integrated intensities are shown in b), corresponding to the host-related (background), Tb-related and NBE (excitonic) emission.

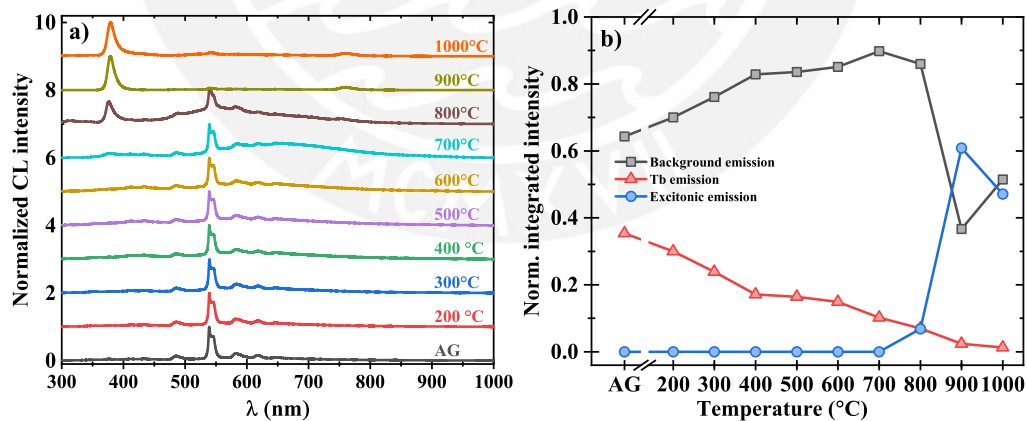


Fig. 5.19 Room temperature cathodoluminescence spectra of AZO with 1.7 at.% in a) for the AG state and different annealing temperatures. The normalized integrated intensities are shown in b), corresponding to the host-related (background), Tb-related and NBE (excitonic) emission.

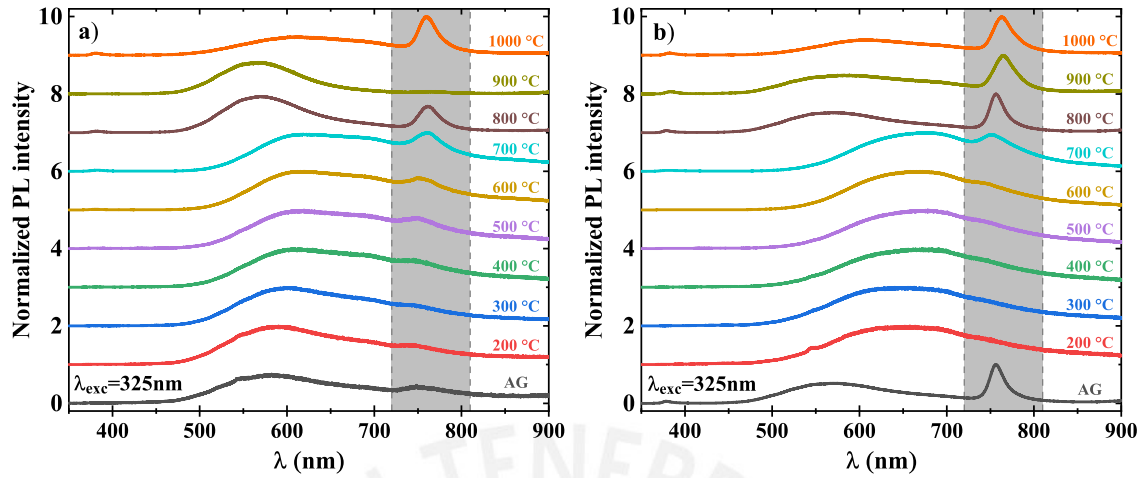


Fig. 5.20 Room temperature photoluminescence spectra taken at room temperature of AZO with 0.6 at.% in a) and 1.7 at.% in b) for the AG state and different annealing temperatures. The spectral bands at around 760 nm shown inside the shadowed regions are the second-order diffraction peaks of the 380 nm band.

## 5.2 On the excitation mechanism of optically active $Tb^{3+}$ centers in AZO

In order to investigate the possible excitation mechanism of Tb ions, temperature-dependent PL measurements were carried out on samples annealed at 400 °C with the same 325 nm excitation source. Again, this would be a band-to-band charge carrier excitation. In the undoped AZO case shown in Figure 5.21, there is a broad band that red-shifts when the sample temperature increases. There is also an intensity decrease as can be noticed from the signal-to-noise ratio in the normalized spectra.

For the samples with Tb as shown in Figures 5.22 and 5.23, characteristic Tb luminescence is obtained starting at 83 K. However, as sample temperature increases, both defect and Tb-related emission decreases. After normalization of areas as described in Section 3.4.1, the logarithm of the ratio between normalized Tb-related intensity  $I_{Tb}$  and its maximum  $I_{Tb_{max}}$  was plotted against the reciprocal of the sample temperature in an Arrhenius plot, as can be seen to the right side of the figures. The observed temperature dependence of  $I_{Tb}$  show non-linear behavior and a weak luminescence quenching up to around 200 K. The temperature regions which show an intensity decrease were fitted with an Arrhenius-like expression shown in Equation (5.2). This expression differs from the one in Equation (4.4)

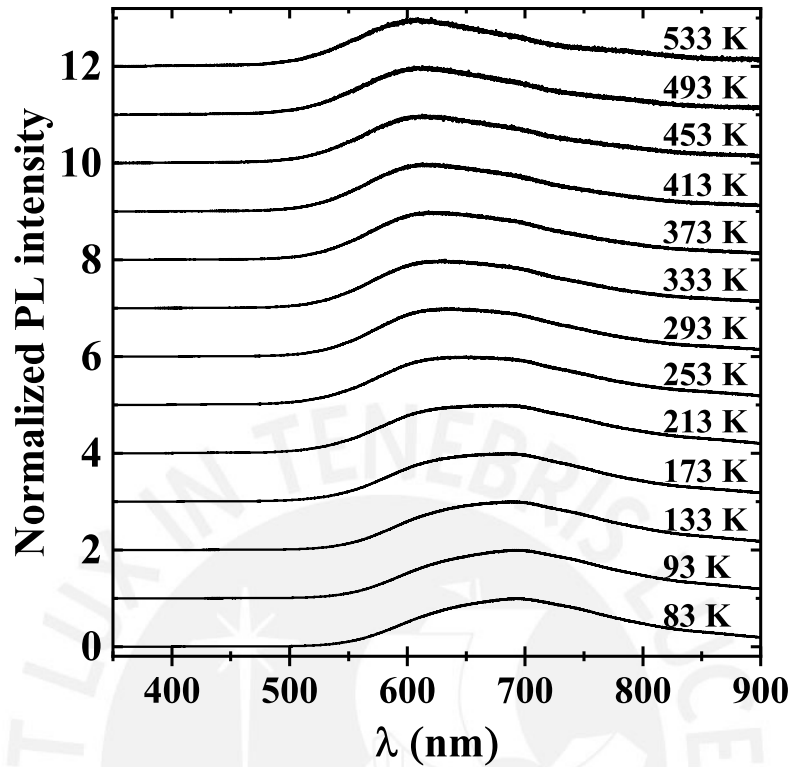


Fig. 5.21 Temperature dependent PL of the 400 °C annealed pure AZO film. The step was 20 K starting at 93 K but for better visibility the spectra is displayed every 40 K. The PL excitation wavelength for the measurements was 325nm.

used for ITO:Tb due to the features shown which are similar to those found for rare-earth doped AlN in the work of Lozykowski and Jadwisienczak [18].

$$I(T) = \sum_{n=1}^N \frac{A_n}{1 + e^{\frac{-\epsilon_n^b}{k_B} (\frac{1}{T} - \frac{1}{T_n})}} \quad (5.2)$$

Here  $k_B$  is the Boltzmann constant,  $T$  is the sample temperature,  $\epsilon_n^b$  are the thermal activation energies, which can describe one or more possible thermal quenching channels.  $A_n$  are independent amplitudes and  $T_n$  are related to the relative ratios of the competing thermal quenching processes. For the sample with 0.6 at.% (Figure 5.22), two independent fits were carried out for the decreasing regions. The lower temperature region was fitted with two activation energies, whilst the higher temperature region was fitted with only one. Meanwhile, for the sample with 1.7 at.% (Figure 5.23) the full temperature range was fitted with four activation energies. The fitting results for each sample are shown in Table 5.1.

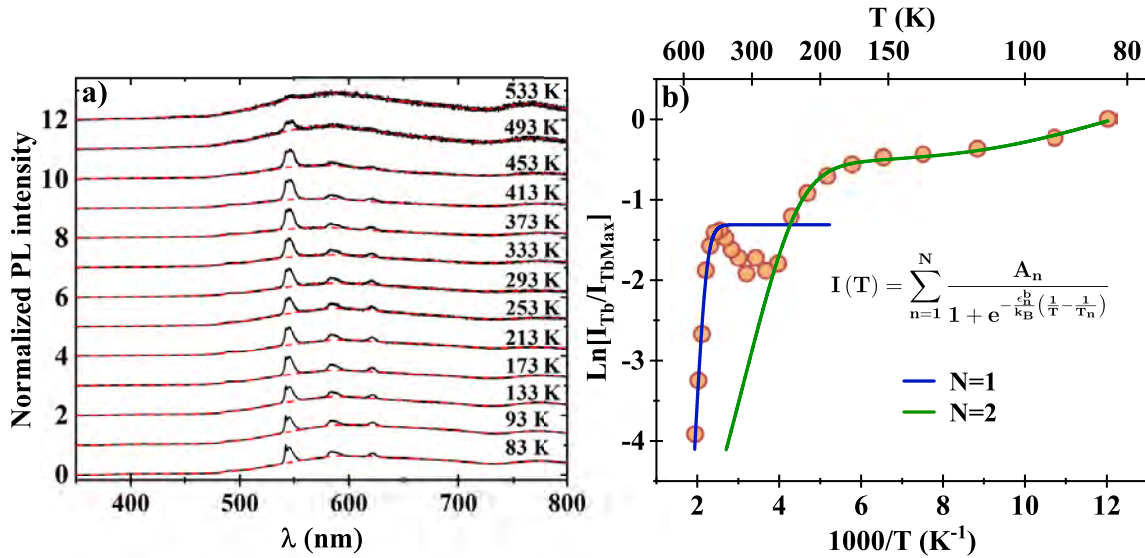


Fig. 5.22 Temperature dependent PL of the 400 °C annealed AZO with 0.6 at.% Tb film. The PL excitation wavelength for the measurements was 325nm.

Different excitation mechanisms of RE ions in a ZnO matrix have been proposed. For instance, taking as an example the excitation spectra of ZnS:Tm, Boyn [155] mentions the following RE excitation mechanism in II-VI semiconductors:

- a) Direct excitation of 4f levels that may result in radiative or non-radiative transitions to the initial level. Nonetheless, this excitation process is not efficient due to the small 4f-4f oscillator strengths.
- b) Indirect excitation via non-radiative energy transfer to the 4f shell in which a number of external impurity states may participate. As in the first case, this excitation may result in radiative transitions to the initial level and with a higher intensity as the oscillator strengths for the excitation of impurities are high. The optical transitions in this case could be of three kinds:
  - i) Transitions within an impurity, also known as "sensitizing center", which is located apart from the RE ion.
  - ii) Transitions between donor-acceptor complexes, in which the RE ions can act as donors due to their excess donated charge, allowing them to associate with impurities that function as acceptors. The transitions between these complexes involve the transfer of charge between the donor and acceptor.

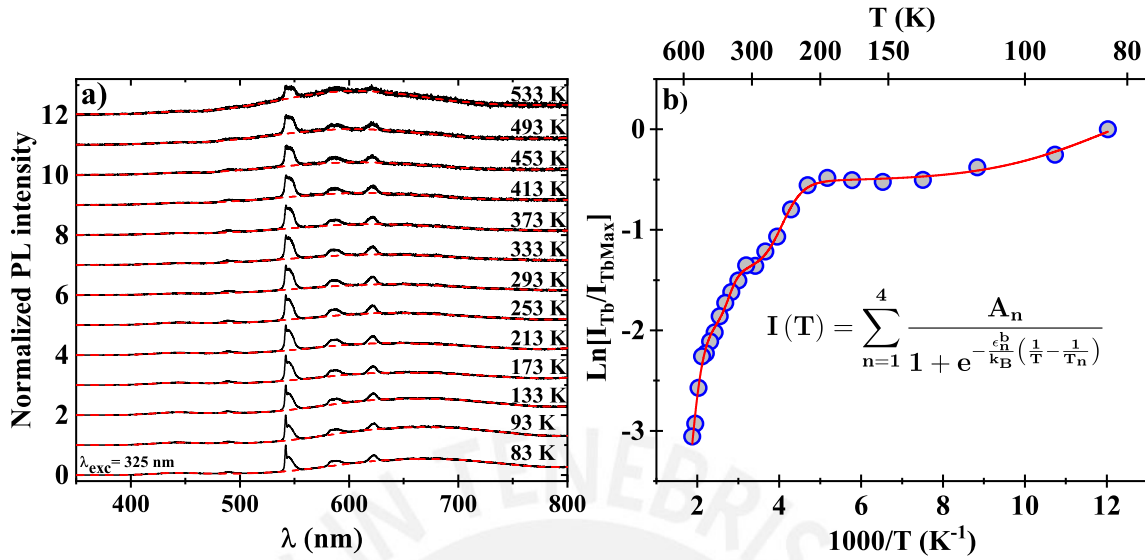


Fig. 5.23 Temperature dependent PL of the 400 °C annealed AZO with 1.7 at.% Tb film. The PL excitation wavelength for the measurements was 325nm.

- iii) Transitions between donor-acceptor pairs in which a RE ion functions as donor and any other kind of impurity as an acceptor. This would imply the transfer of a charge from the acceptor state to a shallow donor state.
- c) Indirect excitation via electron-hole pair or exciton creation with a subsequent non-radiative energy transfer to the RE ion. These generated excitons would be captured into impurity states that contain RE ions or complexes, followed by energy transfer to the 4f level in a similar way described in the previous case. Although, it is mentioned that the direct energy transfer from the exciton to the 4f states is less probable, especially at low temperatures, at which the probability for the transferred energy to be absorbed at an occupied 4f energy level is low due to a smaller spread of said levels.

Regarding the AZO:Tb films in this work, as mentioned in case a), the low probability of direct excitation makes this mechanism less likely to be the main excitation process. For the indirect non-radiative excitation in b)-i) involving ZnO/AZO intrinsic defects, the recombination energy at those defects should match the intra-4f transitions, mainly  ${}^7F_j \rightarrow {}^5D_4$  and, furthermore, there is a very weak interaction of the 4f-shell with the host states. Additionally, for b)-ii) and b)-iii) there must be a charge transferred to the 4f level which is unlikely due to the low energy excitation source of  $\sim 3.81$  eV (325 nm) [177]. Then, the focus in the remaining part of this section will be on case c), where the Tb<sup>3+</sup> PL excitation process is

due to the energy transfer from the recombination of an exciton that is bound to Tb ions or complexes.

Table 5.1 Best fitted parameters from Equation (5.2) for the Arrhenius curves shown in Figures 5.22 and 5.23. For the sample with 0.6 at.% Tb, single ( $N = 1$ ) thermal quenching process for the highest temperature region together with a dual ( $N = 2$ ) quenching process for the lowest temperature region were used to do the fitting. For the 1.7 at.% Tb sample, quadruple ( $N = 4$ ) quenching processes describe the intensity decrease throughout all the temperature range. Errors shown were obtained from the fit.

	AZO 0.6 at.% Tb		AZO 1.7 at.% Tb
	$N = 1$	$N = 2$	$N = 4$
$A_n$	$A_1 = 270 \pm 19$	$A_1 = 1$ $A_2 = 0.580 \pm 0.047$	$A_1 = 1$ $A_2 = 0.351 \pm 0.054$ $A_3 = 0.105 \pm 0.043$ $A_4 = 0.141 \pm 0.017$
$T_n(K)$	$T_1 = 454 \pm 4$	$T_1 = 78 \pm 3$ $T_2 = 230 \pm 3$	$T_1 = 78 \pm 4$ $T_2 = 239 \pm 6$ $T_3 = 356 \pm 13$ $T_4 = 499 \pm 9$
$\epsilon_n^b(meV)$	$\epsilon_1^b = 871 \pm 61$	$\epsilon_1^b = 49 \pm 18$ $\epsilon_2^b = 196 \pm 25$	$\epsilon_1^b = 58 \pm 25$ $\epsilon_2^b = 338 \pm 141$ $\epsilon_3^b = 642 \pm 413$ $\epsilon_4^b = 554 \pm 66$

Table 5.2 SPW and KS parameters obtained from Eqs. 4.5 and 4.7 using the two lowest activation energies derived from the thermal quenching behavior of the luminescence for the AZO samples with 0.6 at.% Tb and 1.7 at.% Tb. Error values shown were calculated by error propagation of the best fit activation energies presented in Table 5.1

		AZO 0.6 at.% Tb	AZO 1.7 at.% Tb
K-S	$J(eV)$	$0.910 \pm 0.018$	$1.84 \pm 0.76$
	$T(ev)$	$2.80 \pm 0.08$	$6.07 \pm 0.2.44$
SPW	$V_0(eV)$	$0.867 \pm 0.007$	$1.79 \pm 0.73$
	$\rho_1(nm)$	$0.391 \pm 0.011$	$0.260 \pm 0.053$

As in the previously proposed model for the excitation mechanism of  $Tb^{3+}$  ions in ITO, the activation energies estimated with Equation (5.2) for AZO:Tb could be associated to the binding energies of excitons that are bound to  $Tb^{3+}$ -related trap levels. These traps would be due to and located near clusters of Tb ions or defect complexes that includes at least one Tb ion [130]. The energy from the exciton recombination would be transferred to the  $Tb^{3+}$  exciting an intra-4f transition level.

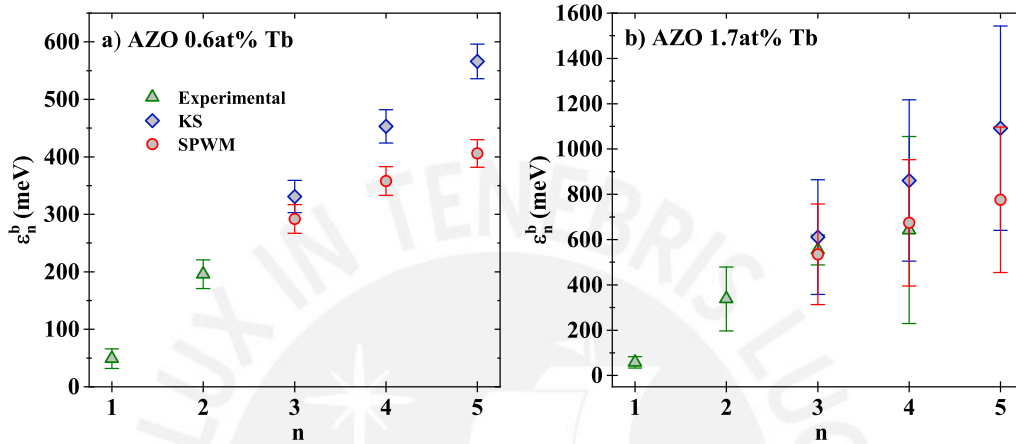


Fig. 5.24 Exciton binding energies calculated with the SPW and KS models for different cluster sizes. Experimental (green) values refer to the activation energies shown in Table 5.2 related to the thermal quenching effect.

Thus, both Koster-Slater and spherical potential-well models were used to estimate the host parameters and the binding energies of excitons bound to the Tb complexes. The estimated parameters using Equations (4.5) and (4.7) are shown in Table 5.2, while the binding energies against the number of Tb ions are shown in Figure 5.24. For both cases shown in Figures 5.22 and 5.23 the two lowest activation energies were used to do the calculation. In the particular case of the sample with 0.6 at.% of Tb, the third activation energy (871 meV, not shown in the graph) may be associated to a larger cluster size. It also could correspond to another type of quenching process that is occurring at higher sample temperatures.

In this way, the energy transfer mechanism from the bound excitons to the  $Tb^{3+}$  ion clusters throughout the temperature range investigated is proposed to be as follows. At the lowest temperature and under UV light excitation, excitons are formed and bound to the clusters with  $n$  number of ions ( $n = 1, 2, 3, \dots$ ), after which they recombine and transfer their energy non-radiatively to the cluster. A subsequent excitation of the  $Tb^{3+}$  ion is followed and de-excitation occurs by the characteristic photon emission from the ion. Increasing the temperature dissociates first the excitons with the lowest binding energy and no recombination occurs near the corresponding singlet cluster ( $n = 1$ ), thus reducing the Tb-related intensity. This can be observed in Figure 5.23 for the lower temperature range between 80 K and



$\sim 150$  K. Further increase of the temperature dissociate excitons with a correspondingly higher binding energy that are bound to clusters with  $n = 2, 3, \dots$   $Tb^{3+}$  ions and decrease even more the Tb-related intensity as can also be observed in the figure.

### 5.2.1 Electrical Properties of AZO

The samples of pure ZnO as well as those with Tb are very resistive, thus measuring their electrical properties with the available equipment was not possible. In the case of pure AZO, the electrical resistivity, majority carrier concentration and the mobility are shown in Figure 5.25. The resistivity increases with the annealing temperature, while the carrier concentration decreases. Inversely, the mobility increases with the temperature. A similar effect has been shown by other authors when annealing in air ambient [178, 179]. The electrical transport in ZnO is mainly influenced by intrinsic defects such as oxygen vacancies and zinc ions at interstitial sites which act as electron donors. Aluminum doping in ZnO gives an additional charge as Zn sites are replaced by Al, giving an excess of electrons that compensates the positive ionic charge [179]. The decrease of carrier concentration with the increasing annealing temperature may be due to a progressively reduction of oxygen vacancies as oxygen from the air ambient might be introduced into the structure [180]. Although a decreasing mobility may be expected due to the air annealing environment [181], the opposite occurs in our samples. This increase could be due to the greater grain size that each annealing step induces which reduces the scattering at the grain boundaries.

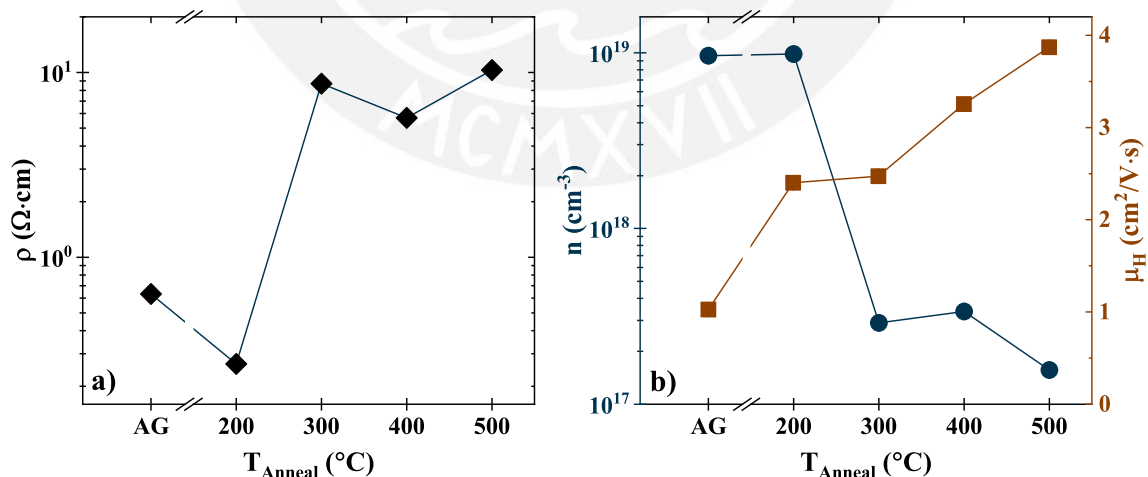


Fig. 5.25 Pure AZO electrical resistivity in a) with a comparison of carrier concentration  $n$  and mobility  $\mu_H$  in b) for each annealing temperature. For higher temperatures the data was not reliable or the measurement could not be carried out due to a higher resistive sample.



Although for higher electron concentrations the carrier-carrier scattering would reduce the mobility [182], at the carrier concentrations of the samples investigated and especially for those around  $10^{19} \text{ cm}^{-3}$ , the main source of scattering would be due the ionized impurities, while the grain boundary scattering would have less influence due to the bigger grains when increasing the annealing temperature. For the lower values of mobility observed at lower temperatures, the grain boundary scattering would have a higher influence. Nevertheless, there could also be other sources of scattering that affect the mobility of the samples [183].

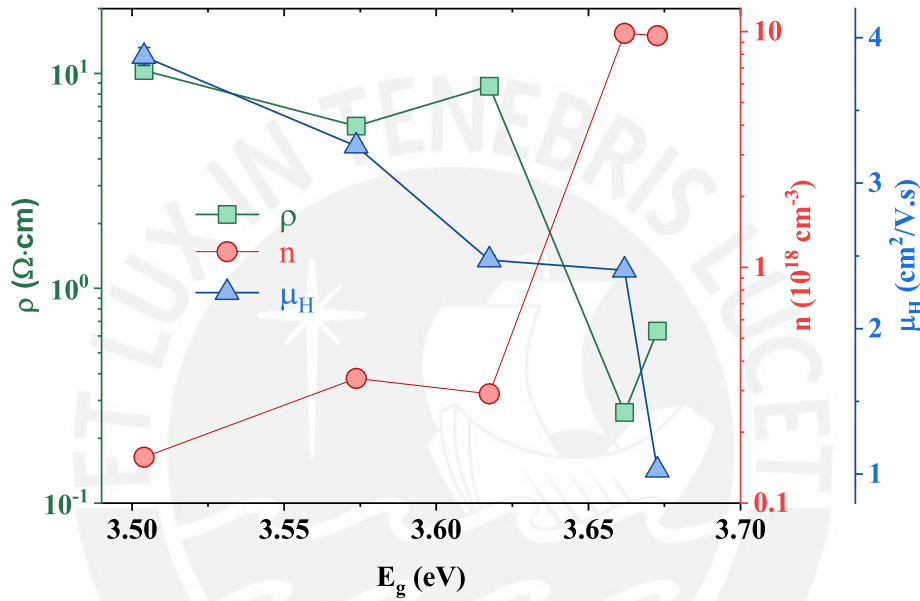


Fig. 5.26 Dependence on the Elliot-band-fluctuations band gap  $E_g$  of the electrical resistivity  $\rho$ , charge carrier concentration  $n$  and charge Hall mobility  $\mu_H$ .

The dependence of  $\rho$ ,  $n$  and  $\mu_H$  on the band gap  $E_g$  estimated with the Elliot-band-fluctuations model is shown in Figure 5.26. The increase of  $E_g$  may be induced by the increment of carrier concentration due to the Burstein-Moss (BM) effect [184, 185] following the relationship

$$\Delta E^{BM} = \frac{h^2}{8\pi^2} \frac{(3\pi^2 n)^{2/3}}{m^*} \quad (5.3)$$

which considers a parabolic band for a degenerate n-type semiconductor [186]. Annealing treatments could also modify the band structure of the material and consequently change the density of states effective mass. Following the definition for the classical mobility  $\mu = \frac{e\tau_s}{m^*}$ , where  $e$  is the electron charge,  $\tau_s$  is the mean scattering time and  $m^*$  is the effective mass, it can be seen that the mobility is affected by  $m^*$ . From Figure 5.26 it can be noticed that the Hall mobility  $\mu_H$  decreases with  $E_g$ , while the opposite occurs with annealing temperature

as seen in Figure 5.25. This increase of  $\mu_H$  would also hint at a reduction of  $m^*$  at higher annealing temperatures, which would enhance the BM shift according to Equation (5.3). However, the BM effect does not fully account for the band gap decrease with the annealing temperature. Assuming the effective mass to be  $m^* = 0.28m_e$  [183],  $\Delta E^{BM}$  values are between 5 meV to 60 meV.

### 5.3 Summary

The introduction of terbium into AZO by means of RFMS deposition while actively cooling down the substrates has proved to be successful in order to obtain characteristic Tb luminescence. The as-grown samples, regardless of Tb content, showed already this luminescence, although it greatly affected the structural, optical and electrical. The crystalline structure of AZO that showed a preferential growth direction along the (002) plane similar to that of ZnO, was heavily influenced when Tb was introduced as different orientations were observed in the diffractograms. As could be seen on the SEM images, samples with Tb appear to have reduced grain size and further, it seems that a higher Tb concentration induces smaller grains. Annealing showed an enhancement on the crystallization of pure ZnO and AZO. On the other hand, it only showed slight crystallization enhancement in all samples with Tb.

Although all samples with and without Tb have shown a high optical transmittance, the optical parameters estimated with the models employed in this work are strongly affected by the introduction of Tb, as well as with the thermal treatments. Tb containing samples show a slightly higher band gap in comparison to pure AZO. The Urbach energies estimated with the BF model have smaller values at low Tb concentration, whilst with the EBF model the opposite occurs as the largest values of  $E_U$  were retrieved at the concentration of 0.6 at.% Tb.

All samples have a larger estimated band gap with the EBF model than with the BF model alone. This is expected as the discrete levels are introduced to take into account the excitonic transitions. However, for samples in the AG state, annealed at low temperatures or containing Tb, the contribution from discrete states in the EBF model may not be of considerable influence so that only the BF model could be considered for parameters estimation. Whether to definitely use one model or the other to estimate the optical parameters will still require more data evaluation and discussion from the materials investigated in this work, as well as with other materials. Nonetheless, the EBF model allows the estimation of band gap considering the excitonic transitions according to Elliot's formulation and the Urbach energies of both discrete and continuum states.

For practical purposes, the EBF model would be used whenever the characteristic excitonic absorption peak is noticed in the spectrum. Otherwise, the BF model would give reasonable results.

As previously mentioned, characteristic Tb emission was obtained when excited with an electron beam, and slightly enhanced at the annealing temperature of 400 °C for the sample with 0.6 at.% Tb. Otherwise, the intensity always decreased with the increase of annealing temperature. At room temperature (RT) the samples with Tb did not show characteristic Tb emission when excited with 325 nm (3.81 eV), even though the excitation is band-to-band and energetically higher than the  $^7F_j \rightarrow ^5D_3$  transitions. This effect is contrary to what has been shown in the temperature dependent PL measurements where after increasing the temperature back to RT did show Tb-related peaks. This may suggest that raising the temperature after cooling down or the prolonged exposure of the sample to the excitation source may influence the competition of the radiative and non-radiative processes that could be occurring between the optically active Tb ions and the host-related defects. Moreover, the temperature-dependent PL measurements allowed to determine activation energies that could be associated to excitons that are bound to Tb ion clusters or Tb complexes that include at least one Tb ion together with intrinsic host defects. These clusters or complexes induce trap levels where the excitons are captured and their recombination energy is transferred to the optically active Tb ion. These cluster-exciton or complex-exciton systems are modeled by the SPW and KS models, where their associated parameters were calculated with two lowest binding energies estimated from fitting the experimental data with an Arrhenius-like function. Although the estimated parameters were not in agreement with those reported for AZO, it allowed the prediction of binding energies for clusters with 3 or more ions. For the sample with 1.7 at.% Tb this resulted in a good agreement with the experimental values obtained with the Arrhenius equation.

Unfortunately, introducing Tb into AZO under the described conditions in this work, has had a negative impact on the electrical conductivity. Notwithstanding the AZO:Tb films' electrical properties could not be investigated, those of AZO could. The results have shown low quality of the films, particularly regarding the resistivity as high values emerged from the measurements. Low temperature (200 °C) annealing enhanced slightly the conductivity but a further temperature increase was detrimental for the carrier concentration, even though the mobility slightly increased.

# Chapter 6

## Conclusions

Transparent conductive oxides (TCOs) are used in a wide range of applications due to their known excellent optical and electrical properties. Introducing a new property such as rare-earth (RE) characteristic luminescence in order to take advantage of the TCO's wide band gap, could open a new pathway for applications such as in light-emitting devices or photovoltaics. Nevertheless, by making TCOs host of RE ions, their structural, optical and electrical properties might be altered.

This study has addressed the effects of introducing terbium in ITO and AZO films and also how the post-deposition annealing treatments of the samples impact their physical properties. Furthermore, it is depicted throughout how both materials differ when Tb is introduced as an optically active luminescent center.

A common ground for both materials investigated were the deposition technique. Radio frequency magnetron sputtering has proven to be a good way to prepare the materials, particularly taking advantage of low temperature deposition by actively cooling the substrates. In the case of ITO, it allowed for a thermal activation of Tb-related luminescence by post-annealing treatments. For AZO, it allowed Tb ions to be optically active even in the as-grown state. In both cases, the transparency in the visible range was very good, especially for AZO:Tb. In both materials, the as-grown state showed a nanocrystalline or even amorphous structure.

The increase of Tb concentration in ITO quenched the luminescence at around 3 at.% Tb. On the other hand, Tb concentration in AZO was only around 2.9 at.% Tb at most, under the deposition conditions. Post-deposition thermal treatments enhanced the Tb-related emission in ITO starting at around 470 °C. These treatments also altered the shape of the spectrum in

the sense that at each temperature the peaks due to the crystal field splitting had different intensities. The most remarkable change was at 650 °C where the peak corresponding to the  ${}^5D_4 \rightarrow {}^7F_2$  transition at 650 nm had a comparable intensity with the  ${}^5D_4 \rightarrow {}^7F_5$  transition which is usually the most probable for  $Tb^{3+}$ . In AZO, there were resolved peaks related to the crystal field splitting. Furthermore, the increase of annealing temperature reduced the  $Tb$ -related emission and increased the host's defect-related emission at temperatures lower than 700 °C, and at higher annealing temperatures the near-band-edge emission intensity associated to the host's excitonic transitions.

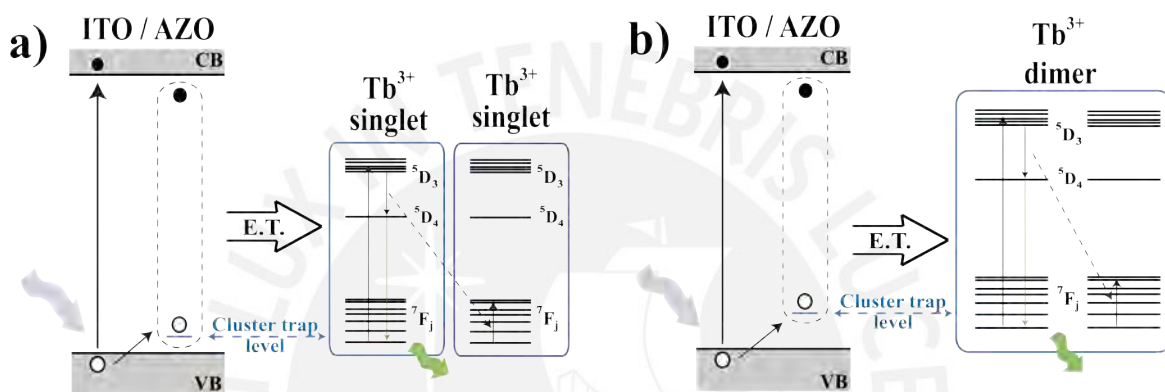


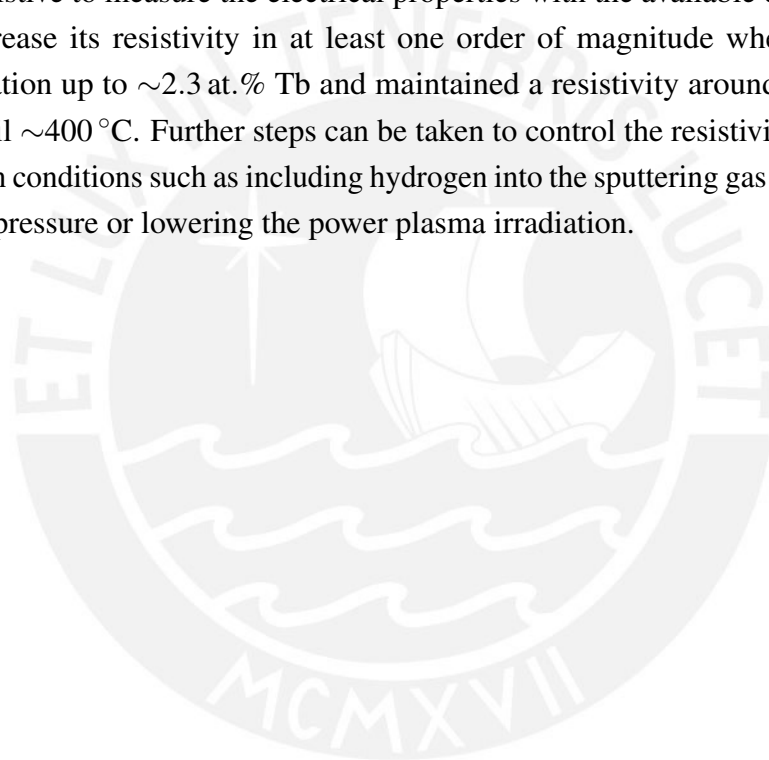
Fig. 6.1 Schematic of the proposed energy transfer mechanism between ITO or AZO and the  $Tb^{3+}$  ion cluster for a singlet ( $n=1$ ) in a) and a dimer ( $n=2$ ) in b). The absorbed photon generates an electron-hole pair and the generated hole is trapped by the cluster at the corresponding trap level. Subsequently, the hole attracts an electron from the conduction band to form a bound exciton. The exciton recombines and the recombination energy is transferred to the cluster. Additional relaxation mechanisms may take place to facilitate radiative transitions from  $Tb^{3+}$  ions. For instance, in a), two adjacent singlets can interact to enable radiative transitions from the  ${}^5D_4$  level. In b), the two ions within the dimer can interact to facilitate radiative transitions from  ${}^5D_4$ .

It is proposed that the excitation mechanism of the optically active  $Tb$  ions in both ITO and AZO is of excitonic nature. Based on the results from the temperature-dependent PL measurements, the estimated activation energies were associated to luminescence quenching processes that start to compete as the sample temperature increases. These energies were associated to binding energies of excitons that are bound to clusters of  $Tb^{3+}$  ions that act as isovalent traps in the case of ITO and to clusters of  $Tb^{3+}$  ions or  $Tb^{3+}$  complexes formed with host defects in the case of AZO. Figure 6.1 depicts the proposed energy transfer mechanism that might be occurring at the clusters with one and two ions. The cluster introduce an energy level that can trap a hole, which in turn can attract an electron to form a bound exciton. The recombination energy from the bound exciton would be transferred to the cluster and further

excitation of the  $Tb^{3+}$  ions entails, with a subsequent characteristic emission. The emission could involve relaxation processes that enable radiative transitions from the  $^5D_4$  level.

However, further studies should be carried out to assess the excitation processes in order to have a clearer idea as to which are the competing radiative and non-radiative processes that intervene in the Tb emission. In this way, an enhancement of the Tb-related light emission from these hosts could be achieved by favoring the radiative processes while inhibiting those non-radiative.

In both cases, the electrical resistivity was affected by the introduction of Tb. AZO was made too resistive to measure the electrical properties with the available equipment, whilst ITO did increase its resistivity in at least one order of magnitude when increasing the Tb concentration up to  $\sim 2.3$  at.% Tb and maintained a resistivity around  $0.2 \Omega \cdot \text{cm}$  when annealed until  $\sim 400^\circ\text{C}$ . Further steps can be taken to control the resistivity by considering the deposition conditions such as including hydrogen into the sputtering gas mixture, reducing the working pressure or lowering the power plasma irradiation.



## References

- [1] Gongxun Bai, Shuoguo Yuan, Yuda Zhao, Zhibin Yang, Sin Yuk Choi, Yang Chai, Siu Fung Yu, Shu Ping Lau, and Jianhua Hao. 2d layered materials of rare-earth Er-doped MoS<sub>2</sub> with NIR-to-NIR down- and up-conversion photoluminescence. *Adv. Mater.*, 28:7472–7477, 2016. doi: 10.1002/adma.201601833.
- [2] Nannan Yao, Jinzhao Huang, Ke Fu, Xiaolong Deng, Meng Ding, and Xijin Xu. Rare earth ion doped phosphors for dye-sensitized solar cells applications. *RSC Adv.*, 6: 17546–17559, 2016. doi: 10.1039/C5RA27033B.
- [3] P. Xing, G. F. R. Chen, X. Zhao, D. K. T. Ng, M. C. Tan, and D. T. H. Tan. Silicon rich nitride ring resonators for rare-earth doped telecommunications-band amplifiers pumped at the O-band. *Sci. Rep.*, 7:9101, 2017. doi: 10.1038/s41598-017-09732-x.
- [4] A Kenyon. Recent developments in rare-earth doped materials for optoelectronics. *Prog. Quantum Electron.*, 26:225–284, 2002. doi: 10.1016/S0079-6727(02)00014-9.
- [5] D. S. Lee and A. J. Steckl. Enhanced blue emission from Tm-doped Al<sub>x</sub>Ga<sub>1-x</sub>N electroluminescent thin films. *Appl. Phys. Lett.*, 83:2094–2096, 2003. doi: 10.1063/1.1611275.
- [6] Ling Li, Shenwei Wang, Guangyao Mu, Xue Yin, and Lixin Yi. Multicolor light-emitting devices with Tb<sub>2</sub>O<sub>3</sub> on silicon. *Sci. Rep.*, 7:42479, 2017. doi: 10.1038/srep42479.
- [7] Christian Kränkel, Daniel-Timo Marzahl, Francesca Moglia, Günter Huber, and Philip Werner Metz. Out of the blue: semiconductor laser pumped visible rare-earth doped lasers. *Laser Photon. Rev.*, 10:548–568, 2016. doi: 10.1002/lpor.201500290.
- [8] Galina Nemova and Raman Kashyap. Laser cooling in Yb<sup>3+</sup>:YAG. *J. Opt. Soc. Am. B*, 31:340, 2014. doi: 10.1364/JOSAB.31.000340.
- [9] D. Scoca, M. Morales, R. Merlo, F. Alvarez, and A. R. Zanatta. Photoluminescence and compositional-structural properties of ion-beam sputter deposited Er-doped TiO<sub>2-x</sub>N<sub>x</sub> films: Their potential as a temperature sensor. *J. Appl. Phys.*, 117:205304, 2015. doi: 10.1063/1.4921809.
- [10] A. R. Zanatta, D. Scoca, and F. Alvarez. A suitable (wide-range + linear) temperature sensor based on Tm<sup>3+</sup> ions. *Sci. Rep.*, 7:14113, 2017. doi: 10.1038/s41598-017-14535-1.

- [11] Michael N. Getz, Ola Nilsen, and Per-Anders Hansen. Sensors for optical thermometry based on luminescence from layered YVO<sub>4</sub>: Ln<sup>3+</sup> (Ln = Nd, Sm, Eu, Dy, Ho, Er, Tm, Yb) thin films made by atomic layer deposition. *Sci. Rep.*, 9:10247, 2019. doi: 10.1038/s41598-019-46694-8.
- [12] Dongling Geng, Elena Cabello-Olmo, Gabriel Lozano, and Hernán Míguez. Photonic structuring improves the colour purity of rare-earth nanophosphors. *Mater. Horizons*, 5:661–667, 2018. doi: 10.1039/C8MH00123E.
- [13] I. B. Gallo, A. Braud, and A. R. Zanatta. Efficient 1535 nm light emission from an all-Si-based optical micro-cavity containing Er<sup>3+</sup> and Yb<sup>3+</sup> ions. *Opt. Express*, 21:28394, 2013. doi: 10.1364/OE.21.028394.
- [14] Fan Zhang, Yonghui Deng, Yifeng Shi, Renyuan Zhang, and Dongyuan Zhao. Photoluminescence modification in upconversion rare-earth fluoride nanocrystal array constructed photonic crystals. *J. Mater. Chem.*, 20:3895, 2010. doi: 10.1039/c000379d.
- [15] Lucile Dumont, Julien Cardin, Christophe Labbé, Cédric Frilay, Pierre-Matthieu Anglade, Ing-Song Yu, Maxime Vallet, Patrick Benzo, Marzia Carrada, Didier Stiévenard, Hocine Merabet, and Fabrice Gourbilleau. First down converter multilayers integration in an industrial Si solar cell process. *Prog. Photovoltaics Res. Appl.*, 27:152–162, 2019. doi: 10.1002/pip.3071.
- [16] Wen-Jeng Ho, Jheng-Jie Liu, Zong-Xian Lin, and Hung-Pin Shiao. Enhancing Photovoltaic Performance of GaAs Single-Junction Solar Cells by Applying a Spectral Conversion Layer Containing Eu-Doped and Yb/Er-Doped Phosphors. *Nanomaterials*, 9:1518, 2019. doi: 10.3390/nano9111518.
- [17] L. Dumont, P. Benzo, J. Cardin, I.-S. Yu, C. Labbé, P. Marie, C. Dufour, G. Zatoryb, A. Podhorodecki, and F. Gourbilleau. Down-shifting Si-based layer for Si solar applications. *Sol. Energy Mater. Sol. Cells*, 169:132–144, 2017. doi: 10.1016/j.solmat.2017.05.011.
- [18] H. J. Lozykowski and W. M. Jadwisienczak. Thermal quenching of luminescence and isovalent trap model for rare-earth-ion-doped AlN. *physica status solidi (b)*, 244(6):2109–2126, jun 2007. doi: 10.1002/pssb.200642152.
- [19] R. Weingärtner, O. Erlenbach, A. Winnacker, A. Welte, I. Brauer, H. Mendel, H.P. Strunk, C.T.M. Ribeiro, and A.R. Zanatta. Thermal activation, cathodo- and photoluminescence measurements of rare earth doped (Tm,Tb,Dy,Eu,Sm,Yb) amorphous/nanocrystalline AlN thin films prepared by reactive rf-sputtering. *Opt. Mater. (Amst)*, 28:790–793, 2006. doi: 10.1016/j.optmat.2005.09.024.
- [20] A R Zanatta. Effect of thermal annealing treatments on the optical properties of rare-earth-doped AlN films. *J. Phys. D. Appl. Phys.*, 42:025109, 2009. doi: 10.1088/0022-3727/42/2/025109.
- [21] J A Guerra, F De Zela, K Tucto, L Montañez, J A Töfflinger, A Winnacker, and R Weingärtner. Effect of thermal annealing treatments on the optical activation of Tb<sup>3+</sup>-doped amorphous SiC:H thin films. *J. Phys. D. Appl. Phys.*, 49:375104, 2016. doi: 10.1088/0022-3727/49/37/375104.



- [22] J. Andres Guerra, Liz Montañez, Albrecht Winnacker, Francisco De Zela, and Roland Weingärtner. Thermal activation and temperature dependent PL and CL of Tb doped amorphous AlN and SiN thin films. *Phys. status solidi*, 12:1183–1186, 2015. doi: 10.1002/pssc.201400226.
- [23] A. R. Zanatta. Visible light emission and energy transfer processes in Sm-doped nitride films. *J. Appl. Phys.*, 111:123105, 2012. doi: 10.1063/1.4729911.
- [24] A. R. Zanatta. An alternative experimental approach to produce rare-earth-doped SiO<sub>x</sub> films. *J. Appl. Phys.*, 119:145302, 2016. doi: 10.1063/1.4945677.
- [25] J. Andres Guerra, Felix Benz, A. Ricardo Zanatta, Horst P. Strunk, Albrecht Winnacker, and Roland Weingärtner. Concentration quenching and thermal activation of the luminescence from terbium-doped a-SiC:H and c-AlN thin films. *Phys. status solidi*, 10:68–71, 2013. doi: 10.1002/pssc.201200394.
- [26] T. O. L. Sunde, M. Lindgren, T. O. Mason, M.-A. Einarsrud, and T. Grande. Solid solubility of rare earth elements (Nd, Eu, Tb) in In<sub>2-x</sub>Sn<sub>x</sub>O<sub>3</sub> – effect on electrical conductivity and optical properties. *Dalton Trans.*, 43(25):9620–9632, 2014. doi: 10.1039/C4DT00850B.
- [27] A. Janotta, M. Schmidt, R. Janssen, M. Stutzmann, and Ch. Buchal. Photoluminescence of Er<sup>3+</sup>-implanted amorphous hydrogenated silicon suboxides. *Physical Review B*, 68:165207, 2003. doi: 10.1103/PhysRevB.68.165207.
- [28] K. Y. Tucto, W. Aponte, J. A. Dulanto, J. A. Töfflinger, J. A. Guerra, and R. Grieseler. Combinatorial approach toward optimization of the light emission intensity of AlO<sub>x</sub>N<sub>y</sub>:Yb<sup>3+</sup> thin films. *Appl. Opt.*, 58:3097, 2019. doi: 10.1364/AO.58.003097.
- [29] Giacomo B.F. Bosco, Zahra Khatami, Jacek Wojcik, Peter Mascher, and Leandro R. Tessler. Excitation mechanism of Tb<sup>3+</sup> in a-Si<sub>3</sub>N<sub>4</sub>:H under sub-gap excitation. *J. Lumin.*, 202:327–331, 2018. doi: 10.1016/j.jlumin.2018.05.080.
- [30] Sandra Helen Skjærvø. *Terbium Doped ITO Thin Films Prepared by an Aqueous Sol-Gel Method*. Master thesis, Norwegian University of Science and Technology, 2013.
- [31] V. Anand, A. Sakthivelu, K. Deva Arun Kumar, S. Valanarasu, V. Ganesh, Mohd Shkir, A. Kathalingam, and S. AlFaify. Novel rare earth gd and al co-doped ZnO thin films prepared by nebulizer spray method for optoelectronic applications. *Superlattices and Microstructures*, 123:311–322, nov 2018. doi: 10.1016/j.spmi.2018.09.014.
- [32] V. Anand, A. Sakthivelu, K. Deva Arun Kumar, S. Valanarasu, V. Ganesh, Mohd Shkir, S. AlFaify, and H. Algarni. Rare earth Eu<sup>3+</sup> co-doped AZO thin films prepared by nebulizer spray pyrolysis technique for optoelectronics. *Journal of Sol-Gel Science and Technology*, 86(2):293–304, mar 2018. doi: 10.1007/s10971-018-4646-6.
- [33] V. Anand, A. Sakthivelu, K. Deva Arun Kumar, S. Valanarasu, A. Kathalingam, V. Ganesh, Mohd Shkir, S. AlFaify, and I.S. Yahia. Rare earth Sm<sup>3+</sup> co-doped AZO thin films for opto-electronic application prepared by spray pyrolysis. *Ceramics International*, 44(6):6730–6738, apr 2018. doi: 10.1016/j.ceramint.2018.01.088.

- [34] X. M. Teng, H. T. Fan, S. S. Pan, C. Ye, and G. H. Li. Influence of annealing on the structural and optical properties of ZnO:tb thin films. *Journal of Applied Physics*, 100(5):053507, sep 2006. doi: 10.1063/1.2227268.
- [35] S.M.C. Miranda, M. Peres, T. Monteiro, E. Alves, H.D. Sun, T. Geruschke, R. Vianden, and K. Lorenz. Rapid thermal annealing of rare earth implanted ZnO epitaxial layers. *Opt. Mater.*, 33:1139–1142, 2011. doi: 10.1016/j.optmat.2010.10.009.
- [36] A. Ziani, C. Davesne, C. Labbé, J. Cardin, P. Marie, C. Frilay, S. Boudin, and X. Portier. Annealing effects on the photoluminescence of terbium doped zinc oxide films. *Thin Solid Films*, 553:52–57, feb 2014. doi: 10.1016/j.tsf.2013.11.123.
- [37] Elias H. Penilla, Yasuhiro Kodera, and Javier E. Garay. Blue-green emission in terbium-doped alumina (Tb:Al<sub>2</sub>O<sub>3</sub>) transparent ceramics. *Adv. Funct. Mater.*, 23:6036–6043, 2013. doi: 10.1002/adfm.201300906.
- [38] Lung-Chien Chen, Ching-Ho Tien, and Wei-Chian Liao. A phosphor-free white light-emitting diode using In<sub>2</sub>O<sub>3</sub>:Tb transparent conductive light converter. *J. Phys. D. Appl. Phys.*, 44:165101, 2011. doi: 10.1088/0022-3727/44/16/165101.
- [39] Sirshendu Ghosh, Kajari Das, Godhuli Sinha, J. Lahtinen, and S. K. De. Bright white light emitting Eu and Tb co-doped monodisperse In<sub>2</sub>O<sub>3</sub> nanocrystals. *J. Mater. Chem. C*, 1:5557, 2013. doi: 10.1039/c3tc31087f.
- [40] Habib Elhouichet, Walid Ben Haj Othmen, and Sofiene Dabboussi. Effect of Sb, Tb<sup>3+</sup> doping on optical and electrical performances of SnO<sub>2</sub> and si based schottky diodes. *Silicon*, 12:715–722, 2020. doi: 10.1007/s12633-019-00164-y.
- [41] Laishram Priyobarta Singh, Ningthoujam Premananda Singh, and Sri Krishna Srivastava. Terbium doped SnO<sub>2</sub> nanoparticles as white emitters and SnO<sub>2</sub>:5Tb/Fe<sub>3</sub>O<sub>4</sub> magnetic luminescent nanohybrids for hyperthermia application and biocompatibility with hela cancer cells. *Dalt. Trans.*, 44:6457–6465, 2015. doi: 10.1039/C4DT03000A.
- [42] T. Neubert, F. Neumann, K. Schiffmann, P. Willich, and A. Hangleiter. Investigations on oxygen diffusion in annealing processes of non-stoichiometric amorphous indium tin oxide thin films. *Thin Solid Films*, 513:319–324, 2006. doi: 10.1016/j.tsf.2006.02.007.
- [43] G. E. Jellison and F. A. Modine. Parameterization of the optical functions of amorphous materials in the interband region. *Appl. Phys. Lett.*, 69:371–373, 1996. doi: 10.1063/1.118064.
- [44] Hiroyuki Fujiwara and Michio Kondo. Effects of carrier concentration on the dielectric function of ZnO:Ga and In<sub>2</sub>O<sub>3</sub>:Sn by spectroscopic ellipsometry: Analysis of free-carrier and band-edge absorption. *Physical Review B*, 71(7):075109, feb 2005. doi: 10.1103/physrevb.71.075109.
- [45] I. Volintiru, M. Creatore, and M. C. M. van de Sanden. In situ spectroscopic ellipsometry growth studies on the al-doped ZnO films deposited by remote plasma-enhanced metalorganic chemical vapor deposition. *Journal of Applied Physics*, 103(3):033704, feb 2008. doi: 10.1063/1.2837109.

- [46] C. Talagrand, X. Boddaert, D.G. Selmeczi, C. Defranoux, and P. Collot. Ellipsometry study of process deposition of amorphous indium gallium zinc oxide sputtered thin films. *Thin Solid Films*, 590:134–140, sep 2015. doi: 10.1016/j.tsf.2015.07.059.
- [47] Stephen K. O’Leary and P.K. Lim. On determining the optical gap associated with an amorphous semiconductor: A generalization of the tauc model. *Solid State Communications*, 104(1):17–21, oct 1997. doi: 10.1016/s0038-1098(97)00268-8.
- [48] J. Tauc. Optical properties and electronic structure of amorphous ge and si. *Materials Research Bulletin*, 3(1):37–46, jan 1968. doi: 10.1016/0025-5408(68)90023-8.
- [49] Frederick Wooten. *Optical properties of solids*. Academic Press, 1972. ISBN 0127634509.
- [50] J A Guerra, A Tejada, J A Töfflinger, R Grieseler, and L Korte. Band-fluctuations model for the fundamental absorption of crystalline and amorphous semiconductors: a dimensionless joint density of states analysis. *Journal of Physics D: Applied Physics*, 52(10):105303, jan 2019. doi: 10.1088/1361-6463/aaf963.
- [51] J A Guerra, J R Angulo, S Gomez, J Llamaza, L M Montañez, A Tejada, J A Töfflinger, A Winnacker, and R Weingärtner. The Urbach focus and optical properties of amorphous hydrogenated SiC thin films. *J. Phys. D. Appl. Phys.*, 49:195102, 2016. doi: 10.1088/0022-3727/49/19/195102.
- [52] J. A. Guerra, A. Tejada, L. Korte, L. Kegelman, J. A. Töfflinger, S. Albrecht, B. Rech, and R. Weingärtner. Determination of the complex refractive index and optical bandgap of  $\text{CH}_3\text{NH}_3\text{PbI}_3$  thin films. *J. Appl. Phys.*, 121:173104, 2017. doi: 10.1063/1.4982894.
- [53] A. Tejada, S. Braunger, L. Korte, S. Albrecht, B. Rech, and J. A. Guerra. Optical characterization and bandgap engineering of flat and wrinkle-textured  $\text{FA } 0.83 \text{ Cs } 0.17 \text{ Pb}(\text{I} 1- x \text{ Br } x ) 3$  perovskite thin films. *J. Appl. Phys.*, 123:175302, 2018. doi: 10.1063/1.5025728.
- [54] Peter Y. Yu and Manuel Cardona. *Fundamentals of Semiconductors*. Springer-Verlag Berlin Heidelberg, 2010. doi: 10.1007/978-3-642-00710-1.
- [55] A.B. Djurišić, Y. Chan, and E.H. Li. The optical dielectric function of ZnO. *Applied Physics A: Materials Science & Processing*, 76(1):37–43, jan 2003. doi: 10.1007/s003390201290.
- [56] Arman Mahboubi Soufiani, Fuzhi Huang, Peter Reece, Rui Sheng, Anita Ho-Baillie, and Martin A. Green. Polaronic exciton binding energy in iodide and bromide organic-inorganic lead halide perovskites. *Applied Physics Letters*, 107(23):231902, dec 2015. doi: 10.1063/1.4936418.
- [57] Kevin Lizárraga. PhD thesis, Pontificia Universidad Católica del Perú, 2023.
- [58] Hiroyuki Fujiwara. *Spectroscopic Ellipsometry*. Wiley, 2007. ISBN 9780470016084.
- [59] F. Baur, F. Glocker, and T. Jüstel. Photoluminescence and energy transfer rates and efficiencies in  $\text{Eu}^{3+}$  activated  $\text{Tb}_2\text{Mo}_3\text{O}_{12}$ . *Journal of Materials Chemistry C*, 3(9): 2054–2064, 2015. doi: 10.1039/c4tc02588a.

- [60] Ana de Bettencourt-Dias. *The Rare Earth Elements Fundamentals And Applications*, chapter The electronic Structure of the Lanthanides, pages 27–34. John Wiley & Sons, 2013. ISBN 978-1-119-95097-4.
- [61] Julien Andres and Anne-Sophie Chauvin. *The Rare Earth Elements Fundamentals And Applications*, chapter Luminescence, pages 27–34. John Wiley & Sons, 2013. ISBN 978-1-119-95097-4.
- [62] Jean-Claude G. Bünzli and Svetlana V. Eliseeva. Basics of lanthanide photophysics. In *Lanthanide Luminescence*, pages 1–45. Springer Berlin Heidelberg, 2010. doi: 10.1007/4243\_2010\_3.
- [63] D. L. Dexter. A theory of sensitized luminescence in solids. *The Journal of Chemical Physics*, 21(5):836–850, may 1953. doi: 10.1063/1.1699044.
- [64] Eiichiro Nakazawa. *Phosphor Handbook, Second Edition (Laser and Optical Science and Technology)*, chapter Fundamentals of luminescence, page 1080. CRC, 2006. ISBN 0-8493-3564-7.
- [65] Raúl A. Baragiola. Sputtering: survey of observations and derived principles. *Philosophical Transactions of the Royal Society of London. Series A: Mathematical, Physical and Engineering Sciences*, 362(1814):29–53, nov 2003. doi: 10.1098/rsta.2003.1301.
- [66] Gerhard Dehm, James M. Howe, and Josef Zweck. *In-Situ Electron Microscopy Applications in Physics, Chemistry and Materials Science*. Wiley-VCH Verlag GmbH, 2012. ISBN 9783527319732.
- [67] Joseph I. Goldstein, Dale E. Newbury, David C. Joy, Nicholas W. M. Ritchie, and John Henry J. Scott. *Scanning Electron Microscopy and X-Ray Microanalysis*. Springer, 2017. ISBN 9781493966745.
- [68] Pierre Hovington, Dominique Drouin, and Raynald Gauvin. CASINO: A new monte carlo code in c language for electron beam interaction -part i: Description of the program. *Scanning*, 19(1):1–14, dec 2006. doi: 10.1002/sca.4950190101.
- [69] Dominique Drouin, Pierre Hovington, and Raynald Gauvin. CASINO: A new monte carlo code in c language for electron beam interactions-part II: Tabulated values of the mott cross section. *Scanning*, 19(1):20–28, jan 1997. doi: 10.1002/sca.4950190103.
- [70] Pierre Hovington, Dominique Drouin, Raynald Gauvin, David C. Joy, and Neal Evans. CASINO: A new monte carlo code in c language for electron beam interactions-part III: Stopping power at low energies. *Scanning*, 19(1):29–35, jan 1997. doi: 10.1002/sca.4950190104.
- [71] Dominique Drouin, Alexandre Réal Couture, Dany Joly, Xavier Tastet, Vincent Aimez, and Raynald Gauvin. CASINO v2.42—a fast and easy-to-use modeling tool for scanning electron microscopy and microanalysis users. *Scanning*, 29(3):92–101, 2007. doi: 10.1002/sca.20000.
- [72] ASTM International. ASTM E1508-12a(2019) Standard Guide for Quantitative Analysis by Energy-Dispersive Spectroscopy. 2019. doi: 10.1520/E1508-12AR19.

- [73] Gregory S. Rohrer. *Structure and Bonding in Crystalline Materials*. Cambridge University Press, 2001. ISBN 0-521-66328-8.
- [74] Christopher Hammond. *Basics of Crystallography and Diffraction Fourth Edition*. Oxford University Press, 2015. ISBN 9780198738671.
- [75] J. I. Langford and A. J. C. Wilson. Scherrer after sixty years: A survey and some new results in the determination of crystallite size. *Journal of Applied Crystallography*, 11(2):102–113, apr 1978. doi: 10.1107/s0021889878012844.
- [76] Bruker AXS GmbH. *Topas 5 Technical Reference*, 2014.
- [77] Howard F. McMurdie, Marlene C. Morris, Eloise H. Evans, Boris Paretzkin, Winnie Wong-Ng, Lisa Ettliger, and Camden R. Hubbard. Standard x-ray diffraction powder patterns from the JCPDS research associateship. *Powder Diffraction*, 1(2):64–77, jun 1986. doi: <https://doi.org/10.1017/S0885715600011593>.
- [78] Joachim U. Brehm, Markus Winterer, and Horst Hahn. Synthesis and local structure of doped nanocrystalline zinc oxides. *Journal of Applied Physics*, 100(6):064311, sep 2006. doi: 10.1063/1.2349430.
- [79] J. Albertsson, S. C. Abrahams, and Å. Kvik. Atomic displacement, anharmonic thermal vibration, expansivity and pyroelectric coefficient thermal dependences in ZnO. *Acta Crystallographica Section B Structural Science*, 45(1):34–40, feb 1989. doi: 10.1107/S0108768188010109.
- [80] S. C. Abrahams and J. L. Bernstein. Remeasurement of the structure of hexagonal ZnO. *Acta Crystallographica Section B Structural Crystallography and Crystal Chemistry*, 25(7):1233–1236, jul 1969. doi: 10.1107/s0567740869003876.
- [81] Olaf Stenzel. *The Physics of Thin Film Optical Spectra*. Springer, 2005. ISBN 3-540-23147-1.
- [82] A. Tejada, L. Montañez, C. Torres, P. Llontop, L. Flores, F. De Zela, A. Winnacker, and J. A. Guerra. Determination of the fundamental absorption and optical bandgap of dielectric thin films from single optical transmittance measurements. *Appl. Opt.*, 58:9585, 2019. doi: 10.1364/AO.58.009585.
- [83] R.A Synowicki. Spectroscopic ellipsometry characterization of indium tin oxide film microstructure and optical constants. *Thin Solid Films*, 313-314:394–397, 1998. doi: 10.1016/S0040-6090(97)00853-5.
- [84] H. Kim, C. M. Gilmore, A. Piqué, J. S. Horwitz, H. Mattoussi, H. Murata, Z. H. Kafafi, and D. B. Chrisey. Electrical, optical, and structural properties of indium-tin-oxide thin films for organic light-emitting devices. *J. Appl. Phys.*, 86:6451–6461, 1999. doi: 10.1063/1.371708.
- [85] Yeon Sik Jung. Spectroscopic ellipsometry studies on the optical constants of indium tin oxide films deposited under various sputtering conditions. *Thin Solid Films*, 467: 36–42, 2004. doi: 10.1016/j.tsf.2004.02.047.

- [86] Ho-Chul Lee and O. Ok Park. The evolution of the structural, electrical and optical properties in indium-tin-oxide thin film on glass substrate by DC reactive magnetron sputtering. *Vacuum*, 80:880–887, 2006. doi: 10.1016/j.vacuum.2005.11.069.
- [87] Norbert Kaiser. Review of the fundamentals of thin-film growth. *Appl. Opt.*, 41:3053, 2002. doi: 10.1364/AO.41.003053.
- [88] Prakash Uprety, Maxwell M Junda, Hannah Salmon, and Nikolas J Podraza. Understanding near infrared absorption in tin doped indium oxide thin films. *J. Phys. D. Appl. Phys.*, 51:295302, 2018. doi: 10.1088/1361-6463/aac9e8.
- [89] Jose Solé, Luisa Bausa, and Daniel Jaque. *An Introduction to the Optical Spectroscopy of Inorganic Solids*. Wiley, 2005. ISBN 9780470868850.
- [90] L. J. van der Pauw. A method of measuring specific resistivity and hall effect of discs of arbitrary shape. *Philips Res. Rep.*, 13:1–9, 1958.
- [91] L. J. van der Pauw. A method of measuring the resistivity and hall coefficient on lamellae of arbitrary shape. *Philips Res. Rep.*, 20:220–224, 1958.
- [92] Klaus Ellmer. Hall effect and conductivity measurements in semiconductor crystals and thin films. In *Characterization of Materials*, pages 564–579. John Wiley & Sons, Inc., October 2012. doi: <https://doi.org/10.1002/0471266965.com035.pub2>.
- [93] Florian Werner. Hall measurements on low-mobility thin films. *Journal of Applied Physics*, 122(13):135306, oct 2017. doi: 10.1063/1.4990470.
- [94] Shinich Honda, Michio Watamori, and Kenjiro Oura. The effects of oxygen content on electrical and optical properties of indium tin oxide films fabricated by reactive sputtering. *Thin Solid Films*, 281-282:206–208, aug 1996. doi: 10.1016/0040-6090(96)08614-2.
- [95] Shinichi Honda, Akira Tsujimoto, Michio Watamori, and Kenjiro Oura. Oxygen content of indium tin oxide films fabricated by reactive sputtering. *Journal of Vacuum Science & Technology A: Vacuum, Surfaces and Films*, 13(3):1100–1103, may 1995. doi: 10.1116/1.579593.
- [96] John C. C. Fan and John B. Goodenough. X-ray photoemission spectroscopy studies of sn-doped indium-oxide films. *Journal of Applied Physics*, 48(8):3524–3531, aug 1977. doi: 10.1063/1.324149.
- [97] S. V. Belaya, V. V. Bakovets, A. I. Boronin, S. V. Koshcheev, M. N. Lobzareva, I. V. Korolkov, and P. A. Stabnikov. Terbium oxide films grown by chemical vapor deposition from terbium(III) dipivaloylmethanate. *Inorganic Materials*, 50(4):379–386, mar 2014. doi: 10.1134/s0020168514040037.
- [98] Tung-Ming Pan, Ji-Shing Jung, and Fa-Hsyang Chen. Metal-oxide-high-k-oxide-silicon memory structure incorporating a  $Tb_2O_3$  charge trapping layer. *Applied Physics Letters*, 97(1):012906, jul 2010. doi: 10.1063/1.3462321.

- [99] Tung-Ming Pan, Chih-Wei Wang, Yu-Shu Huang, Wen-Hui Weng, and See-Tong Pang. Effect of postdeposition annealing on the structural and sensing characteristics of  $\text{tb}_2\text{o}_3$  and  $\text{tb}_2\text{ti}_2\text{o}_7$  sensing films for electrolyte-insulator-semiconductor pH sensors. *Journal of The Electrochemical Society*, 162(4):B83–B88, 2015. doi: 10.1149/2.0641504jes.
- [100] I. Hamberg, C. G. Granqvist, K. F. Berggren, B. E. Sernelius, and L. Engström. Band-gap widening in heavily sn-doped  $\text{in}_2\text{o}_3$ . *Physical Review B*, 30(6):3240–3249, sep 1984. doi: 10.1103/physrevb.30.3240.
- [101] Chuen-Lin Tien, Hong-Yi Lin, Chih-Kai Chang, and Chien-Jen Tang. Effect of Oxygen Flow Rate on the Optical, Electrical, and Mechanical Properties of DC Sputtering ITO Thin Films. *Adv. Condens. Matter Phys.*, 2018:1–6, 2018. doi: 10.1155/2018/2647282.
- [102] J. Lægsgaard. Dissolution of rare-earth clusters in  $\text{si}_2\text{o}_2$  by al codoping: A microscopic model. *Physical Review B*, 65(17):174114, apr 2002. doi: 10.1103/physrevb.65.174114.
- [103] Vera Pukhkaya, Philippe Goldner, Alban Ferrier, and Nadège Ollier. Impact of rare earth element clusters on the excited state lifetime evolution under irradiation in oxide glasses. *Optics Express*, 23(3):3270, feb 2015. doi: 10.1364/oe.23.003270.
- [104] B Schaudel, P Goldner, M Prassas, and F Auzel. Cooperative luminescence as a probe of clustering in  $\text{Yb}^{3+}$  doped glasses. *Journal of Alloys and Compounds*, 300-301: 443–449, apr 2000. doi: 10.1016/s0925-8388(99)00760-4.
- [105] D. de Graaf, S.J. Stelwagen, H.T. Hintzen, and G. de With.  $\text{Tb}^{3+}$  luminescence as a tool to study clustering of lanthanide ions in oxynitride glasses. *Journal of Non-Crystalline Solids*, 325(1-3):29–33, sep 2003. doi: 10.1016/s0022-3093(03)00324-7.
- [106] A. N. Nazarov, S. I. Tiagulskiy, I. P. Tyagulskyy, V. S. Lysenko, L. Rebohle, J. Lehmann, S. Prucnal, M. Voelskow, and W. Skorupa. The effect of rare-earth clustering on charge trapping and electroluminescence in rare-earth implanted metal-oxide-semiconductor light-emitting devices. *J. Appl. Phys.*, 107:123112, 2010. doi: 10.1063/1.3436591.
- [107] Ningthoujam Surajkumar Singh, Shougaijam Dorendrajit Singh, and Sanoujam Dhiren Meetei. Structural and photoluminescence properties of terbium-doped zinc oxide nanoparticles. *Chin. Phys. B*, 23:058104, 2014. doi: 10.1088/1674-1056/23/5/058104.
- [108] Mohd. Shkir, Kamlesh V. Chandekar, Thamraa Alshahrani, Ashwani Kumar, and Salem AlFaify. A novel terbium doping effect on physical properties of lead sulfide nanostructures: A facile synthesis and characterization. *J Mater Res*, 35:2664–2675, 2020. doi: 10.1557/jmr.2020.216.
- [109] Pawan Chetri, Bhamyarswa Saikia, and Amarjyoti Choudhury. Structural and optical properties of Cu doped  $\text{SnO}_2$  nanoparticles: An experimental and density functional study. *J. Appl. Phys.*, 113:233514, 2013. doi: 10.1063/1.4811374.
- [110] David C. Paine, T. Whitson, D. Janiac, R. Beresford, Cleve Ow Yang, and Brian Lewis. A study of low temperature crystallization of amorphous thin film indium–tin–oxide. *J. Appl. Phys.*, 85:8445–8450, 1999. doi: 10.1063/1.370695.

- [111] Shinji Takayama, Toshifumi Sugawara, Akira Tanaka, and Tokuji Himuro. Indium tin oxide films with low resistivity and low internal stress. *J. Vac. Sci. Technol. A Vacuum, Surfaces, Film.*, 21:1351–1354, 2003. doi: 10.1116/1.1563623.
- [112] R.G. Dhere, T.A. Gessert, L.L. Schilling, A.J. Nelson, K.M. Jones, H. Aharoni, and T.J. Coutts. Electro-optical properties of thin indium tin oxide films: Limitations on performance. *Sol. Cells*, 21:281–290, 1987. doi: 10.1016/0379-6787(87)90127-X.
- [113] T. A. Gessert, D. L. Williamson, T. J. Coutts, A. J. Nelson, K. M. Jones, R. G. Dhere, H. Aharoni, and P. Zurcher. Summary Abstract: The dependence of the electrical properties of ion-beam sputtered indium tin oxide on its composition and structure. *J. Vac. Sci. Technol. A Vacuum, Surfaces, Film.*, 5:1314–1315, 1987. doi: 10.1116/1.574756.
- [114] Seon-Soon Kim, Se-Young Choi, Chan-Gyung Park, and Hyeon-Woo Jin. Transparent conductive ITO thin films through the sol-gel process using metal salts. *Thin Solid Films*, 347:155–160, 1999. doi: 10.1016/S0040-6090(98)01748-9.
- [115] Lata Gupta, Abhai Mansingh, and P.K. Srivastava. Band gap narrowing and the band structure of tin-doped indium oxide films. *Thin Solid Films*, 176:33–44, 1989. doi: 10.1016/0040-6090(89)90361-1.
- [116] Yutaka Furubayashi, Makoto Maehara, and Tetsuya Yamamoto. Tailoring of Point Defects in Polycrystalline Indium Tin Oxide Films with Postirradiation of Electronegative Oxygen Ions. *ACS Appl. Electron. Mater.*, 1:1545–1551, 2019. doi: 10.1021/acsaelm.9b00317.
- [117] H. Han, J. W. Mayer, and T. L. Alford. Effect of various annealing environments on electrical and optical properties of indium tin oxide on polyethylene naphthalate. *J. Appl. Phys.*, 99:123711, 2006. doi: 10.1063/1.2204815.
- [118] H. Han, J. W. Mayer, and T. L. Alford. Band gap shift in the indium-tin-oxide films on polyethylene naphthalate after thermal annealing in air. *J. Appl. Phys.*, 100:083715, 2006. doi: 10.1063/1.2357647.
- [119] Felix Benz, J. Andrés Guerra, Ye Weng, Roland Weingärtner, and Horst P. Strunk. How to describe concentration quenching in rare earth doped semiconductors. *Phys. status solidi*, 10:109–112, 2013. doi: 10.1002/pssc.201200357.
- [120] J. A. Guerra. *Optical characterization and thermal activation of Tb doped amorphous SiC, AlN and SiN thin films*. PhD thesis, Pontificia Universidad Católica del Perú / Friedrich-Alexander-Universität Erlangen-Nürnberg, 2017.
- [121] A. Layek, S. Banerjee, B. Manna, and A. Chowdhury. Synthesis of rare-earth doped ZnO nanorods and their defect–dopant correlated enhanced visible-orange luminescence. *RSC Adv.*, 6:35892–35900, 2016. doi: 10.1039/C6RA02278B.
- [122] I. A. Buyanova, M. Izadifard, W. M. Chen, A. Polimeni, M. Capizzi, H. P. Xin, and C. W. Tu. Hydrogen-induced improvements in optical quality of GaNAs alloys. *Appl. Phys. Lett.*, 82:3662–3664, 2003. doi: 10.1063/1.1578513.



- [123] J. D. Lambkin, L. Considine, S. Walsh, G. M. O'Connor, C. J. McDonagh, and T. J. Glynn. Temperature dependence of the photoluminescence intensity of ordered and disordered In 0.48 Ga 0.52 P. *Appl. Phys. Lett.*, 65:73–75, 1994. doi: 10.1063/1.113078.
- [124] P. Dorenbos and E. van der Kolk. Location of lanthanide impurity energy levels in the III-V semiconductor  $\text{Al}_x\text{Ga}_{1-x}\text{N}$  ( $0 \leq x \leq 1$ ). *Optical Materials*, 30:1052–1057, 2008. doi: 10.1016/j.optmat.2007.05.019.
- [125] Jonas J. Joos, David Van der Heggen, Lisa I. D. J. Martin, Lucia Amidani, Philippe F. Smet, Zoila Barandiarán, and Luis Seijo. Broadband infrared LEDs based on europium-to-terbium charge transfer luminescence. *Nat. Commun.*, 11:3647, 2020. doi: 10.1038/s41467-020-17469-x.
- [126] J. F. M. dos Santos, I. A. A. Terra, N. G. C. Astrath, F. B. Guimarães, M. L. Baesso, L. A. O. Nunes, and T. Catunda. Mechanisms of optical losses in the  $^5\text{D}_4$  and  $^5\text{D}_3$  levels in  $\text{Tb}^{3+}$  doped low silica calcium aluminosilicate glasses. *J. Appl. Phys.*, 117:053102, 2015. doi: 10.1063/1.4906781.
- [127] Brian G. Wybourne and William F. Meggers. Spectroscopic Properties of Rare Earths. *Phys. Today*, 18:70–72, 1965. doi: 10.1063/1.3047727.
- [128] A. Baldereschi. Theory of isoelectronic traps. *J. Lumin.*, 7:79–91, 1973. doi: 10.1016/0022-2313(73)90060-4.
- [129] O. Goede and D. Hennig. Isovalent-impurity clusters in koster-slater approximation. *Phys. status solidi*, 119:261–268, 1983. doi: 10.1002/pssb.2221190130.
- [130] H. J. Lozykowski. Kinetics of luminescence of isoelectronic rare-earth ions in III-V semiconductors. *Physical Review B*, 48(24):17758–17769, dec 1993. doi: 10.1103/physrevb.48.17758.
- [131] Jung H. Shin, G. N. van den Hoven, and A. Polman. Direct experimental evidence for trap-state mediated excitation of  $\text{Er}^{3+}$  in silicon. *Appl. Phys. Lett.*, 67:377–379, 1995. doi: 10.1063/1.114634.
- [132] N. Nepal, J. M. Zavada, D. S. Lee, A. J. Steckl, A. Sedhain, J. Y. Lin, and H. X. Jiang. Deep ultraviolet photoluminescence of Tm-doped AlGaIn alloys. *Appl. Phys. Lett.*, 94:111103, 2009. doi: 10.1063/1.3097808.
- [133] Jingzhou Wang, Atsushi Koizumi, Yasufumi Fujiwara, and Wojciech M. Jadwisnienczak. Optical and electrical study of defects in GaN in situ doped with  $\text{Eu}^{3+}$  ion grown by omvpe. *J. Electron. Mater.*, 45:6355–6362, 2016. doi: 10.1007/s11664-016-4983-6.
- [134] Gabriela B. González, Jerome B. Cohen, Jin-Ha Hwang, Thomas O. Mason, Jason P. Hodges, and James D. Jorgensen. Neutron diffraction study on the defect structure of indium-tin-oxide. *J. Appl. Phys.*, 89:2550–2555, 2001. doi: 10.1063/1.1341209.
- [135] C Gupta and N Krishnamurthy. *Extractive Metallurgy of Rare Earths*. CRC Press, Boca Raton, 2004. doi: 10.1201/9780203413029.

- [136] Jarosław Kaszewski, Bartłomiej S. Witkowski, Łukasz Wachnicki, Hanka Przybylińska, Bolesław Kozankiewicz, Ewa Mijowska, and Marek Godlewski. Reduction of Tb<sup>4+</sup> ions in luminescent Y<sub>2</sub>O<sub>3</sub>:Tb nanorods prepared by microwave hydrothermal method. *J. Rare Earths*, 34:774–781, 2016. doi: 10.1016/S1002-0721(16)60093-5.
- [137] O. Goede, W. Heimbrodt, and R. Müller. CdS<sub>1-x</sub>Te<sub>x</sub> as persistence-type semiconductor mixed crystals. *Phys. status solidi*, 105:543–550, 1981. doi: 10.1002/pssb.2221050213.
- [138] Madhvendra Nath Tripathi, Kazuhito Shida, Ryoji Sahara, Hiroshi Mizuseki, and Yoshiyuki Kawazoe. First-principles analysis of structural and opto-electronic properties of indium tin oxide. *J. Appl. Phys.*, 111:103110, 2012. doi: 10.1063/1.4719980.
- [139] Chainok Kittipong, Phailyn Khemthong, Filip Kielar, and Yan Zhou. Crystal structure of a mixed-ligand terbium(III) coordination polymer containing oxalate and formate ligands, having a three-dimensional fcu topology. *Acta Crystallogr. Sect. E Crystallogr. Commun.*, 72:87–91, 2016. doi: 10.1107/S205698901502397X.
- [140] Thaiane Gregório, Siddhartha O. K. Giese, Giovana G. Nunes, Jaísa F. Soares, and David L. Hughes. Crystal structures of two mononuclear complexes of terbium(III) nitrate with the tripodal alcohol 1,1,1-tris(hydroxymethyl)propane. *Acta Crystallogr. Sect. E Crystallogr. Commun.*, 73:278–285, 2017. doi: 10.1107/S2056989017001116.
- [141] Jun-Bo Lu, David C. Cantu, Manh-Thuong Nguyen, Jun Li, Vassiliki-Alexandra Glezakou, and Roger Rousseau. Norm-Conserving Pseudopotentials and Basis Sets To Explore Lanthanide Chemistry in Complex Environments. *J. Chem. Theory Comput.*, 15:5987–5997, 2019. doi: 10.1021/acs.jctc.9b00553.
- [142] D. Hennig, O. Goede, and W. Heimbrodt. Koster-Slater Model for Isolated and Paired Te Isoelectronic Impurities in II-VI Semiconductors. *Phys. status solidi*, 113:K163–K167, 1982. doi: 10.1002/pssb.2221130261.
- [143] Dongyun Wan, Ping Chen, Jun Liang, Shaotang Li, and Fuqiang Huang. (211)-orientation preference of transparent conducting In<sub>2</sub>O<sub>3</sub>:Sn films and its formation mechanism. *ACS Appl. Mater. Interfaces*, 3:4751–4755, 2011. doi: 10.1021/am2012432.
- [144] C. Körber, V. Krishnakumar, A. Klein, G. Panaccione, P. Torelli, A. Walsh, J. L. F. Da Silva, S.-H. Wei, R. G. Egdell, and D. J. Payne. Electronic structure of In<sub>2</sub>O<sub>3</sub> and Sn-doped In<sub>2</sub>O<sub>3</sub> by hard x-ray photoemission spectroscopy. *Physical Review B*, 81:165207, 2010. doi: 10.1103/PhysRevB.81.165207.
- [145] Yinzhi Chen, Hongchuan Jiang, Shuwen Jiang, Xingzhao Liu, Wanli Zhang, and Qinyong Zhang. Influence of Annealing Temperature on the Microstructure and Electrical Properties of Indium Tin Oxide Thin Films. *Acta Metall. Sin. (English Lett.)*, 27:368–372, 2014. doi: 10.1007/s40195-014-0059-x.
- [146] Masatoshi Higuchi, Shinichiro Uekusa, Ryotaro Nakano, and Kazuhiko Yokogawa. Postdeposition Annealing Influence on Sputtered Indium Tin Oxide Film Characteristics. *Jpn. J. Appl. Phys.*, 33:302–306, 1994. doi: 10.1143/JJAP.33.302.

- [147] Jinyuan Zhou, Dengfei Song, Hao Zhao, Xiaojun Pan, Zhenxing Zhang, Yanzhe Mao, Yujun Fu, Tao Wang, and Erqing Xie. Microstructural and photoluminescent properties of terbium-doped SiC nanotubes prepared by sputtering using electrospun polymer templates. *J. Lumin.*, 157:119–125, 2015. doi: 10.1016/j.jlumin.2014.08.046.
- [148] U Wahl, E Alves, K Lorenz, J.G Correia, T Monteiro, B De Vries, A Vantomme, and R Vianden. Lattice location and optical activation of rare earth implanted GaN. *Mater. Sci. Eng. B*, 105:132–140, 2003. doi: 10.1016/j.mseb.2003.08.031.
- [149] Saad Rahmane, Mohamed Abdou Djouadi, Mohamed Salah Aida, and Nicolas Barreau. Oxygen effect in radio frequency magnetron sputtered aluminium doped zinc oxide films. *Thin Solid Films*, 562:70–74, jul 2014. doi: 10.1016/j.tsf.2014.03.073.
- [150] T.H. Okabe, K. Hirota, E. Kasai, F. Saito, Y. Waseda, and K.T. Jacob. Thermodynamic properties of oxygen in RE–O (RE=gd, tb, dy, er) solid solutions. *Journal of Alloys and Compounds*, 279(2):184–191, oct 1998. doi: 10.1016/s0925-8388(98)00690-2.
- [151] Norifumi Fujimura, Tokihiro Nishihara, Seiki Goto, Jifang Xu, and Taichiro Ito. Control of preferred orientation for ZnO films: control of self-texture. *Journal of Crystal Growth*, 130(1-2):269–279, may 1993. doi: 10.1016/0022-0248(93)90861-p.
- [152] Nalin Prashant Poddar and S. K. Mukherjee. Investigations on preferentially oriented al-doped ZnO films developed using rf magnetron sputtering. *Journal of Materials Science: Materials in Electronics*, 30(1):537–548, nov 2018. doi: 10.1007/s10854-018-0320-6.
- [153] A Van der Drift. Evolutionary selection, a principle governing growth orientation in vapour-deposited layers. *Philips Res. Rep*, 22(3):267, 1967.
- [154] Swee-Yong Pung, Kwang-Leong Choy, Xianghui Hou, and Chongxin Shan. Preferential growth of ZnO thin films by the atomic layer deposition technique. *Nanotechnology*, 19(43):435609, sep 2008. doi: 10.1088/0957-4484/19/43/435609.
- [155] R. Boyn. 4f–4f luminescence of rare-earth centers in II–VI compounds. *physica status solidi (b)*, 148(1):11–47, jul 1988. doi: 10.1002/pssb.2221480102.
- [156] Z.B. Fang, Y.S. Tan, H.X. Gong, C.M. Zhen, Z.W. He, and Y.Y. Wang. Transparent conductive tb-doped ZnO films prepared by rf reactive magnetron sputtering. *Materials Letters*, 59(21):2611–2614, sep 2005. doi: 10.1016/j.matlet.2005.02.062.
- [157] Guy L. Kabongo, Gugu H. Mhlongo, Thomas Malwela, Bakang M. Mothudi, Kenneth T. Hillie, and Mokhotjwa S. Dhlamini. Microstructural and photoluminescence properties of sol-gel derived Tb<sup>3+</sup> doped ZnO nanocrystals. *Journal of Alloys and Compounds*, 591:156–163, apr 2014. doi: 10.1016/j.jallcom.2013.12.075.
- [158] Wenbing Hu and Rebecca L. Peterson. The roles of rare-earth dopants in solution-processed ZnO-based transparent conductive oxides. *Journal of Applied Physics*, 122(10):105301, sep 2017. doi: 10.1063/1.4991943.
- [159] Ü. Özgür, Ya. I. Alivov, C. Liu, A. Teke, M. A. Reshchikov, S. Doğan, V. Avrutin, S.-J. Cho, and H. Morkoç. A comprehensive review of ZnO materials and devices. *Journal of Applied Physics*, 98(4):041301, aug 2005. doi: 10.1063/1.1992666.

- [160] Anderson Janotti and Chris G. van de Walle. Native point defects in ZnO. *Physical Review B*, 76(16):165202, oct 2007. doi: 10.1103/physrevb.76.165202.
- [161] Vani Pawar, Pardeep K. Jha, S. K. Panda, Priyanka A. Jha, and Prabhakar Singh. Band-gap engineering in ZnO thin films: A combined experimental and theoretical study. *Physical Review Applied*, 9(5):054001, may 2018. doi: 10.1103/physrevapplied.9.054001.
- [162] Yashika Gupta, P. Arun, A.A. Naudi, M.V. Walz, and E.A. Albanesi. Grain size and lattice parameter's influence on band gap of SnS thin nano-crystalline films. *Thin Solid Films*, 612:310–316, aug 2016. doi: 10.1016/j.tsf.2016.05.056.
- [163] Sahitya V. Vegesna, Vinayak J. Bhat, Danilo Bürger, Jan Dellith, Ilona Skorupa, Oliver G. Schmidt, and Heidemarie Schmidt. Increased static dielectric constant in ZnMnO and ZnCoO thin films with bound magnetic polarons. *Scientific Reports*, 10(1), apr 2020. doi: 10.1038/s41598-020-63195-1.
- [164] F. Vratny. Reflectance spectra of terbium oxides in the range Tb<sub>2</sub>O<sub>3</sub> to Tb<sub>4</sub>O<sub>7</sub>. *The Journal of Chemical Physics*, 34(4):1377–1379, apr 1961. doi: 10.1063/1.1731747.
- [165] Tong-Ye Li, Hong-Wang Zhao, Liang Dong, Na Guo, and Yu Wang. Novel varistor material based on terbium oxide. *Journal of Physics D: Applied Physics*, 42(3):035401, dec 2008. doi: 10.1088/0022-3727/42/3/035401.
- [166] I. Chambouleyron, F. Fajardo, and A. R. Zanatta. Aluminum-induced crystallization of hydrogenated amorphous germanium thin films. *Applied Physics Letters*, 79(20):3233–3235, nov 2001. doi: 10.1063/1.1415772.
- [167] A. R. Zanatta and I. Chambouleyron. Low-temperature al-induced crystallization of amorphous ge. *Journal of Applied Physics*, 97(9):094914, may 2005. doi: 10.1063/1.1889227.
- [168] Zhuo Yang, Alessandro Surrente, Krzysztof Galkowski, Nicolas Bruyant, Duncan K. Maude, Amir Abbas Haghighirad, Henry J. Snaith, Paulina Plochocka, and Robin J. Nicholas. Unraveling the exciton binding energy and the dielectric constant in single-crystal methylammonium lead triiodide perovskite. *The Journal of Physical Chemistry Letters*, 8(8):1851–1855, apr 2017. doi: 10.1021/acs.jpcllett.7b00524.
- [169] Valerio D’Innocenzo, Giulia Grancini, Marcelo J. P. Alcocer, Ajay Ram Srimath Kandada, Samuel D. Stranks, Michael M. Lee, Guglielmo Lanzani, Henry J. Snaith, and Annamaria Petrozza. Excitons versus free charges in organo-lead tri-halide perovskites. *Nature Communications*, 5(1), apr 2014. doi: 10.1038/ncomms4586.
- [170] Ying Wang, Andris Suna, John McHugh, Edwin F. Hilinski, Patricia A. Lucas, and Robert D. Johnson. Optical transient bleaching of quantum-confined CdS clusters: The effects of surface-trapped electron–hole pairs. *The Journal of Chemical Physics*, 92(11):6927–6939, jun 1990. doi: 10.1063/1.458280.
- [171] Cheol Hyoun Ahn, Young Yi Kim, Dong Chan Kim, Sanjay Kumar Mohanta, and Hyung Koun Cho. A comparative analysis of deep level emission in ZnO layers deposited by various methods. *Journal of Applied Physics*, 105(1):013502, jan 2009. doi: 10.1063/1.3054175.

- [172] Haibo Zeng, Zhigang Li, Weiping Cai, and Peisheng Liu. Strong localization effect in temperature dependence of violet-blue emission from ZnO nanoshells. *Journal of Applied Physics*, 102(10):104307, nov 2007. doi: 10.1063/1.2803712.
- [173] Mingsong Wang, Yajun Zhou, Yiping Zhang, Eui Jung Kim, Sung Hong Hahn, and Seung Gie Seong. Near-infrared photoluminescence from ZnO. *Applied Physics Letters*, 100(10):101906, mar 2012. doi: 10.1063/1.3692584.
- [174] Renata Ratajczak, Elzbieta Guziewicz, Slawomir Prucnal, Grzegorz Łuka, Roman Böttger, Rene Heller, Cyprian Mieszczynski, Wojciech Wozniak, and Andrzej Turos. Luminescence in the visible region from annealed thin ALD-ZnO films implanted with different rare earth ions. *physica status solidi (a)*, 215(16):1700889, jan 2018. doi: 10.1002/pssa.201700889.
- [175] Claire Tonon, Carole Duvignacq, Gilbert Teysse, and Magdeleine Dinguirard. Degradation of the optical properties of ZnO-based thermal control coatings in simulated space environment. *Journal of Physics D: Applied Physics*, 34(1):124–130, dec 2000. doi: 10.1088/0022-3727/34/1/319.
- [176] Frank Güell and Paulina R. Martínez-Alanis. Tailoring the green, yellow and red defect emission bands in ZnO nanowires via the growth parameters. *Journal of Luminescence*, 210:128–134, jun 2019. doi: 10.1016/j.jlumin.2019.02.017.
- [177] Wasanthamala Badalawa, Hiroaki Matsui, Takamasa Osone, Noriyuki Hasuike, Hiroshi Harima, and Hitoshi Tabata. Correlation between structural and luminescent properties of  $\text{Eu}^{3+}$ -doped ZnO epitaxial layers. *Journal of Applied Physics*, 109(5):053502, mar 2011. doi: 10.1063/1.3549633.
- [178] A. El Manouni, F.J. Manjón, M. Perales, M. Mollar, B. Marí, M.C. Lopez, and J.R. Ramos Barrado. Effect of thermal annealing on ZnO:al thin films grown by spray pyrolysis. *Superlattices and Microstructures*, 42(1-6):134–139, jul 2007. doi: 10.1016/j.spmi.2007.04.005.
- [179] Jun Hong Noh, Hyun Suk Jung, Jung-Kun Lee, Jin Young Kim, Chin Moo Cho, Jae sul An, and Kug Sun Hong. Reversible change in electrical and optical properties in epitaxially grown al-doped ZnO thin films. *Journal of Applied Physics*, 104(7):073706, 2008. doi: 10.1063/1.2987472.
- [180] C. Guillén and J. Herrero. Optical, electrical and structural characteristics of al:ZnO thin films with various thicknesses deposited by DC sputtering at room temperature and annealed in air or vacuum. *Vacuum*, 84(7):924–929, mar 2010. doi: 10.1016/j.vacuum.2009.12.015.
- [181] F. Ruske, M. Roczen, K. Lee, M. Wimmer, S. Gall, J. Hüpkens, D. Hrunski, and B. Rech. Improved electrical transport in al-doped zinc oxide by thermal treatment. *Journal of Applied Physics*, 107(1):013708, jan 2010. doi: 10.1063/1.3269721.
- [182] T.P. McLean and E.G.S. Paige. A theory of the effects of carrier-carrier scattering on mobility in semiconductors. *Journal of Physics and Chemistry of Solids*, 16(3-4):220–236, nov 1960. doi: 10.1016/0022-3697(60)90152-9.

- [183] André Bikowski and Klaus Ellmer. Analytical model of electron transport in polycrystalline, degenerately doped ZnO films. *Journal of Applied Physics*, 116(14):143704, oct 2014. doi: 10.1063/1.4896839.
- [184] Elias Burstein. Anomalous optical absorption limit in InSb. *Physical Review*, 93(3): 632–633, feb 1954. doi: 10.1103/physrev.93.632.
- [185] T S Moss. The interpretation of the properties of indium antimonide. *Proceedings of the Physical Society. Section B*, 67(10):775–782, oct 1954. doi: 10.1088/0370-1301/67/10/306.
- [186] J. G. Lu, S. Fujita, T. Kawaharamura, H. Nishinaka, Y. Kamada, T. Ohshima, Z. Z. Ye, Y. J. Zeng, Y. Z. Zhang, L. P. Zhu, H. P. He, and B. H. Zhao. Carrier concentration dependence of band gap shift in n-type ZnO:al films. *Journal of Applied Physics*, 101(8):083705, apr 2007. doi: 10.1063/1.2721374.

